Western University
Scholarship@Western

Digitized Theses | Digitized Special Collections

2010

# EXPERIMENTAL AND NUMERICAL MODELING OF WIND FLOW OVER COMPLEX TOPOGRAPHY

Ashkan Rasouli

Follow this and additional works at: https://ir.lib.uwo.ca/digitizedtheses

Recommended Citation
Rasouli, Ashkan, "EXPERIMENTAL AND NUMERICAL MODELING OF WIND FLOW OVER COMPLEX TOPOGRAPHY" (2010). *Digitized Theses*. 3903.
https://ir.lib.uwo.ca/digitizedtheses/3903

This Thesis is brought to you for free and open access by the Digitized Special Collections at Scholarship@Western. It has been accepted for inclusion in Digitized Theses by an authorized administrator of Scholarship@Western. For more information, please contact wlswadmin@uwo.ca.

# EXPERIMENTAL AND NUMERICAL MODELING OF WIND FLOW OVER COMPLEX TOPOGRAPHY

(Spine Title: EXP. AND NUM. MODELING OF WIND FLOW OVER COMPLEX TOPOGRAPHY
(Thesis Format: Monograph)

by

Ashkan Rasouli

Department of Civil and Environmental Engineering
Faculty of Engineering Science

A thesis submitted in partial fulfillment
of the requirements for the degree of
Doctor of Philosophy

The School of Graduate and Postdoctoral Studies
The University of Western Ontario
London, Ontario, Canada

© Ashkan Rasouli 2010

**THE UNIVERSITY OF WESTERN ONTARIO**
**THE SCHOOL OF GRADUATE AND POSTDOCTORAL STUDIES**

**CERTIFICATE OF EXAMINATION**

Supervisor

Dr. Horia Hangan

Examiners

Dr. Rupp Carriveau

Dr. T.C.Eric Ho

Dr. Craig Miller

Dr. Chao Zhang

The thesis by

**Ashkan Rasouli**

entitled

**Experimental and Numerical Modeling of**

**Wind Flow over Complex Topography**

is accepted in partial fulfillment of the
requirements for the degree of
Doctor of Philosophy

Date_____

Chair of the Thesis Examination Board

**ABSTRACT**

Wind mapping is of utmost importance in various wind engineering, wind environment, and wind energy applications. The available wind atlases usually provide wind data with low resolutions relative to the wind turbine height and size and usually neglect the effect of topographic features with relatively large or sudden changes in elevation.

Developing a cost effective methodology to predict the wind patterns and to obtain wind maps over any topographic terrain is absolutely needed for wind turbine/farm siting. As the previous analytic and empirical attempts to resolve the flow over topographic features were limited to basic geometries that hardly exist in nature, applying Particle Image Velocimetry (PIV) measurement techniques in wind tunnel and Computational Fluid Dynamics (CFD) techniques in numerical simulation of the flow over topography seems to be the best alternative solution to the problem. PIV measurements and CFD simulations are carried out on a 1:3000 scale model of complex topographic area. Three distinct topographic features are investigated: a valley, a ridge and a hill.

The PIV measurements compare well with hot-wire based mean velocity profiles for the three cases. Moreover, the turbulence intensity profiles match well for flow regions without recirculation. The ridge wake region shows discrepancies between the two techniques which are attributed to the complexity of the flow in this region and limitations of both techniques.

A procedure incorporating Geographic Information System (GIS) and surface modeling techniques is introduced to build the CFD model of a complex terrain starting from the existing topography maps with desired resolutions. Moreover, a new approach is made to simulate the terrain roughness up to ultimate roughness heights, by implementing arrays

of bell-shaped roughness elements in the CFD model. The velocity profiles and velocity vectors were compared with the PIV measurements and were found to be in good agreement near the ground and up to the full scale height of 300m.

The study shows that PIV measurements and CFD simulations can be successfully used in qualifying and quantifying the flow over complex topography consisting of a wide range of roughness heights, enabling to map the flow structure with very high spatial resolution.

**KEYWORDS:** Wind mapping, Complex topography, Computational fluid dynamics (CFD), Particle image velocimetry (PIV)

## CO-AUTHORSHIP

All the work presented in this thesis was performed by Ashkan Rasouli. Chapter 2 of the thesis is published as two manuscripts in different scholarly journals co-authored by Ashkan Rasouli, Horia Hangan and Kamran Siddiqui.

**DEDICATION**

*To Sepideh*

## ACKNOWLEDGEMENTS

I am grateful to Professor Horia Hangan for the opportunity to work in such a great research environment, the supervision to guide me throughout the research process, the expertise to improve my work, and for his continuous support and patience.

The contribution of Professor Kamran Siddiqui in this work was necessary for the completion of my research. I am grateful to him for his excellent knowledge and expertise in PIV measurement technique.

I would like to thank my friends Arash, Pooyan and Taravat for their useful comments and great support during my study period and their invaluable help in completing my thesis. Also, I would like to thank Dr. Jongdae Kim and Mr. Ziad Boutanios, for their useful comments and helpful discussions.

I would like to express my deep gratitude to my wife, Sepideh, for her unlimited support, patience and love. I am grateful to her for her invaluable assistance during the past few months in formatting this thesis and its graphs.

And last but not least, I would like to express my affectionate appreciation to my brothers, Ali and Erfan, my father and mother in Iran, for their encouragement, patience and endless support.

**TABLE OF CONTENTS**

CERTIFICATE OF EXAMINATION ..... ii

ABSTRACT ..... iii

CO-AUTHORSHIP ..... v

DEDICATION ..... vi

ACKNOWLEDGEMENTS ..... vii

LIST OF TABLES ..... x

LIST OF FIGURES ..... xi

NUMENCLATURE ..... xvii

1 Introduction ..... 1
1.1 Background ..... 1
1.2 Experimental Approach ..... 2
1.2.1 Full Scale Measurements ..... 2
1.2.2 Wind Tunnel Testing ..... 4
1.3 Numerical Approach ..... 9
1.3.1 Meso-scale Numerical Simulations ..... 9
1.3.2 Micro-scale Numerical Simulations ..... 12
1.3.2.1 Generic Topographic Features ..... 13
1.3.2.2 Simple Topography ..... 15
1.3.2.3 Complex Topography ..... 17
1.4 Scope ..... 19

2 Experiments ..... 22
2.1 Introduction ..... 22
2.2 Experimental Setup ..... 23
2.2.1 Wind Tunnel ..... 23
2.2.2 Topographic Model ..... 24
2.2.2.1 Valley Configuration ..... 25
2.2.2.2 Hill Configuration ..... 26
2.2.2.3 Ridge Configuration ..... 28
2.2.3 PIV System ..... 28
2.2.3.1 Laser ..... 28
2.2.3.2 Optics ..... 28
2.2.3.3 Seeding System ..... 29
2.2.3.4 Image Acquisition System ..... 30
2.2.4 Set-up ..... 30
2.2.4.1 Vertical Plane Measurements ..... 35
2.2.4.2 Horizontal Plane Measurements ..... 42
2.3 Results and Discussion ..... 44
2.3.1 Valley Flow ..... 44
2.3.2 Hill Flow ..... 51

2.3.3 Ridge Flow ..... 56
2.4 Conclusions ..... 64

3 Simulations ..... 66
3.1 Introduction ..... 66
3.2 Two-Dimensional Simulation – NASA Hump ..... 67
3.2.1 Numerical Setup ..... 67
3.2.1.1 Solution Domain ..... 68
3.2.1.2 Boundary Conditions ..... 69
3.2.1.3 Grid ..... 69
3.2.1.4 Numerical Solution Method ..... 70
3.2.2 Results and Discussion ..... 74
3.2.3 Conclusions ..... 79
3.3 Three-Dimensional Simulation – Generic Hill ..... 80
3.3.1 Numerical Setup ..... 81
3.3.1.1 Solution Domain ..... 81
3.3.1.2 Boundary Conditions ..... 82
3.3.1.3 Grid ..... 83
3.3.1.4 Numerical Solution Method ..... 84
3.3.2 Results and Discussion ..... 84
3.3.3 Conclusions ..... 87
3.4 Complex Topography Simulation – Hong-Kong Model ..... 89
3.4.1 Numerical Setup ..... 89
3.4.1.1 Solution Domain ..... 91
3.4.1.2 Boundary Conditions ..... 91
3.4.1.3 Grid ..... 92
3.4.1.4 Numerical Solution Method ..... 96
3.4.2 Results and Discussion ..... 96
3.4.3 Valley Flow ..... 98
3.4.4 Hill Flow ..... 101
3.4.5 Ridge Flow ..... 103
3.4.6 Conclusions ..... 105

4 Conclusions ..... 106
4.1 Experiments ..... 107
4.2 Simulations ..... 108
4.3 Future work ..... 111

REFERENCES ..... 113

Appendix I: Error Estimate for PIV Measurements ..... 119

Appendix II: Turbulence Models used in CFD Simulations ..... 122

CURRICULUM VITAE ..... 126

## LIST OF TABLES

Table 2.1: Sensitivity analysis of the mean velocities relative to the size of the averaging area for the PIV velocity vectors. The percentage difference is calculated with respect to values measured with the hot-wire. ..... 49

Table 3.1: Flow conditions in NASA hump experiment ..... 68

Table 3.2: Grid independence study for the NASA hump. ..... 75

Table 3.3: Flow conditions for generic hill model. ..... 81

Table 3.4: The different domain dimensions used in the generic hill study. ..... 82

Table 3.5: Grid independence study for the generic hill. ..... 86

Table 3.6: Flow conditions for topography model: hill, valley and ridge cases ..... 92

## LIST OF FIGURES

Figure 2.1: BLWTL II, Boundary Layer Wind Tunnel Laboratory, University of Western Ontario.....23

Figure 2.2: Google Earth satellite images of Hong Kong: (a) Extent of the topographic model, (b) Southeast Hong Kong.....24

Figure 2.3: (a) Model surface. (b) Foam blocks representing the built-up areas.....26

Figure 2.4: Selected topographic features and wind tunnel configurations corresponding to them. (a) Valley and ridge configurations, (b) hill configuration.....27

Figure 2.5: Seed distributor.....29

Figure 2.6: Seed distributor location for (a) ridge configuration and (b) hill configuration....31

Figure 2.7: PIV system setup for (a) vertical plane measurements, (b) horizontal plane measurements. The images belong to valley configuration.....34

Figure 2.8: (a) A PIV image in the vertical plane. The dark regions in the image correspond to the areas where the seed density is very low. Some buildings (foam blocks) are also visible at the bottom of the image, obstructing the view of laser light sheet. (b) The segmented image obtained after applying the detection scheme to the presented PIV image. The black regions correspond to the areas with insufficient seed density. The buildings located at the bottom of the image are also marked and excluded. (c) The corrected instantaneous velocity field (d) The corresponding turbulent velocity field. The free-stream flow is from right to left.....37

Figure 2.9: (a) Instantaneous and (b) turbulent velocity fields from a PIV image pair that has sufficient seed density in the entire image pair. The free-stream flow is from right to left.....41

Figure 2.10: The region of interest in the horizontal plane measurements for the valley. The dimensions of the region of interest are 15cm×11.3cm. The length scale is also provided for

the model scale and full-scale (in parenthesis). The free-stream flow is from top to bottom of the image. ..... 41

Figure 2.11: (a) An instantaneous velocity field and (b) corresponding turbulent velocity field in a horizontal plane at a height of 8.4cm for the valley. The free-stream flow is from top to bottom. ..... 43

Figure 2.12: Wind direction for valley configuration. The cross marks the approximate location of the region of interest (Satellite image is from Google Earth) ..... 45

Figure 2.13: Topographic contours and side view of the valley configuration with horizontal and vertical measurement area locations, size and reference coordinates. The rectangles show the extent of the PIV measurements in horizontal and vertical planes. The thick solid lines in side view correspond to the horizontal measurement planes demonstrated as a rectangle in top view. ..... 45

Figure 2.14: Mean velocity field in the horizontal plane for the valley flow. (a) $z = 195\text{m}$, (b) $z = 312\text{m}$ ..... 46

Figure 2.15: Crosswind mean velocity magnitude ratios for the valley flow at three heights and two downstream locations. (a) $z = 195\text{m}$, $x = -44\text{m}$, (b) $z = 195\text{m}$, $x = 105\text{m}$, ..... 47

Figure 2.16: Contour plots for the valley flow in a vertical plane at $y = 0$. (a) Mean vorticity contours [1/sec], (b) t.k.e. contours [$\text{m}^2/\text{sec}^2$]. Flow direction is from right to left. ..... 48

Figure 2.17: Comparison of profiles measured by PIV and hot-wires for the valley flow. (a) Mean velocity, (b) Turbulence intensity. ..... 50

Figure 2.18: Wind direction for hill configuration. The cross marks the approximate location of the region of interest (Satellite image is from Google Earth). ..... 51

Figure 2.19: Topographic contours and side view of the hill configuration with horizontal and vertical measurement area locations, size and reference coordinates. The rectangles show the extent of the PIV measurements in horizontal and vertical planes. The thick solid lines in side view correspond to the horizontal measurement planes demonstrated as a rectangle in top view. ..... 52

Figure 2.20: Mean velocity vectors in the horizontal plane for the hill flow. (a) $z = 249\text{m}$, (b) $z = 360\text{m}$. ..... 53

Figure 2.21: Crosswind mean velocity magnitude ratios for the hill flow at two heights and two downstream locations. (a) $z = 249\text{m},\ x = 68\text{m}$, (b) $z = 249\text{m},\ x = 139\text{m}$, (c) $z = 360\text{m},\ x = 68\text{m}$, (d) $z = 360\text{m},\ x = 139\text{m}$. ..... 54

Figure 2.22: Contour plots for the hill flow in a vertical plane at $y = 0$. (a) Mean vorticity contours [1/sec], (b) t.k.e. contours [$\text{m}^2/\text{sec}^2$]. Flow direction is from right to left. ..... 55

Figure 2.23: Comparison of profiles measured by PIV and hot-wires for the hill flow. (a) Mean velocity, (b) Turbulence intensity. ..... 55

Figure 2.24: Wind direction for ridge configuration. The cross marks the approximate location of the region of interest (Satellite image is from Google Earth) ..... 56

Figure 2.25: Topographic contours and side view of the ridge configuration with horizontal measurement area locations, size and reference coordinates. The rectangle shows the extent of the PIV measurement in the horizontal plane. The thick solid lines in side view correspond to the horizontal measurement planes demonstrated as a rectangle in top view. ..... 57

Figure 2.26: Velocity vectors for the ridge flow in a horizontal plane at $z = 200\text{m}$. ..... 58

Figure 2.27: Velocity vectors for the ridge flow in a horizontal plane at $z = 255\text{m}$ ..... 58

Figure 2.28: t.k.e contours for the ridge flow in horizontal planes [$\text{m}^2/\text{sec}^2$]. (a) $z = 200\text{m}$, 59

Figure 2.29: Crosswind mean velocity magnitude ratios for the ridge flow at three heights and two downstream locations. (a) $z = 200\text{m}$, $x = -84\text{m}$, (b) $z = 200\text{m}$, $x = 98\text{m}$, .....61

Figure 2.30: Crosswind correlations of the mean velocity magnitudes for the ridge flow at three heights and two downstream locations. (a) $z$ = 200m, $x$ = -84m, (b) $z$ = 200m, $x$ = 98m, .....62

Figure 2.31: Comparison of profiles measured by PIV and hot-wires for the ridge flow. (a) Mean velocity, (b) Turbulence intensity. .....63

Figure 3.1: NASA hump model. (a) Schematic of the hump (from Greenblat et al. (2006)), (b) Hump prfoile. .....68

Figure 3.2: Solution domain and boundary conditions for NASA hump test case. .....69

Figure 3.3: Structured grid over NASA hump model. View of the entire solution domain and magnified view of the grid around hump model. .....70

Figure 3.4: Mean velocity profiles at x/c=-2.14. .....76

Figure 3.5: Non-physical separation in leading edge (x/c=0). (a) Contours of velocity, (b) velocity vectors, Flow direction is from right to left. .....76

Figure 3.6: Pressure (a) and skin friction (b) coefficients on the hump surface obtained by SST k-ω and RSM turbulence model. .....77

Figure 3.7: Velocity profiles in four sections over the hump for SST k-ω and RSM turbulence model. C3 and C4 are also compared with measurements. .....79

Figure 3.8: Middle section profile of the three-dimensional hill. .....81

Figure 3.9: Solution domain and boundary conditions for three-dimensional hill. .....82

Figure 3.10: Hybrid grid over three-dimensional hill model. View of the entire solution domain and zoomed sectional view of the grid around hill model. .....84

Figure 3.11: Speed-up ratios (S) for three locations over the hill (hill foot, mid slope and summit).....86

Figure 3.12: Streamwise velocity profiles on four locations on the mid section of the hill (y/L=0) at (a) x/L=0, (b) x/L=0.45, (c) x/L=1.0 and (d) x/L=1.5. The experimental values are from Ishihara et al. (1999).....88

Figure 3.13: Modeling procedure for complex topographic terrains. .....90

Figure 3.14: Southeastern Hong Kong model. (a) Digital elevation model (b) NURBS surface. .....91

Figure 3.15: Streamwise velocity and turbulence intensity profiles upstream of the topography model from hot-wire measurements. .....92

Figure 3.16: Solution domain and boundary conditions for topography models.....93

Figure 3.17: Hybrid grid over topography model. View of the entire solution domain and magnified view of the grid near topography surface.....94

Figure 3.18: Roughness simulation in hill configuration: (a) Roughness blocks in wind tunnel model, (b) Roughness elements implemented in the numerical model, (c) the elements are staggered in an angle to produce maximum frontal area- the camera axis is in direction of free stream. Flow direction is from bottom-left corner to the top-right corner in isometric views (a and b).....97

Figure 3.19: Stream lines in ridge flow released from an upstream rake at the height of (a) $z = 195\text{m}$ (b) $z = 312\text{m}$ .....99

Figure 3.20: Mean vorticity contour plots for the valley flow in a vertical plane at $y = 0$. (a) PIV measurements, (b) CFD simulation. Mean vorticity contours [1/sec], Flow direction is from right to left. .....100

Figure 3.21: Comparison of CFD predicted mean velocity profiles by PIV and hot-wire measurements for the valley flow..... 100

Figure 3.22: Comparison of CFD predicted turbulent intensity profiles by PIV and hot-wire measurements for the valley flow..... 101

Figure 3.23: Mean contour plots at hub height ($z = 50m$) for the hill flow. (a) Velocity magnitude contours [m/s], (b) wind energy coefficient contours. Flow direction is aligned with x-axis. The plots cover an area of 12km×14km..... 102

Figure 3.24: Comparison of CFD predicted mean velocity profiles by PIV and hot-wire measurements for the hill flow..... 102

Figure 3.25: Velocity vectors for the ridge flow in a horizontal plane at $z = 200$m (6cm model scale). (a) PIV measurements (b) CFD simulation. The velocity vectors are superimposed on the topography image. Flow direction is from left to right..... 103

Figure 3.26: Velocity vectors for the ridge flow in a horizontal plane at $z = 225$m (7.5cm model scale). (a) PIV measurements (b) CFD simulation. The velocity vectors are superimposed on the topography image. Flow direction is from left to right..... 104

Figure 3.27: Comparison of CFD predicted mean velocity profiles by PIV and hot-wire measurements for the ridge flow..... 104

## NUMENCLATURE

| | |
|---|---|
| $C$ | chord length |
| $h$ | hill height, characteristic height |
| $I_u$, $I_v$, $I_w$ | turbulence intensity components |
| $k$ | turbulent kinetic energy |
| $L$ | hill radius (generic model), characteristic length |
| $L_X$, $L_Y$, $L_Z$ | boundary distances from the model within simulation domain |
| $S$ | velocity speed-up ratio |
| $U$ | streamwise velocity component |
| $U_\infty$, $U_0$ | free stream velocity |
| $u$,$v$, $w$ | velocity components in x, y and z direction |
| $u'$, $v'$, $w'$ | rms velocity components |
| $x$ $y$, $z$ | Cartesian coordinates |
| $y_{ref}$ | reference crosswind distance used in calculation of correlations |
| $y_{U\,\max}$ | crosswind distance where streamwise velocity component reaches its maximum |
| $Z_s$ | distance along z coordinates measured from surface |

Greek Symbols

| | |
|---|---|
| $\nu$ | kinematic viscosity |
| $\varepsilon$ | rate of dissipation of turbulent kinetic energy |
| $\omega$ | specific dissipation rate |

Dimensionless group

| | |
|---|---|
| $Re$ | Reynolds number based on the free stream velocity |
| $R_{uu}$ | spatial correlation for the streamwise velocity components |
| $u_\tau$ | friction velocity |
| $y^+$ | dimensionless wall distance |

# 1 Introduction

## 1.1 Background

Wind mapping is of utmost importance in various wind engineering, wind environment, and wind energy applications. The wind maps provide the users with wind data over the regions of interest. The wind data can be obtained by direct measurement, wind tunnel experiment, computer simulation or a combination of the abovementioned methods. Each of the methods has its own advantages and limitations.

Direct measurement of wind speed over an area requires a number of anemometers to record the wind data for a long period of time to produce a wind map of the area. The collected data are limited to the locations of the anemometers; hence, detailed wind data in the rest of the area must be extrapolated from the measured data points.

Wind tunnel testing can be very helpful to measure the wind data over a scale model of the desired area. Using advanced measurement techniques, one can obtain the flow characteristics in good quality over any location on the topographic model. The limitations of the wind tunnel models are mainly cost of experiments and complication of the measurement techniques. Besides, the scaling issue should always be considered to guarantee a reasonable connection between the scaled experimental model and the existing site.

Numerical modeling is one of the best tools to create large scale wind maps. Meso-scale atmospheric models have been vastly used for the purpose of weather prediction. These models provide excellent mapping with horizontal resolution of approximately 5×5km at heights above 3-5km. The data can be easily extrapolated to generate wind maps near the surface. However, the extrapolations are only valid if the surface is flat and no complex topographic features are

involved (i.e. off-shore sites or plain areas). Unfortunately, these types of flat terrains are not of high interest for setting up wind farms (Stangroom 2004). Moreover, the horizontal resolution of 5×5km is relatively low compared to the size of typical wind farms. To achieve higher vertical and horizontal resolution in simulations, Computational Fluid Dynamics (CFD) models should be used. These models can be used to determine the flow characteristics over a smaller area while keeping all the complex topographic features of the surface that were not considered in the meso-scale models.

While the meso-scale mapping provides good preliminary information for locating a wind farm, the individual location of wind turbines (micro-siting) is determined based on the detailed wind mapping of the site. In wind engineering applications airport data is used as input. However, airports are usually situated in flat terrain and the use of these data for sites situated in topographic terrain is more or less subjective. Therefore detailed topographic terrain mapping is important in providing site-related wind data and defining mean and fluctuating velocity correlations between various locations in complex topographic terrain.

Several researchers have investigated the wind flow over different types of topographic features using various measurement tools and modeling techniques. The following sub-sections provide a brief review of their research.

## 1.2 Experimental Approach

### *1.2.1 Full Scale Measurements*

Naess et al. (2000) performed mean wind speed measurements at the lee side of two mountain ridges and a reference point upstream of those features. They used propeller anemometers and direction vanes and recorded 10 minutes samples of the wind velocity

at the mentioned three sites. The data was statistically processed to calculate the gust factors.

Holmes et al. (1997) measured the wind speeds at the top of a 380m high escarpment and a reference point upstream of the escarpment to obtain the topographic multiplier corresponding to this type of topographic feature. They used two cup-anemometers along with direction vanes installed on a communication tower. Three measurement points (32m, 45m and 69m high) were reported for a wind direction aligned with the tower and steepest face of the escarpment.

Mason (1986) studied the mean and turbulent flow characteristics over an isolated hill. The hill was almost round with diameter of approximately 450m and height of 76m and covered by short grass at the southern slope that was instrumented. The terrain upstream of the slope was covered by short grass interspersed with hedges and ditches. The mean wind speeds were measured over ten sites at the height of 8m and wind profiles were taken at three sites. Turbulence measurements were taken at the summit of the hill using hot film turbulence probes as well as three-component propeller anemometers.

Taylor and Teunissen (1987) reported the field experiments performed to study the flow over Askervein Hill which is a low hill with a smooth geometry in their review paper. Different groups of scientists collaborated in this study. Askervein Hill is a well exposed coastal hill in Scotland, covered mainly by grass and heather. The hill is elliptical (major axis 2km, minor axis 1km) and 116m high. Over 50 towers were mounted to measure the wind data on and around Askervein Hill. The majority of the towers were 10m high, equipped with cup anemometers. There were two 50m towers, a 30m tower, a 16m tower as well as thirteen 10m towers that were able to record three-component turbulence data.

Due to the simple geometry of Askervein Hill, its coastal location and suitable surface roughness, the results of Askervein Hill study have been vastly used as benchmark for wind tunnel and theoretical hill models.

Grant and Mason (1990) used a series of instruments connected to a tether cable holding a balloon. The balloon was flown in valleys while turbulence data were collected simultaneously along the cable for several heights using six probes that each included three propeller anemometers. The wind speeds were measured using the system up to the heights of 1500m and were verified by a Doppler acoustic sounder up to the heights of 820m. The measured velocities were corrected for the cable oscillation by calculating the instantaneous acceleration of each probe relative to the ground. The balloon was flown along a path experiencing valleys, series of ridges and complex topographies with the mean ridge-valley depth of about 270m. Taylor et al. (1987) and Finnigan (1988) are comprehensive reviews that have summarized a number of field experiments and wind tunnel experiments for flow over hills.

Full scale measurements provide the researchers with a source of benchmarking data to develop and calibrate the numerical, statistical and CFD models. However, the full scale measurements are very expensive and time consuming and in most cases only point measurements are feasible. Moreover, it is usually impractical to perform four-season field measurements over a large area for the sole purpose of wind turbine micro-siting.

### *1.2.2 Wind Tunnel Testing*

The wind tunnel modeling of topography has always been a challenge in terms of scaling the atmospheric boundary layer, turbulent flow structure, terrain roughness and the geometry itself. To measure the flow properties over large complex topography models,

novel techniques must be utilized. There have been several studies of the flow over simple geometries in relatively small wind tunnels while only a handful of wind tunnel experiments have been performed over complex topographies.

Ngo and Letchford (2009) measured three-component velocity profiles and turbulence parameters for different generic ridge, escarpment and cliff models by a 4-hole conical pressure probe. Lubitz and White (2007) used a single hot-wire probe to measure wind speed-up factors over generic hills in different wind directions and compared them with their field measurements. Bowen and Lindley (1976) and Pearse (1982) used hot-wire measurements to determine the flow field over generic escarpments and conical hills. Takahashi et al. (2002) obtained mean and turbulent velocities over a two-dimensional hill using hot-wire anemometer with a split fiber probe that measures all three velocity components. Ferreira et al. (1995) and Kim et al. (1997) employed surface pressure, Particle Image Velocimetry (PIV) and Pitot tube measurements for single two-dimensional hills. Miller and Davenport (1998) investigated the flow over multiple two-dimensional hills and complex terrains using hot wires and compared the results with linear flow analysis.

Ishihara et al. (1999) and Ayotte and Hughes (2004) measured velocity profiles over three-dimensional hill models using hot wires and three-dimensional laser Doppler velocimetry (LDV), respectively. Simpson and Byun (2002) used three-orthogonal-velocity-component LDV system to measure flow properties in a vertical plane behind an axisymmetric hill. Garvey et al. (2005) performed mixed hot-wire and PIV measurements for isolated valleys. Rodrigo et al. (2007) used PIV for a generic representation of forest cuts in a wind tunnel simulating the atmospheric boundary layer. Recently Chock and

Cochran (2005) performed velocity measurements using hot-wire probes over a complete topographic model of Hawaii and Guam regions.

Although hot-wire anemometry is capable of measuring instantaneous velocities, it is an intrusive method which might affect the velocity field. Hot-wires are also known to be insensitive to flow direction which affects the mapping of reverse flow regions such as separation-reattachments or wakes. Split-fiber probes overcome this limitation allowing highly localized flow measurements near the surface and in recirculation areas (see Takashi et al. 2002; Kondo et al. 2002; and recently Cao and Tamura 2006). Laser Doppler Velocimetry (LDV) is a non-intrusive method (e.g. Takahashi et al. 2006), but similar to hot-wire anemometry and split-fiber probes, it can only measure velocity at one spatial position at a time. Therefore, simultaneous mapping of wind speeds in a plane (horizontal or vertical) is not possible unless several probes are used simultaneously. Even in such case, the spatial resolution would still be very low. For specific wind energy and environment applications such as the flow around wind turbines in a wind farm or the flow around urban structures, where the detailed characterization of the spatial distribution of the wind field is crucial, hotwire and LDV techniques may therefore not be the best options. Similar to LDV, PIV is a non-intrusive technique; however, it can measure velocity vectors at thousands of locations in a plane simultaneously. That is, providing flow mapping over extended areas at the same time. While the sampling frequency of typical PIV systems is still low compared to hot-wires and LDV systems, recent improvements have shown sampling capabilities in the range of 1 to 2 kHz.

**PIV Technique for Large Scale Wind Tunnels**

PIV and also LDV measurement techniques require tracer particles within the flow under investigation to compute the flow velocity. In PIV, the images of the tracer particles acquired by the camera are used to compute the particle shift and hence the velocity field. Whereas, in LDV, the light reflected by the particles as they pass through the fringed measurement volume provides the velocity estimate. Therefore, the proper distribution of tracer or seed particles within the measurement region is crucial for reliable estimates of the flow velocities using these techniques. In a small wind tunnel setup, the uniform seed distribution is usually not a big issue. However, in a large wind tunnel setup, the proper seed distribution is a major challenge. Due to the large dimensions and the flow volume, the seed is typically added to the flow locally. In LDV, the flow velocity is measured at a spatial location within a measurement volume whose dimensions are in the order of microns. Therefore, proper seeding is usually not a serious issue. However, for PIV, the dimensions of the measurement plane are typically in the range of 10-20 cm and the proper seed distribution within this region becomes a major challenge. The areas of low seed density within the measurement plane result in the inaccurate estimation of the flow velocity. Although non-uniform seed distribution is an important issue in a large setup, very few studies have reported the non-uniform seed distribution issue.

Zhu et al. (2006) studied the turbulence characteristics within and above a canopy in the field and laboratory using PIV. In the field setup, the seed was added locally for the PIV measurements. The PIV measurement region was 18.2 cm × 18.2 cm. They reported non-uniform seed distribution within the measurement region. They used a correlation coefficient threshold and discarded velocity vectors with the correlation coefficient less

than the threshold. In their wind tunnel setup, due to the smaller cross-sectional area of the wind tunnel, they did not report any issues with the seeding. Lawson et al. (2002) conducted PIV and LDA measurements to study ground vortex flow in a wind tunnel. The PIV measurement region was 25 cm × 25 cm. A raw PIV image from the data showed regions with almost no seed particles in the upper and left portions of the measurement region. They did not discuss the seed distribution issue; however, the velocity plots indicate that the upper and left portions with low seed density were excluded. Their spectral analysis showed consistent results with PIV and LDA in the low frequency range but due to the lower sampling frequency, the PIV data was not able to capture high frequency content of the spectral energy. In several large wind tunnel experiments, planar Doppler velocimetry or Doppler global velocimetry has been used. This technique measures the components of velocity in a plane based on the Doppler shift due to the scattering of light by the seed particles in the flow. Mosedale et al. (2000) discussed the use of this technique in a large-scale wind tunnel. McKenzie and Reinath (2005) discussed the seeding issues within the measurement region in the large wind tunnel setup. They observed that the seeding plume breaks into separated eddies causing intermittent seeding in the measurement region. In the majority of images, they observed that the seeding was present in isolated regions whose fractional area was significantly smaller than the total measurement area. In each image, the regions with valid signal were detected by applying a signal threshold. Ferreira et al. (1995) and Rodrigo *et al.* (2007) used PIV for a generic hill and a representation of forest cuts, respectively. However, they did not report any issues related to seeding which is likely due to the smaller dimensions of the wind tunnel in their experiments. Due to the critical nature of

seeding problem in a large setup, there is a need to develop a robust method to detect the regions with adequate seeding and obtain reliable measurements within the region of interest.

The PIV method has proven to be a practical and reliable measurement technique for wind flow past different models with high spatial resolutions. However, the available wind tunnel studies are mostly limited to small models and generic topographic features due to complexity of the experimental setup and distribution of seed particles.

## 1.3 Numerical Approach

### *1.3.1 Meso-scale Numerical Simulations*

Meso-scale atmospheric models as mentioned in section 1.1 have been used for weather prediction and creating wind maps. The meso-scale models use realistic boundary conditions to produce weather simulations or predictions for specified time periods on grids with the minimum resolution of approximately 5km. Among meso-scale models, the Weather Research and Forecasting (WRF) Model is one of the most developed models that has replaced it predecessor, MM5 model. WRF model is a numerical weather prediction system which is designed for forecasting and atmospheric research needs.

Finardi et al. (1998) used two different meso-scale models to simulate flow field over a complex terrain (Appennini Mountains) and compared the results with their field measurements. The area was a square of 15km with the maximum elevation change of 600m dominated by a hill-like structure. First, they used a mass consistent model (MINERVE) with horizontal resolution of 250m that interpolates the wind observations at known stations and then adjusts the flow field. Next, they used a non-hydrostatic

model based on a full set of compressible primitive dynamic equations (RAMS) using the meteorological input data over 240×240km, 50×50km and 15×15km nested grids. The final grid resolution was 250m horizontally. They found the mass consistent model to be sensitive to the topographic position of measurements. Also, having properly sited stations to initialize the model is critical. The non-hydrostatic model results proved that employing grid nesting to start the simulations from larger synoptic meteorological fields is an acceptable method to obtain local scale wind fields.

Mochida et al. (1997) used a CFD model with an algebraic second-moment turbulence model developed for geophysical flow problems to resolve flow field over Greater Tokyo Area. The area had complex topography of varying elevations from 0 to 1.6km. They used a grid computational domain of 480×400km×5km with horizontal resolution of 8km and 20 levels in vertical. They examined the simulation results over the urban areas and reported that the land use and surface roughness play an important role in the validity of the CFD results.

Rognvaldsson and Olafsson (2005) used the MM5 meso-scale model to simulate the wind flow over Iceland and compared the results with the available measured wind data over sites close to different topographic features. The simulations were performed on a grid with horizontal resolution of 8km and 23 levels in the vertical for a period of six month. They observed significant discrepancies near a site that was on a 120m high cliff as well as a site that was at 50m altitude; the rest of the predicted results were in acceptable agreement with field measurements since the real topography and the simulated topography were more similar to each other close to the measurement sites. The discrepancies at the latter site were due to the limitation imposed by the vertical grid

resolution with the first grid point at 150m from surface. Tong et al. (2005) used a similar approach to simulate wind fields over Hong-Kong which is characterized by 75% mountains, complex coastline and numerous islands. The area under study was 1000km$^2$ and the nested grids had the resolutions of 27km, 9km and 1km. The simulation results were compared with observations from six stations and they were found to be under estimating the diurnal values. The discrepancies were explained to be as a result of low grid resolution compared to the complexity of the topography. Some of the meso-scale models have also been integrated with theoretical micro-scale models to provide general wind energy assessment models that to some extent are able to incorporate the terrain and topography. Wind Atlas Analysis and Application Program (WAsP) (see Troen and Peterson (1989)) and Wind Energy Simulation Toolkit (WEST) (see Yu et al. (2006)) are examples of the integrated models to create numerical wind atlases in Europe and Canada, respectively.

Meso-scale models are among the most efficient weather and wind prediction/simulation tools that have been successfully used for several cases. But when it comes to simulation of wind over topographic terrain, most of them rely on simplified micro-scale models which results in larger errors in the wind velocity field predictions. Moreover, the typical grid resolution for meso-scale models is 5km which is very coarse compared to features existing in complex topographic terrain. Meso-scale models can be very helpful in providing boundary conditions for the CFD studies and upstream conditions for wind-tunnel test (PIV measurements) to provide high resolution wind maps over local topography.

### *1.3.2 Micro-scale Numerical Simulations*

Linear models which are typically developed based on simple models for turbulence and roughness can provide a quick analysis of the mean wind flows for hilly terrains. Jackson and Hunt (1975) provided linear models for isolated hills with low slopes in turbulent boundary layer flows. This study has provided the foundations for development of linear models for topographic terrain. Hunt et al. (1988) examined those models for a wide range of upstream velocity profiles for turbulent shear flow analysis. Lemelin et al. (1988) and Cook (1985) presented formulations to predict the maximum speedup for different hill profiles using the linear models. Miller (1996) studied the flow over multiple two-dimensional hills and complex terrains with the linear models and in wind tunnel to provide a model of behaviour for flow over complex topographic terrain.

Although the linear models can provide quick estimate of wind flow over topography, they are limited to low slope hills and are not valid for recirculation regions.

CFD modeling is one of the best approaches to the problem of simulating flow field over topography in micro-scale, near the surface. In micro-scale, the numerical modeling of the flow field consists of utilizing the Navier-Stokes differential equations in a particular domain around the topography. The Navier-Stokes equations must be discretized within the time and space domain to be able to provide a reasonable reproduction of the flow field. Direct Numerical Simulation (DNS) is the most accurate approach to solve the Navier-Stokes equations; however, it requires a large computational resource and great amount of time to resolve the flow field. Large Eddy Simulation (LES) models small scales of turbulence in the flow and leaves the rest of modeling procedure to the Navier-Stokes equations; although it runs faster than DNS, it is still requires a lot of resource and

time. Reynolds Average Navier-Stokes equations (RANS) assume the flow parameters to have a mean and fluctuating component in which the fluctuating components are representatives of the turbulence in the flow. Closure models (aka turbulence models) are needed to solve RANS equations to have a complete set of equations. The RANS equations might not be able to completely resolve the flow field parameters and turbulence; however, it is a lot less resource intensive to employ them to simulate a large domain.

There have been many studies focusing on CFD simulation of generic topographic features using different turbulence models. Some researchers have simulated flow over more complex structures such as multiple hills or real hill models; however, only a few of them have attempted to resolve the flow field over a complex topographic terrain.

#### 1.3.2.1 Generic Topographic Features

Flow over a simple sinusoidal hill has been of interest as a CFD study case because of their geometry simplicity while demonstrating close flow pattern to flows over similar real topography. Lun et al. (2003) studied the flow over a two-dimensional simple cosine shape hill and a forward-backward-step representing a cliff. They compared available experimental results with standard k-ε turbulence model results as well as two modified k-ε models. They observed discrepancies between experimental results and simulations within the area of separation bubble as well as an area 0.5h (h: height of the cliff) downstream of the edge of forward-step. They extended their study to two more modified k-ε models and different backward-forward-slopes (see Lun et al. (2007)). Kim et al. (1997) performed wind tunnel experiments and CFD simulations (a low Reynolds model and standard and RNG k-ε turbulence models) on a cosine shape two-dimensional hill

and two-dimensional double hills. In addition to problems addressed by Lun et al. (2003), the simulated velocity profiles by Kim et al. (1997) demonstrate higher streamwise velocity at the heights about 5-15cm (1.5-3.5h- h: hill height) above the ground with the low Reynolds turbulence model showing more discrepancies. Maurizi (2000) used three versions of k-ε turbulence models to simulate the flow past generic two-dimensional valleys and found the RNG model producing more acceptable results. Ishihara and Hibi (2002) studied the flow over a three-dimensional sinusoidal hill model using the standard k-ε model and a Shih's nonlinear model. They examined the flow patterns behind the hill as well as the turbulent characteristics of the flow and found Shih's model predicting the turbulence parameters better than k-ε model.

NASA hump is another well benchmarked problem and an excellent test case as it involves regions of impingement, boundary layer, separation and reattachment. It was originally designed for the study of flow separation control; however, experiments were also carried out for the no-flow control cases and results such as surface pressure, surface friction and velocity profiles (PIV measurements) were used as benchmark to investigate the performance of several numerical modeling schemes (Seifert and Pack (2002); Naughton et al. (2004, 2006); Greenblatt et al. (2004, 2005, 2006)). Viken (2003) used two-dimensional and three-dimensional CFD solvers employing Thin-Layer Navier-Stokes (TLNS) equations and RANS equations with Spalart-Allmaras (SA) turbulence model. Based on experimental and CFD results, Viken observed that the incoming boundary layer thickness does not have much effect on separation and reattachment point and used free stream inflow instead of the measured profile at the wind tunnel (also stated by Saric et al. (2006) for RANS simulations). Iaccarino et al. (2003) used SA, k-ε and k-

ω model, Morgan et al. (2006) employed k-ε with fourth-order spatial discretiziation. Krishnan et al. (2006) compared SA and Shear Stress Transport (SST) k-ω turbulence models along with Detached Eddy Simulation (DES). The grid they used for the DES simulations had 3.5 million cells. Saric et al. (2006) compared SA turbulence model, DES and LES. The grid for the DES and LES simulations had 3.9 million cells. Both the latter research works showed considerable improvement in results when migrating from pure RANS models to DES and LES. However, the computational cost is far beyond comparison for DES-LES cases (3.9 million cells) and RANS case (61000 grid cells). You et al. (2005) and Avdis et al. (2009) used LES simulations with the grid sizes of 7.5 and 9.5 million cells, respectively. Postl and Fasel (2006) used a 210 million cell grid to perform DNS simulation for the NASA Hump; their results perfectly matched the experiments. Most of the RANS simulations are observed to be in agreement with the experimental results in the areas upstream of the separation bubble. Mostly, the discrepancies between the experiments and RANS simulation appear in the vicinity of the separation and reattachment region.

#### 1.3.2.2 Simple Topography

As a step forward from CFD modeling of generic geometries, single isolated hills with moderate slope have been at the center of attention. Apsley and Castro (1997) performed CFD simulation for an isolated low hill (Cinder Cone Butte) using standard k-ε model and two modified k-ε models. Stangroom (2004) studied the wind flow Askervein hill using RNG k-ε and RSM turbulence models. The velocity profiles at the hilltop were predicted to have lower velocities compared to the field experiments with RNG model demonstrating larger errors. Also, it was noticed that the turbulence properties are

resolved with very high percentage of error (the simulated turbulence intensity was eight times smaller than the measured value). In other words, the CFD data seemed to agree with general theory of RANS modelling but the full scale data represented more turbulent flow field. Prospathopoulos and Voutsinas (2006) simulated flow over Askervein hill using k-ε model and a fairly coarse grid (horizontal grid spacing: approx. 74m, total of 194000 cells), Kim et al. (2000) used standard and RNG k-ε models on a 210000 cell grid (horizontal grid spacing: approx. 75m), Undheim et al. (2006) used k-ε model on a 2.7 million cell grid (horizontal grid spacing: approx. 10m). Chow and Street (2008) performed LES study and Lopes et al. (2007) performed hybrid RANS/LES study over the Askervein Hill using grids of 1.6 million cells (horizontal grid spacing: 35m) and 10.8 million cells (horizontal grid spacing: approx. 19m), respectively. Lopes et al. (2007) thoroughly examined the turbulent characteristics of the flow and compared the hybrid RANS/LES simulation results with RANS (k-ε turbulence model). They observed the speed-up ratios along a section of the hill predicted with both methods were similar; however, in the upstream side of the hill the hybrid RANS/LES simulations predicted the turbulent kinetic energy better. The k-ε model predicted higher speed-up ratios near the ground (in better agreement with the measurements) but only when a finer boundary layer grid was used close to the surface. Kim et al. (2000) performed CFD simulations (approx. 210000 cell grid, RNG k-ε model) over four different sites, a gentle sloped ridge (Cooper's ridge), an isolated hill (Kettles Hill), Askervein Hill and a valley between two nearly two-dimensional ridges. They indicated the inclusion of the neighbouring hills in the computational domain is important in the prediction of three-dimensionality of the flow on the leeside. The valley model showed the RNG k- ε turbulence model gives

better results compared to standard k-ε model. The Askervein Hill simulations at the hill top did not provide a good prediction of the velocity profiles, but the turbulence kinetic energy seemed to be in good agreement with measurements.

#### 1.3.2.3 Complex Topography

Wakes et al. (2010) created a two-dimensional model of a profile along a complex dune system at a coastal area and performed CFD simulation on it using k-ε turbulence model. They explored different modeling parameters such as roughness height and zoning and inlet velocity profile by comparing the simulation results with field measurements at several sections. The terrain roughness along the studied area varied from sea surface to sand and 0.25m tall grass; however, modeling the varying roughness was found important to achieve acceptable results. Uchida and Ohya (1999) simulated the flow field over a wide area of 25km×25km composed of complex terrain, shore and sea. They used a coarse grid (resolution of 250m in horizontal, 0.5 million cells) with rectangular elements for their unsteady simulations and qualitatively inspected the characteristic features of the flow. Uchida and Ohya (2003) used LES to predict the wind flow field over an area of 9.5km×5km covering complex topography that included mountains of h=244m high. The simulations were based on extremely low wind speeds (Reynolds number in order of $10^4$-based on h). They used a relatively fine grid with horizontal resolution of 50m with the total size of 1.2 million grid cells. The simulation consisted of two units: upstream driver unit and main unit; the upstream unit produced inlet boundary condition for the main unit at each time step. The upstream driver unit consisted of physical roughness blocks simulated at the inlet. The driver unit was 80h long while the main unit was 40h long (h: highest elevation of the area). The airflow patterns were visualized by tracing marker

particles over the flow field and the turbulence characteristics were examined at few points. The results were not compared with wind tunnel or field measurements. Uchida and Ohya (2008) performed wind tunnel tests and numerical simulations (LES) on a two-dimensional ridge, three-dimensional generic hill and a topography model (covering the area of Noma Cape Wind Farm in Kagoshima). The wind farm is located the on summit line of a long narrow two-dimensional-hill surrounded by the ocean. The numerical simulation results were compared with wind tunnel measurements; for the case of real topography field measurement data colleted at the wind turbines were also used in the comparisons. The field measurements data was collected by prop-vane anemometers on the wind turbine nacelles downstream of the hub. Two wind tunnel models with the scale of 1:2800 were built: one with smooth surface and one with serrated surface. They were tested in a small (test section width: 1.5m; height: 1.2m) low speed wind tunnel at the very low speed of 1.5m/s with no boundary layer simulation. No significant influence of serration of the model surface was reported for the wind speeds measured at the hub height (30-45m full scale, 10-15mm model scale) for that specific model and Reynolds number ($6\times10^3$). The numerical domain for topography simulations covered an area of approx. 1.5km wide surrounding the wind farm with a grid size of 5.5 million cells (horizontal grid resolution approx. 10m). The simulations were performed at full scale for Reynolds number of $10^4$ (based on h=143 and inlet velocity) and dimensionless time steps of $2\times10^{-3}$ (it can be deduced the inlet velocity for simulation is approx. $10^{-3}$m/s and time step is approx. 300s- wind turbine rated wind speed was 14m/s). Simulations were performed for 16 wind directions and speed-up ratios were calculated for the low

Reynolds model and field measurements. They were found to be in agreement with annual and monthly average wind speeds.

Although many attempts haves been made for the simulation of wind flow over topographic terrain, most of the studies were limited to generic topographic features. Moreover, studies on CFD simulation of the terrain roughness especially for the urban areas are very few. There is a need to provide an integrated method to set up CFD simulations for wind flow over complex terrain with a wide range of roughness heights in order to generate high resolution wind maps for wind engineering and wind energy purposes.

## 1.4 Scope

Valuable studies have been performed on flow over generic topographic features, and few researchers have focused on wind tunnel and numerical simulation of flow over complex topography. The studies over generic topographic features can be used as benchmark models for CFD simulations and development platforms for creating statistical and linear mathematical models of speed-up velocities. However, the research on modeling the flow over complex topography is in its preliminary stages. The wind tunnel models have been relatively small and the measurements were only limited to point measurement techniques such as pressure measurements, hot-wire anemometer and LDV. On the other hand, previous numerical simulations on complex topography have only been performed on surfaces with smooth curvature located near water surface and uniform terrain with relatively low roughness. In addition, the few existing CFD simulations have been performed on relatively coarse grids (in the order of meso-scale simulation grids). Only Uchida and Ohya (2008) have used LES model on a fine grid

over a smooth topography model; however, the simulation velocity was extremely low to make it possible to use very large time steps, to make the LES study feasible.

This thesis includes measurements in several horizontal and vertical rectangular planes on a large wind tunnel model of complex topography of southeast Hong-Kong using PIV technique. Application of PIV technique to velocity measurement in large wind tunnels is very challenging due to several issues including problem of seeding particles and experimental setup. The capabilities and limitations of PIV measurements for complex topographic terrain are investigated. The measurement results are explored to advance understanding of the effects of realistic topographic features on the mean and turbulent wind fields. CFD simulations on the same topography model in wind tunnel scales are also presented. The topography model is very complex in terms of surface shape (consists of several hills, valleys and ridges up to 530m high) and terrain roughness (ranging from water surface to urban area consisting of dense high rise buildings).

In detail, the present study consists of evaluation of different CFD modeling techniques using commercial CFD software, focusing on simulation of wind flow over complex topography. Generic two-dimensional and three-dimensional benchmark models are numerically simulated and a 1:3000 scale model of complex topography of southeast Hong-Kong is tested in wind tunnel to serve as benchmark for CFD simulations.

In chapter two, the wind tunnel model of Hong-Kong is introduced. Hot-wire and PIV measurements are described in detail and the measurement results are presented for three different topographic features selected from the complex model.

Chapter three presents benchmark testing of the two-dimensional and three-dimensional generic hump and hill models. Different approaches to numerical model setup are

explored and the best ones for flow modeling over topography are identified. The numerical simulations for the wind tunnel model of the real topography of southeast Hong-Kong are presented and the predicted results are compared to wind tunnel measurements.

Finally in chapter four, conclusions and recommendations as well as future work are presented.

# 2 Experiments

## 2.1 Introduction

This chapter presents the experimental study that was conducted on a 1:3000 topography model of southeast Hong-Kong. The model represents an area covering complex topography, water surface and urban area. The objectives of the experiments are listed as below:

- To demonstrate PIV's capability to provide a detailed characterization of the flow field over complex topographic terrain in a large boundary layer wind tunnel setup.
- To create benchmark cases of flow over three significant topographic features to be used in evaluating CFD simulations presented in the next chapter.

PIV measurements are performed for several horizontal planes at various elevations as well as for vertical planes corresponding to several topographic features. Three topographic features are investigated: a valley, a hill and a ridge. The mean and turbulent wind velocity fields are analyzed in relation to the local and dominant topographic features. Crosswind mean velocity ratios are determined for the three cases at various heights. For each case the PIV measurements are compared with previous hot-wire measurements performed at the same locations (Ho and De Leebeeck (2004), Farquhar and Ho (2004)). The non-uniform seed distribution due to large size of the wind tunnel and flow complexity was found to be a major issue which could affect the PIV velocity vectors. A novel scheme (Siddiqui et al. (2008)) is used to automatically detect the regions with low seed density and exclude them from further analysis. The study shows

that PIV can be successfully used to measure flow over complex geometries in large wind tunnel setups, enabling to map the flow structure with very high spatial resolution.

## 2.2 Experimental Setup

### *2.2.1 Wind Tunnel*

The experiments were performed in the Boundary Layer Wind Tunnel II (BLWTL II) at the University of Western Ontario. BLWTL II is a closed circuit wind tunnel with two major test sections: a high speed and a low speed (Figure 2.1). The low speed section of BLWTL II is 4m high, 5m wide and 52m in length. The maximum wind speed in this section is 36km/h (10m/s), however a wind speed of 27.4km/hr (7.6m/s) was used based on the hot-wire measurements reported by Ho and De Leebeeck (2004) and Farquhar and Ho (2004). The free-stream velocity was measured at the centerline of the wind tunnel by a pitot tube at the height of 1.8m that corresponds to the full-scale height of 5400m.

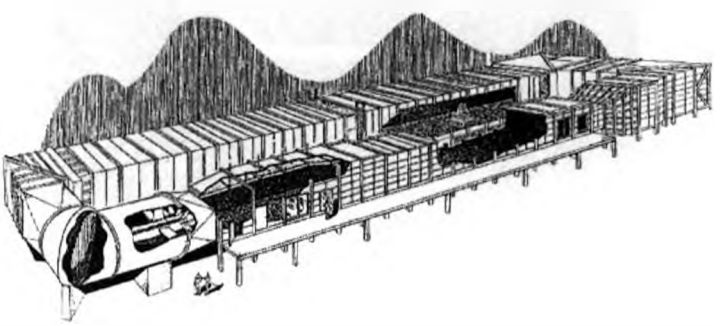

Figure 2.1: BLWTL II, Boundary Layer Wind Tunnel Laboratory, University of Western Ontario.

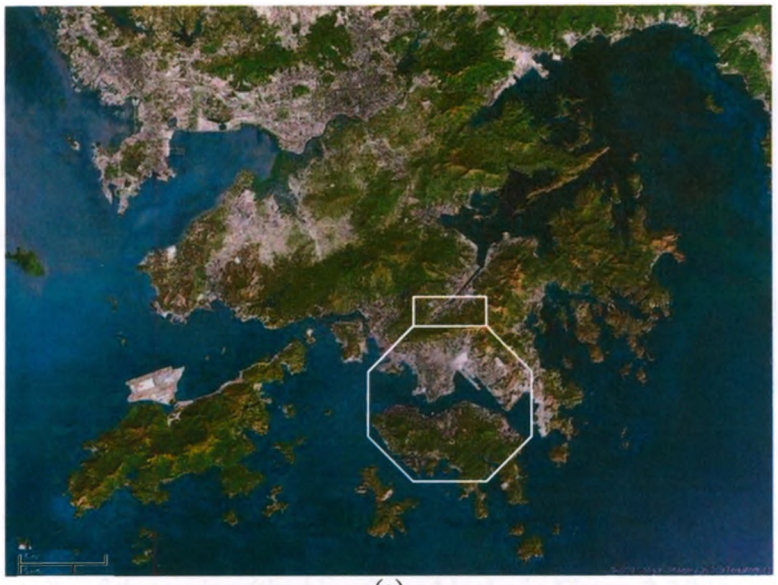

(a)

(b)

Figure 2.2: Google Earth satellite images of Hong Kong: (a) Extent of the topographic model, (b) Southeast Hong Kong.

### *2.2.2 Topographic Model*

The topographic model of Hong Kong area was built at a scale of 1:3000 that covers an equivalent full scale area of 14 km in diameter. Figure 2.2(a) shows the extent of the model on a satellite image of Hong Kong. The model represents the Hong Kong Island and Kowloon peninsula north of the island (Figure 2.2(b)). This area includes the terrain

around two points of interest i.e. a valley/ridge (Happy Valley) and a hill (Victoria Peak). Both locations are subject to upstream conditions with a combination of open areas, built-up urban areas and mountains.

The model diameter is approximately 4.8m, enabling it to fit in BLWTL II low speed test section. The model is made by carving high density foam in several 7mm steps which correspond to equivalent 20m full scale elevation contour lines. The resulting serrated model was sanded to have rounded edges (Figure 2.3(a)). The buildings were included as generic foam blocks to represent the built-up areas in addition to the terrain and topographic details of the region (the blue foam blocks in Figure 2.3(b)).

Considering the model scale of 1:3000, wind tunnel speed of 7.6m/s and the full scale wind speed calculated by Ho and De Leebeeck (2004), hot-wire measurements with sampling rate of 500Hz correspond to sampling rate of 1.5Hz in full scale which also indicate the time scale is 1:333.

The model has a hexagonal shape and was placed on the turntable of the wind tunnel in the low speed section that allows easy rotation of the model in order to change the wind direction. Three configurations were selected for measurements corresponding to a valley, a hill and a ridge with respect to the wind direction, see Figure 2.4.

#### 2.2.2.1 Valley Configuration

Happy Valley in Hong Kong Island was selected as the first topographic feature. The valley belongs to a mountain range located near the shore in the Hong Kong Island. The surrounding mountains range from 250m to 400m in height (8cm to13cm model scale). The wind direction was set such that wind blew from the urban area on the mainland north of the harbor to the water surface (the harbor between mainland and the island), to

the urban area on the island and finally to the valley (see Figure 2.4(a)). The hot-wire measurements were available on a point 32m (1cm model scale) above the sea level slightly off the valley centerline. Hereinafter, the flow in this configuration is called the "valley" flow.

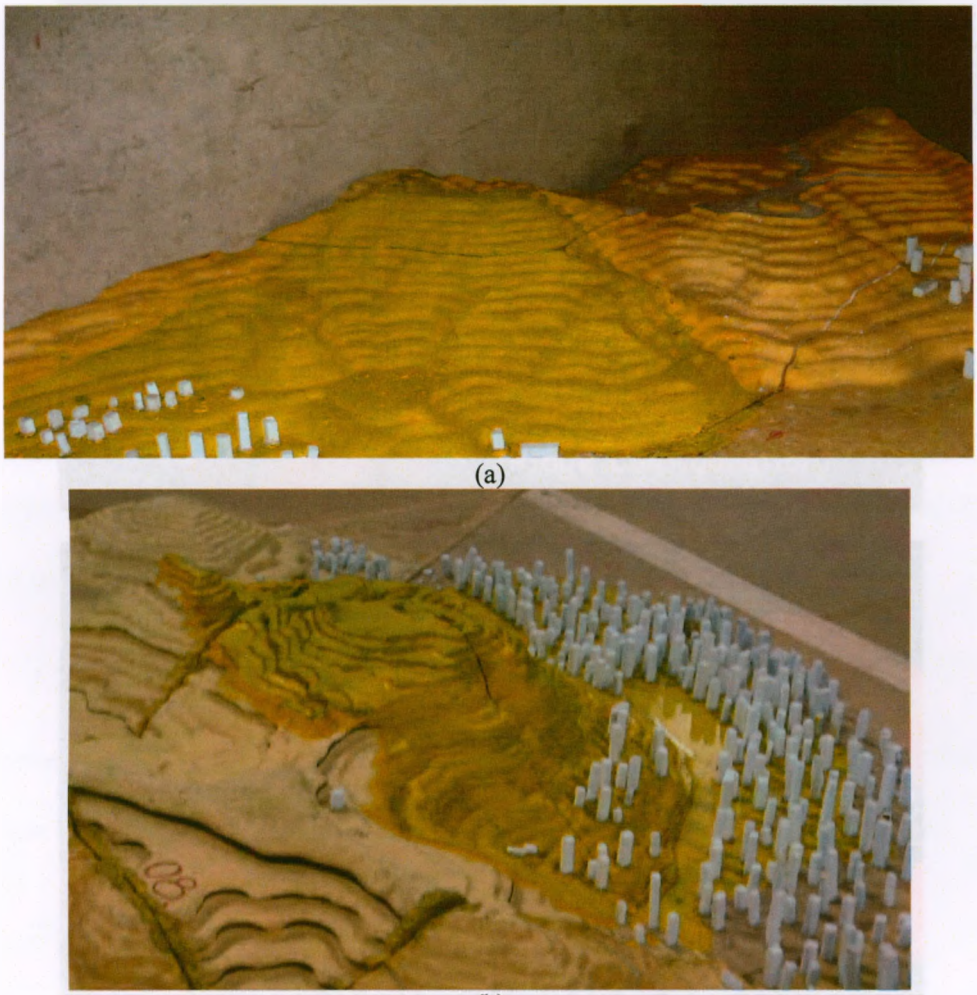

(a)

(b)

Figure 2.3: (a) Model surface. (b) Foam blocks representing the built-up areas.

2.2.2.2 Hill Configuration

For the hill configuration, the model was oriented in a direction so that the wind blew from the urban area on the mainland to the channel, to the urban area on the island and

finally to Victoria Peak (see Figure 2.4(b)). The Victoria Peak is a relatively isolated high slope approximately 520m in height (17cm model scale). This flow is referred to as the "hill" flow.

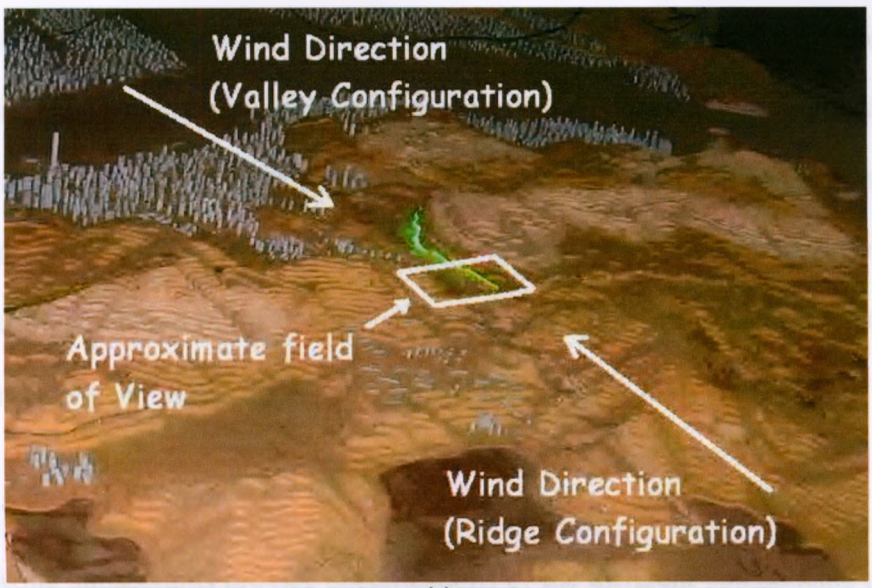


(a)

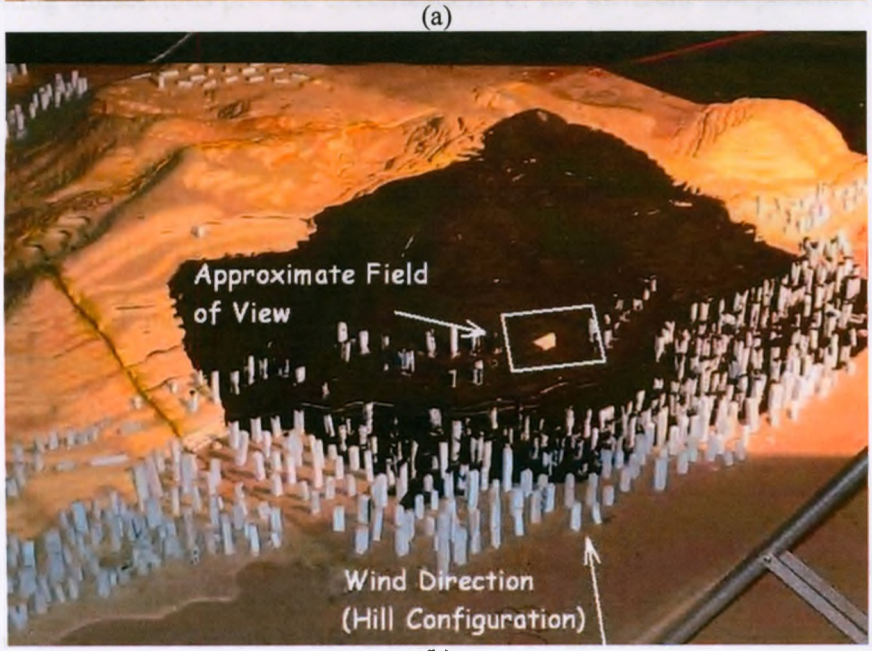


(b)

Figure 2.4: Selected topographic features and wind tunnel configurations corresponding to them. (a) Valley and ridge configurations, (b) hill configuration.

#### 2.2.2.3 Ridge Configuration

For the third configuration, the wind blew from the mountains in the Hong Kong Island over a ridge to the Happy Valley to the low elevation urban area on the island, to the harbor and finally to the urban area on the mainland (see Figure 2.4(a)). The ridge is neighboring the Happy Valley and is 350-400m in height. The flow in this configuration is called the "ridge" flow. The hot-wire measurements were available at the same point as referenced for the valley flow. In essence the "ridge" flow corresponds to the opposite flow direction compared to the "valley" case. The ridge flow measurement is particularly important since it can assess the capability to predict reverse flow in the valley.

### *2.2.3 PIV System*

The following subsections provide specifications of the different components of the PIV system used for the wind tunnel measurements.

#### 2.2.3.1 Laser

A Continuum Minilite-PIV 25mJ Nd:YAG laser was used as the light source which has two laser heads with maximum repetition rate of 15hz and wave length of 532nm.

#### 2.2.3.2 Optics

A cylindrical lens was used to create a laser light sheet with the laser beam. Since the thickness of the laser light was suitable for the experiments the use of a spherical lens was not necessary. For the cases of vertical plane measurements, an optical mirror was used to deflect the laser beam.

#### 2.2.3.3 Seeding System

For PIV measurements, the flow under investigation is seeded. For airside PIV measurements, the flow under investigation is typically seeded with an oil mist. Due to the sticky nature of oil droplets which were not desirable for the present topographic model and wind tunnel, Bis-(2-ETHYLHEXYL) Sebacate mist with the mean diameter of 0.5 μm was used as the tracer particles, which is nontoxic and less sticky than the oil mist. The mist was generated using an air pressure driven aerosol generator (LaVision Inc., Ypsilanti MI). The particle size was determined by the nozzle size and the rate of particle concentration was controlled by the inlet air pressure to the seed generator. Due to very large dimensions of the wind tunnel (total volume equal to 2000 $m^3$), seeding the entire air circulating through the wind tunnel was extremely difficult. Therefore, seeding was added locally to the flow. However, the particles should be introduced to the flow field without disturbing the main flow field or interfering with the topography model. Moreover, to achieve high signal to noise ratio of the PIV images, the seed should be distributed uniformly with appropriate density. A specially designed seed distributor was built to optimize the presence of particles in the measurement areas. The seed distributor is a 22cm long, ½in. PVC pipe with sixteen 4mm holes evenly distributed along it (see Figure 2.5). The length of the distributor and the hole size were adjusted to gain desired seed concentration without disturbing the flow field.

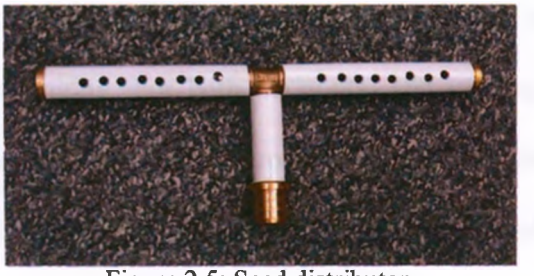

Figure 2.5: Seed distributor.

#### 2.2.3.4 Image Acquisition System

A monochrome camera (JAI CV-M2) with the resolution of 1600×1200 pixels and CCD size of 1″ was used to image the flow for PIV measurements. The maximum frame rate for this camera is 30.2fps and the pixels are squares of 7.4μm$^2$. A lens with focal length of 50mm was installed on the camera to obtain the best PIV resolution for the desired view port size.

The camera was connected to a PC equipped with a frame grabber card (DVR Express, IO Industries, London, ON, Canada) that acquired 8-bit images at a rate of 30 fps. The trigger output of the frame grabber was connected to the input gate of the synchronizer (see the next subsection) and the camera was connected to the frame grabber using a 15ft Camera Link cable. Camera Link enables transferring data from the camera as well as controlling the frame trigger of camera.

A four channel pulse/delay generator (555-4C, Berkeley Nucleonics Corporation, San Rafael CA) was used as the camera-laser synchronizer to control the timing of the laser pulses. The synchronizer input gate was fed from the frame grabber board to trigger the lasers' flash lamps and Q-switches at the desired moment. The time difference between the two laser pulses (or the two image couples) was programmed into the pulse generator.

### *2.2.4 Set-up*

Due to the very large dimensions of the wind tunnel, the setup of the PIV system and the measurements were challenging. For both horizontal and vertical plane measurements, the laser head, the laser power supplies, aerosol generator and the camera were placed inside the tunnel while the rest of the equipment were placed outside the wind tunnel. The

laser, laser optics and camera were placed away from the measurement region to avoid any flow modifications in the region of interest.

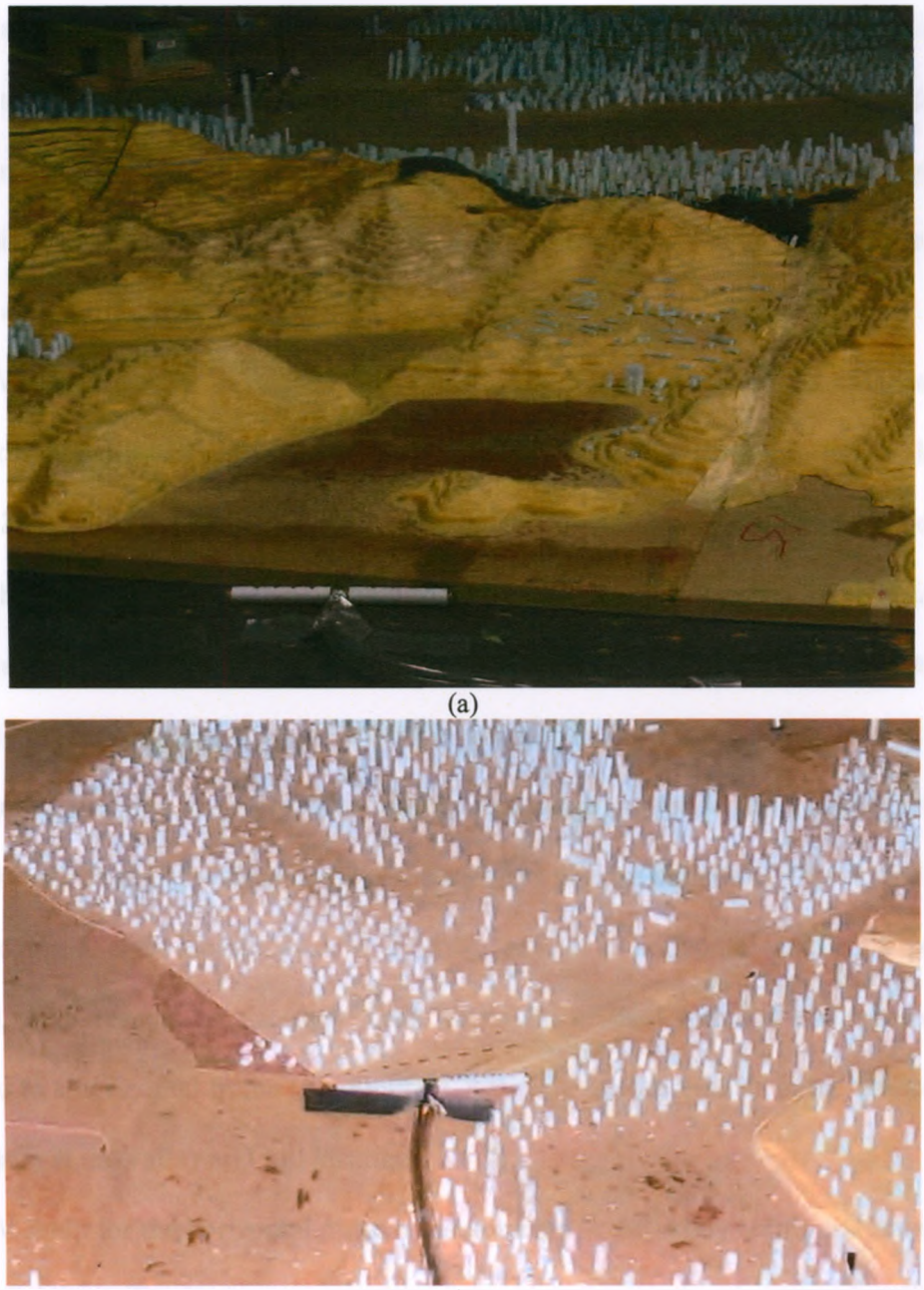

Figure 2.6: Seed distributor location for (a) ridge configuration and (b) hill configuration.

The seed distributor was either placed upstream of the topographic model (flushed with the model's upstream edge) (see Figure 2.6(a)) or among the small foam blocks (Figure 2.6(b) and Figure 2.7(b)). The aerosol generator was placed near the wall of the wind tunnel to minimize its effect on the flow field. A flexible pipe was connected from the outlet of the aerosol generator to the middle of the distributor to transport seed particles. To avoid reflections, the terrains and buildings within and surrounding the measurement region were painted black

The PIV measurements have been performed for both vertical and horizontal planes. The PIV setup for the vertical plane measurements in the valley configuration is shown in Figure 2.7(a). For the vertical plane measurements, the laser was placed on a tripod stand above the topographic model. The cylindrical lens and an optical mirror were mounted on a vertical rod to generate a light sheet in the vertical plane. The camera was mounted on a vertical traverse system through an angle bracket in such a way that it was located upstream of the mounting structure. The camera was mounted in the vertical position to allow measurements in wider angles in normal to ground direction. That is, the images were acquired with the dimensions of 1200 pixels in horizontal and 1600 pixels in vertical, with respect to the flow field. Both the vertical rod and the traverse were attached to a horizontal frame (see Figure 2.7(a)). The measurements in the vertical plane were made at the valley and hill locations.

The PIV setup for the horizontal plane measurements in the valley configuration is shown in Figure 2.7(b). The laser power supplies were placed near the wind tunnel wall and the laser head was placed on one side of the topographic model. The cylindrical lens was placed in front of the laser to generate the light sheet. For the valley configuration, the

only open space on the model for the laser placement was slightly upstream of the measurement location. However, this location was far left from the measurement plane such that any flow disturbance by the laser has no effect on the flow field in the measurement plane. The camera was mounted on the vertical traverse which was attached to a horizontal frame (see Figure 2.7(b)). Both the traverse and the horizontal frame were located downstream of the measurement region and were high enough to avoid any influence on the flow behavior in the measurement region. The measurements in the horizontal plane were made at different heights ranging from 6.5cm (195m full scale) to 12cm (360m full scale). For measurements at the next higher elevation, laser, optics and camera were all lifted. The horizontal plane measurements were performed for all the three configurations: ridge, valley and hill.

For the given setup, the time separation between the two images of an image pair was set equal to 80 μs. For each experimental run, the data were acquired for one minute (i.e. 1800 images). This provided 900 velocity fields for each of the sixty second runs.

One of the biggest challenges faced during the experiments was the proper seed distribution. Due to the high free stream velocity, the large dimensions of the wind tunnel and the complex topolography it was observed that the seed distribution was not fully uniform at higher elevations. For the PIV velocity computation, non-uniform seed distribution is not a critical issue as long as in any particular interrogation region, the seed density is large enough to obtain a strong correlation peak. However, insufficient or negligible seed particles in a region result in an inaccurate velocity vector. An algorithm was used to automatically detect regions with insufficient seed densities, which were excluded from the rest of analysis.

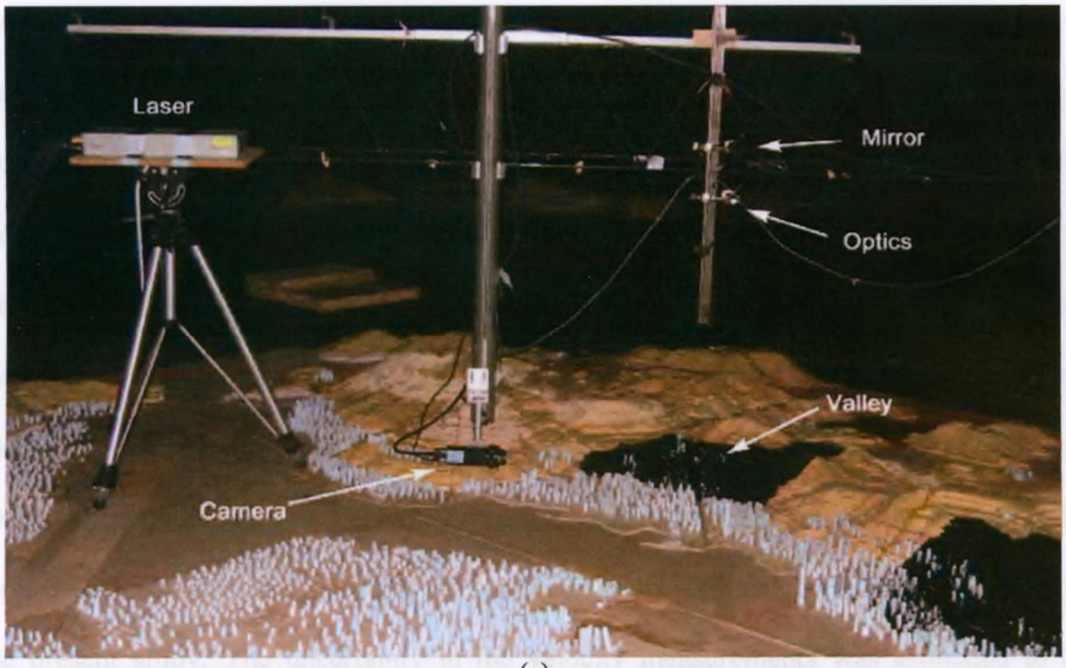


(a)

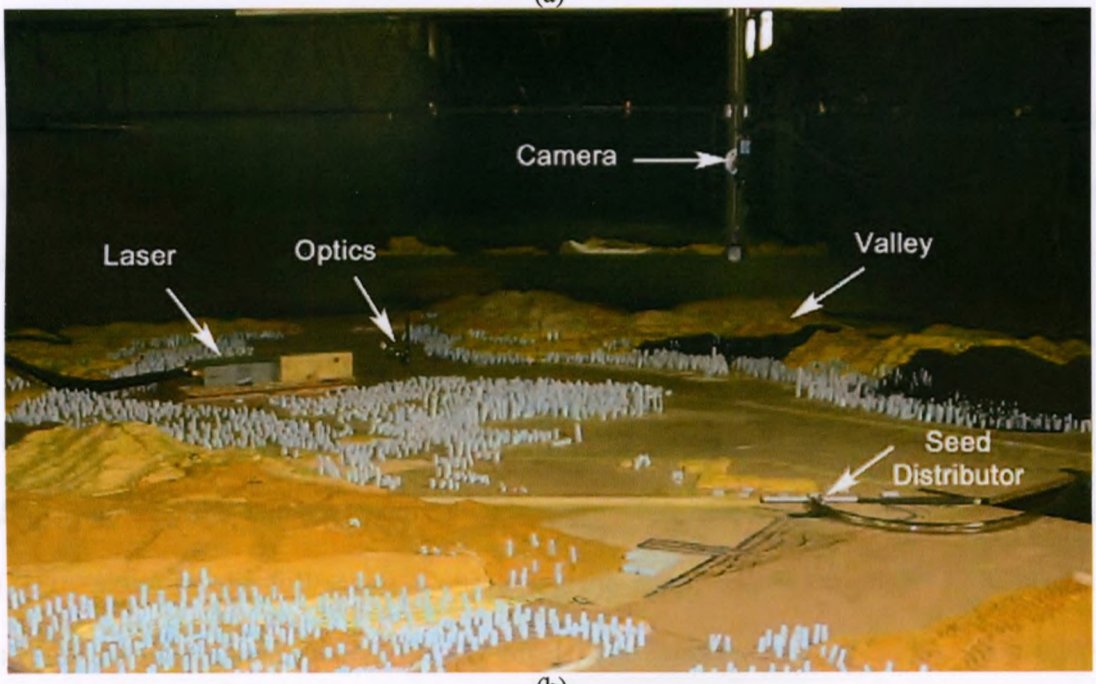


(b)

Figure 2.7: PIV system setup for (a) vertical plane measurements, (b) horizontal plane measurements. The images belong to valley configuration.

PIV velocity fields were obtained by cross-correlating the interrogation region in the first image with the corresponding search region in the second image of an image pair. In the

present study, the size of the interrogation region was set equal to 32×32 pixels and the size of the search region was set equal to 64×64 pixels. A 50% window overlap was used in order to increase the number of velocity vectors. This provided approximately 7000 velocity vectors in each velocity field. However, the Nyquist wavelength of the velocity data, i.e. the smallest length scales resolved by velocity field, is 64 pixels which is based on the interrogation window size (32×32 pixels). Hereinafter, these velocity fields are termed as raw velocity fields as no corrections have been made yet to remove any false vectors. The uncertainty in the velocity measurement was computed for the case with the largest velocity gradients. This provides a conservative estimate of the velocity errors in the present study. The uncertainty in the velocity measurements was estimated to be about 8%.

In the following subsections, the extent of the PIV measurements in horizontal and vertical planes is presented. Moreover, the method employed to automatically mark and eliminate the regions with low seed particles is explained.

#### 2.2.4.1 Vertical Plane Measurements

Vertical plane measurements were taken for the valley and hill configurations. The dimensions of the camera field of view were 10.6cm horizontal and 14cm vertical (318m×420m on the full scale). Considering the image resolution (1600×1200 pixels), size of the interrogation region (32×32 pixels) and window overlap (50%), the velocity vectors were located 1.4mm apart that corresponds to 4.2 meters resolution in full scale, which is quite exceptional. The seed distribution was acceptable in the regions near the surface. However, as the elevation increased, the seed distribution became more non-uniform. A major cause of the non-uniformity in the seed distribution was the seed

entrainment by the near-surface eddies. In the image sequence obtained in the vertical plane, approximately 50% of the images represented some regions where the seed particle density was very low and some regions where the seed particle density was almost zero. A PIV image in the vertical plane is shown in Figure 2.8(a). The image shows insufficient seed in the upper left and top portions. In PIV measurements typically less than 1% of the velocity vectors are false vectors which can be corrected using local mean or median test that is based on the neighboring vectors. However, if the number of false vectors is large and they occupy a larger region, such tests do not work. One approach to deal with this problem is to flag the regions of very low seed density and remove them from further analysis. If the region(s) with insufficient seed density are fixed in the entire dataset, locating their coordinates is a simple task and partial processing of the PIV images is available in most of the commercial PIV processing software. However, if the size and location of the regions with insufficient seeding changes with time and space, the identification (and consequently elimination) of these regions is not a simple task. One option is to manually detect these regions, which is time consuming and laborious as thousands of images are typically acquired during the experiments. Another option is to automatically detect the problem regions based on the PIV image characteristics.

In the PIV technique, when seed particles enter the laser light sheet, they start illuminating which results in higher gray-scale values in the image. In the regions with low or negligible seed density, the gray-scale values are low due to the illumination of fewer particles.

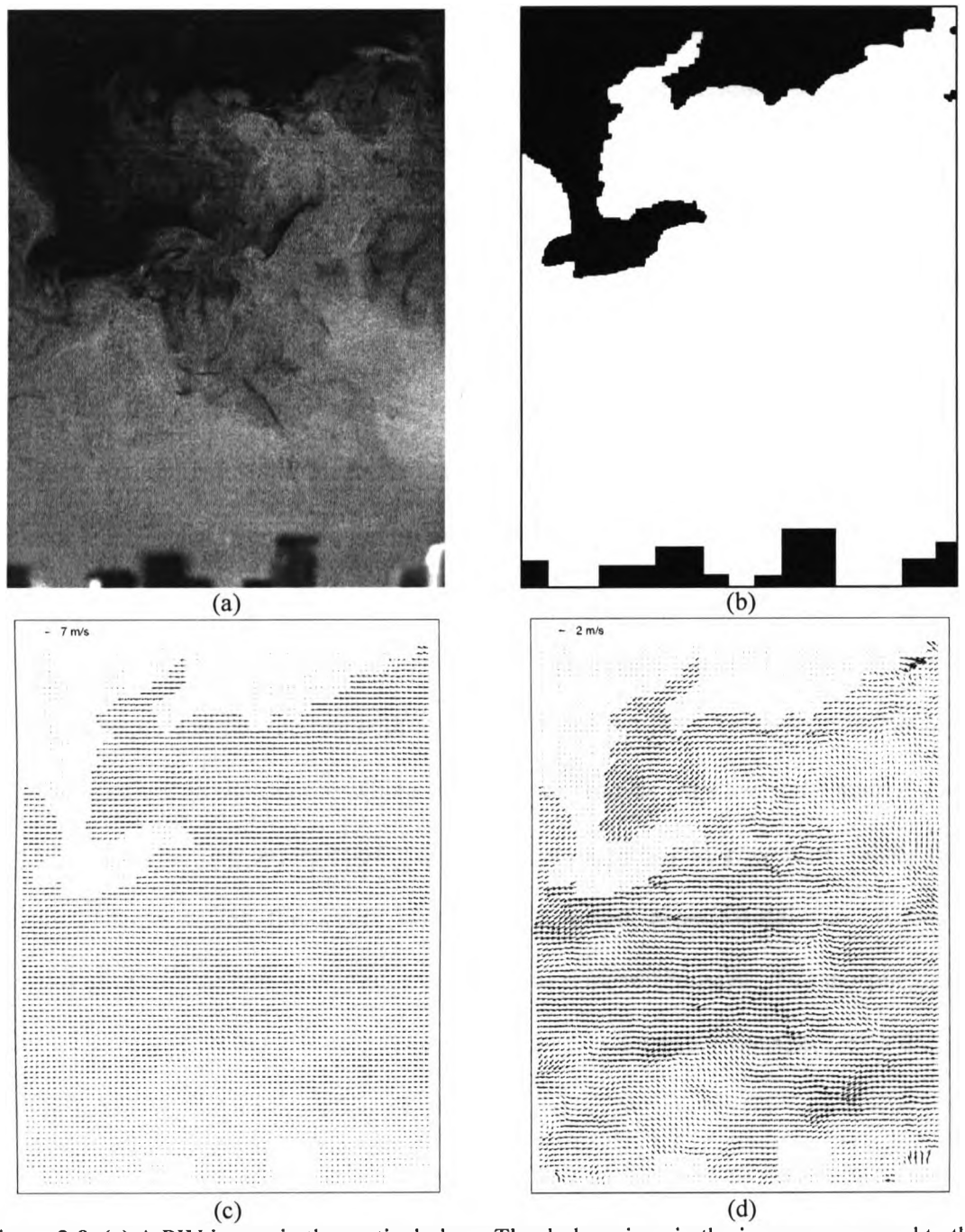


Figure 2.8: (a) A PIV image in the vertical plane. The dark regions in the image correspond to the areas where the seed density is very low. Some buildings (foam blocks) are also visible at the bottom of the image, obstructing the view of laser light sheet. (b) The segmented image obtained after applying the detection scheme to the presented PIV image. The black regions correspond to the areas with insufficient seed density. The buildings located at the bottom of the image are also marked and excluded. (c) The corrected instantaneous velocity field (d) The corresponding turbulent velocity field. The free-stream flow is from right to left.

Using this image characteristic, a novel method (Siddiqui et al. 2008) was employed to automatically detect the regions with low seed density and exclude them from further analysis. First, an image processing scheme was used to detect the insufficient seed density regions in the PIV images. To do so, the signal-to-noise ratio of the image was enhanced by re-scaling the gray-scale values of the image by adjusting the upper and lower gray-scale limits. The limits were set based on the analysis of the gray-scale distribution in a subset of images from the given dataset. The upper and lower limits remained the same for the given dataset. In the next step, the gray-scale image was converted into a binary image by applying a threshold such that gray-scale values higher than or equal to the threshold were assigned 1's, which correspond to the regions with sufficient seed density. The gray-scale values lower than the threshold were assigned 0's, which correspond to the regions with insufficient seed density. To set the threshold, the gray-scale values in the regions where the seed density was very low were analyzed in a subset of images. This information was used to set a threshold gray-scale value which remained constant for the entire dataset of a given experimental run. A set of morphological operations were performed next, to remove the noise. The morphological operations were performed in two sequences. The first sequence consisted of a dilation operation followed by an operation which closed the "holes" within the object, which was followed by an erosion operation. A square mask of 10×10 pixels was used in this sequence. The second sequence consists of erosion, dilation and closing holes operations with a square mask of 20×20 pixels. The binary image obtained after applying the low seed density detection scheme on the image in Figure 2.8(a) is shown in Figure 2.8(b). The comparison shows that the present scheme correctly identifies the low seed density

regions. The bottom of the PIV image in Figure 2.8(a) also shows some features, which are the foam blocks in the topographic model representing buildings that were located between the camera and the laser light sheet. These building also blocked the view of the seed particles in the corresponding regions. Since the position of these buildings was same in all PIV images, their locations were extracted from one image and applied to the entire image sequence.

In the next step, these binary images were used to remove the false vectors that are associated with the insufficient seed regions in the raw velocity fields. That is, in a given raw velocity field, all velocity vectors that were located in the regions occupied by 0's in the corresponding binary image were assigned as NaN (assigning a variable to NaN (not-a-number) flag is a convenient way to mark a variable for further consideration). As mentioned earlier, few spurious or false vectors are also found in the region with sufficient seed density (occupied by 1's). A scheme was used to identify the spurious velocity vectors in these regions and then correct them using a local median test (Siddiqui *et al.* 2001). Note that if a spurious vector is located in the neighborhood of 0's region, only the neighboring vectors in the 1's region are considered in the median test. It was found that less than 1% of the velocity vectors in the 1's region were spurious. The corrected instantaneous velocity field corresponds to the image pair in Figure 2.8(a), is shown in Figure 2.8(c). The plot shows the typical boundary layer trend in the velocity field. That is, the minimum velocities are observed near the ground and the velocity magnitude increased with the distance from the ground.

To obtain the mean velocity field for a given experimental run, the time series were extracted at each grid point from the sequence of corrected instantaneous velocity fields.

The mean velocity was obtained at each grid point by time-averaging. Note that in a given time series, all points associated with NaN were excluded from the mean velocity computation. The turbulent velocity fields were computed by subtracting the time-averaged mean velocity at each grid point, from the corresponding instantaneous velocity. Note that all the grid points associated with NaN in any instantaneous velocity field remained NaN in the corresponding turbulent velocity field. The turbulent kinetic energy (t.k.e.) was then calculated assuming that the third velocity component is equal to the average of the two measured velocity components:

$$k = \frac{3}{4}\left(u'^2 + v'^2\right), \; k = \frac{3}{4}\left(u'^2 + w'^2\right) \tag{2.1}$$

where, the first relation is used in horizontal planes and the second one is used for vertical planes.

The turbulent velocity field associated with the instantaneous velocity field in Figure 2.8(c) is shown in Figure 2.8(d).

As mentioned earlier, the regions of insufficient seed density were observed in about 50% of the image pairs for this set of measurements. Therefore, the remaining approx. 50% of image pairs have sufficient seed density throughout the image. An instantaneous velocity field from the same dataset for this latter case is shown in Figure 2.9(a). The corresponding turbulent velocity field is shown in Figure 2.9(b).

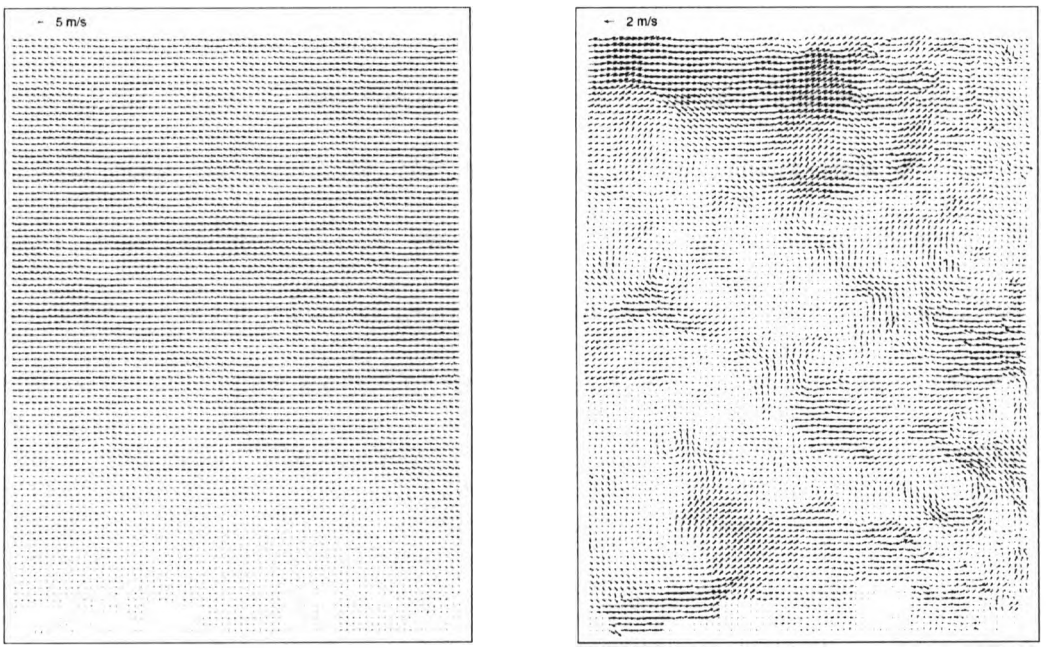


(a) (b)

Figure 2.9: (a) Instantaneous and (b) turbulent velocity fields from a PIV image pair that has sufficient seed density in the entire image pair. The free-stream flow is from right to left.

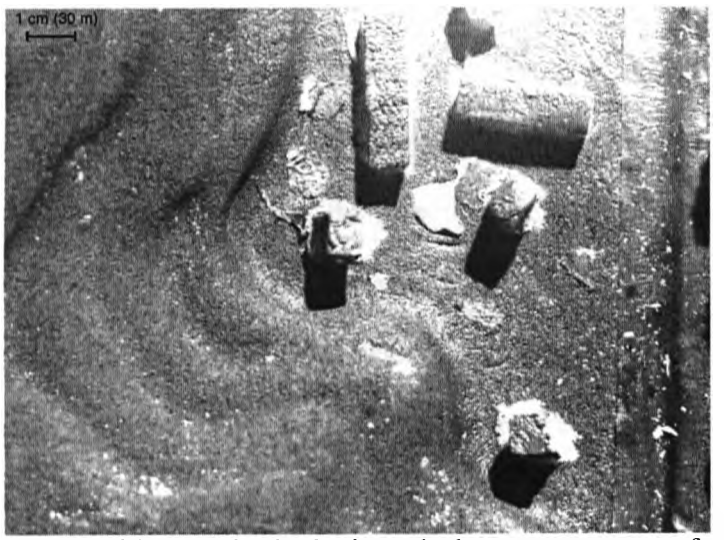


Figure 2.10: The region of interest in the horizontal plane measurements for the valley. The dimensions of the region of interest are 15cm×11.3cm. The length scale is also provided for the model scale and full-scale (in parenthesis). The free-stream flow is from top to bottom of the image.

#### 2.2.4.2 Horizontal Plane Measurements

Horizontal measurements were taken for the valley, hill and ridge configurations. For horizontal plane measurements, the dimensions of the camera field of view were 15cm×11.3cm (450m×338m on the full scale). The approximate location of the horizontal plane in the region of interest inside the valley is shown in Figure 2.10. The foothills are visible in the left portion of the image. Some model building blocks are also located near the base of the foothills inside the valley. For the given size of interrogation region and window overlap, the resolution of the obtained velocity vectors was 1.5mm (full scale resolution of 4.5m). Measurements in the horizontal planes were taken at different heights from 6.2cm to 11.6cm measured from the base of the model. Insufficient seed density regions were observed in relatively few image pairs for the measurements at 6.5cm height in the valley. However, with increasing height, both the number of images with the insufficient seed regions and the size of insufficient seed regions in a given image increased. At the two higher elevations, the insufficient seed regions were observed in almost all images; however, the false vector elimination method introduced in the former subsection was employed and the false vectors were eliminated. Attempts to conduct measurements at few higher elevations were made but the non-uniform seed density appeared to be a serious issue. That is, the size of the insufficient seed regions grew to one-quarter to half the size of the image. For instance, in all horizontal plane measurements at the valley the regions of insufficient seed density were mainly observed in the left portions of the image which is above the foothill (Figure 2.10).

An instantaneous velocity field and its corresponding turbulent velocity fields for valley configuration in the horizontal plane at a height of 8.4cm are shown in Figure 2.11(a) and

(b), respectively. Note that the false vectors in the top left region of the image have been automatically removed. Approximately 450 of 900 image pairs in the dataset were properly seeded in the entire region; therefore, the final computed mean and rms velocity vectors are valid for the entire extent of the PIV image.

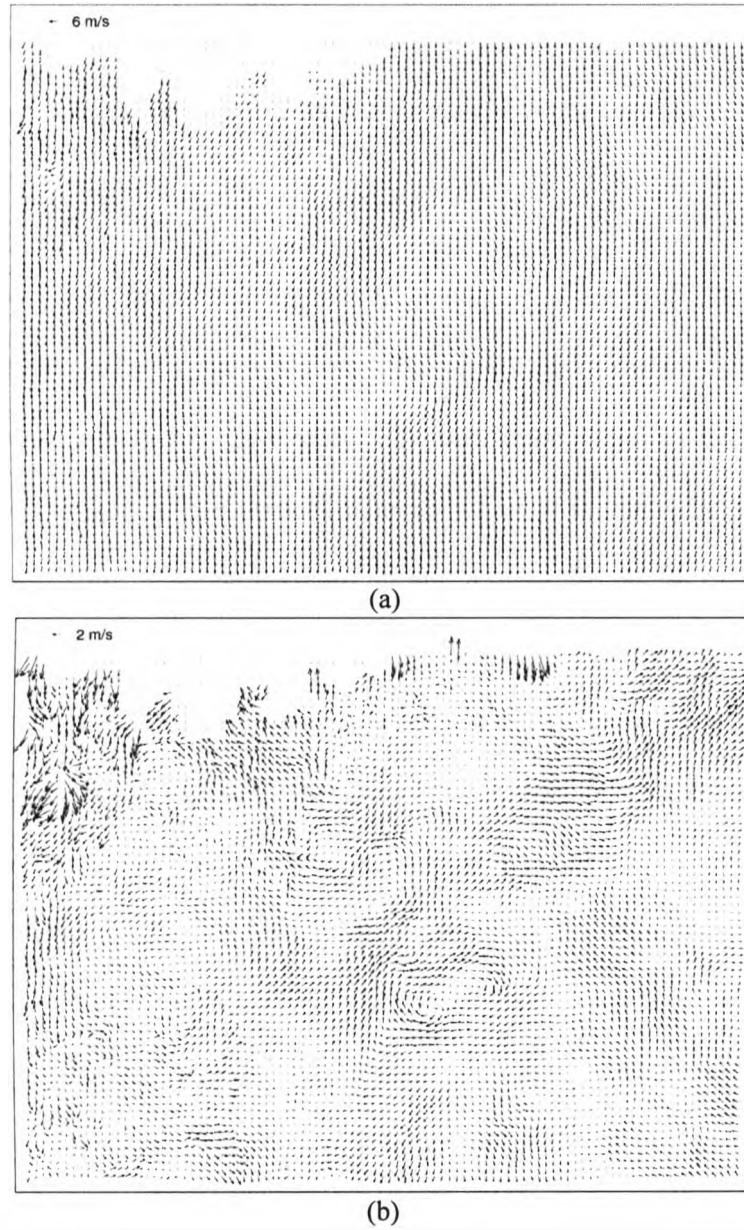


Figure 2.11: (a) An instantaneous velocity field and (b) corresponding turbulent velocity field in a horizontal plane at a height of 8.4cm for the valley. The free-stream flow is from top to bottom.

## 2.3 Results and Discussion

The results are presented in the order of flow complexity: the valley followed by the hill and the ridge flow. Both mean and fluctuating velocity fields are presented in horizontal and vertical (where available) planes. To better understand the spatial flow structure in relation to each of the topographic features, crosswind correlation analysis is also presented. Finally the PIV results are compared with hot-wire velocity profiles.

### *2.3.1 Valley Flow*

The valley flow configuration corresponds to an azimuthal angle of 320 degrees, Figure 2.12. This is expected to be the simplest wind flow case in the present study with no major separation-reattachment flow areas. PIV measurements were performed in three horizontal planes as well as one vertical plane as indicated in Figure 2.13. The elevation contours corresponding to the topography in and around the region of interest are also presented.

The mean velocity field in two horizontal planes at $z = 195\text{m}$ and $z = 312\text{m}$ are shown in Figure 2.14. It should be noted that the original resolution of the velocity vectors computed from the PIV images is 72×97 vectors which is reduced to 12×15 vectors in all vector plots in this section for better visualization of the flow field. The elevation contours are also superimposed in the plots for better illustration of the topographic profile underneath the measurement plane. This is a quasi-parallel, well behaved flow. The only influence of the topography is observed in the upper portion of the plot corresponding to a local region of topographic terrain. Here the vectors deviate slightly from the main wind direction. As expected this effect reduces with increasing height, see Figure 2.14(b).

Figure 2.12: Wind direction for valley configuration. The cross marks the approximate location of the region of interest (Satellite image is from Google Earth).

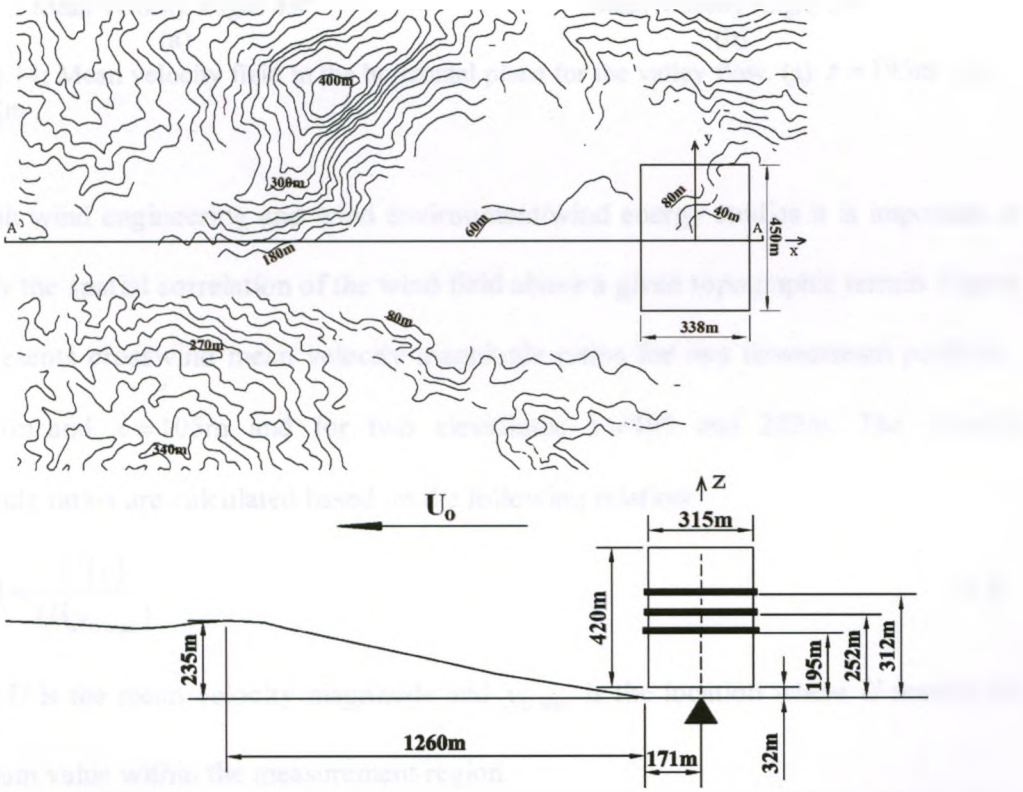


Figure 2.13: Topographic contours and side view of the valley configuration with horizontal and vertical measurement area locations, size and reference coordinates. The rectangles show the extent of the PIV measurements in horizontal and vertical planes. The thick solid lines in side view correspond to the horizontal measurement planes demonstrated as a rectangle in top view.

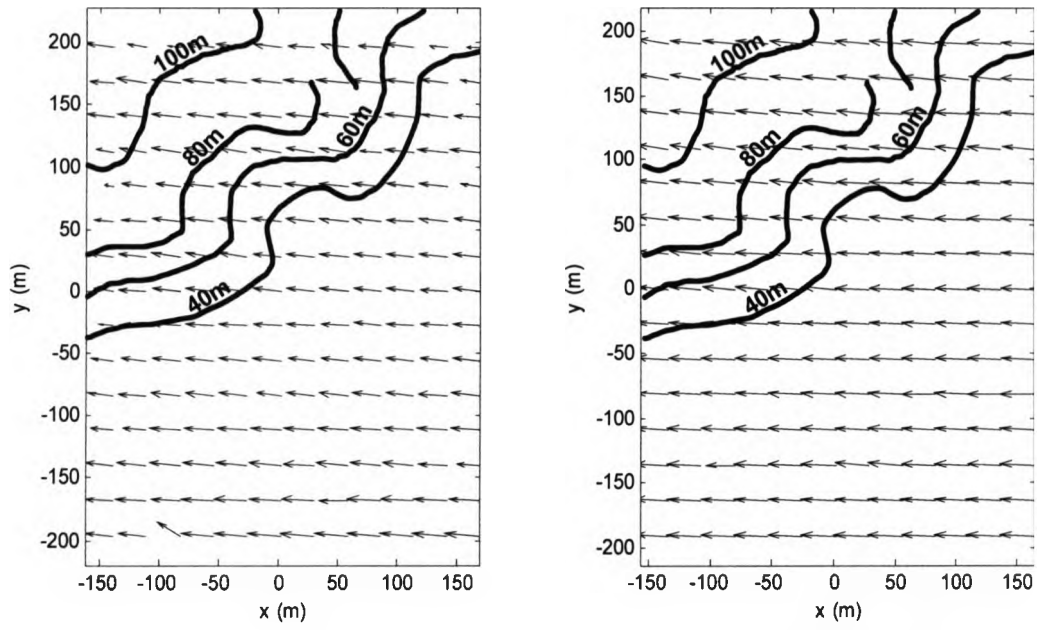


Mean Velocity Angle: 4.6° (a)

Mean Velocity Angle: 2.9° (b)

Figure 2.14: Mean velocity field in the horizontal plane for the valley flow. (a) $z = 195\text{m}$, (b) $z = 312\text{m}$.

For both wind engineering and wind environment/wind energy studies it is important to quantify the spatial correlation of the wind field above a given topographic terrain. Figure 2.15 presents crosswind mean velocity magnitude ratios for two downstream positions, $x = -44\text{m}$ and $x = 105\text{m}$ and for two elevations: $z = 195$ and 252m. The velocity magnitude ratios are calculated based on the following relation:

$$R_{UU}(y) = \frac{U(y)}{U(y_{U\max})} \tag{2.2}$$

where, $U$ is the mean velocity magnitude and $y_{U\max}$ is the location where $U$ reaches its maximum value within the measurement region.

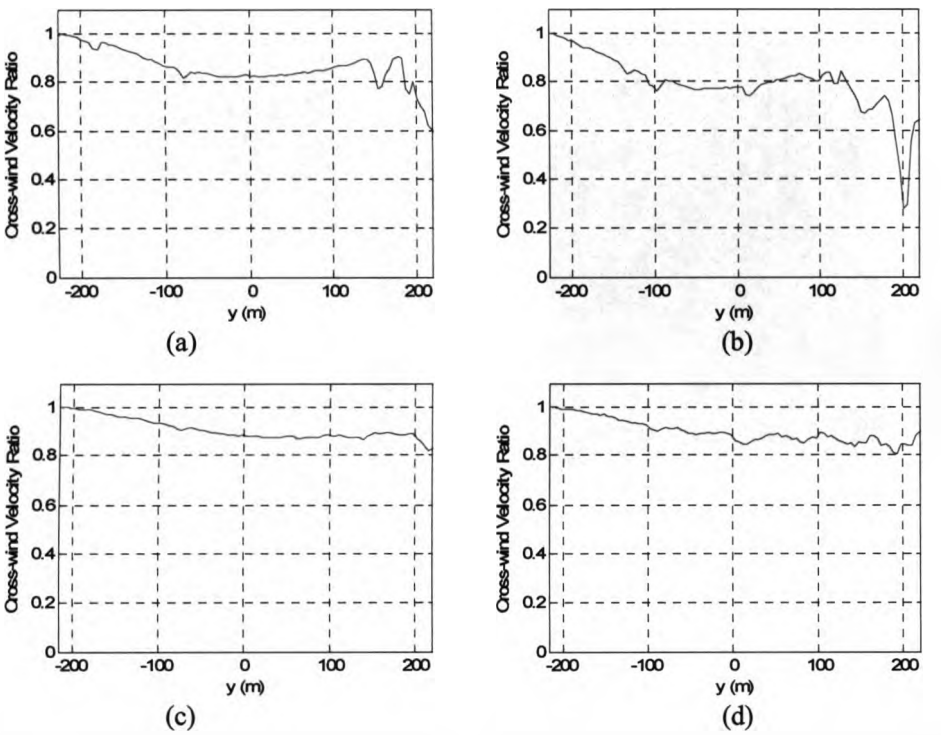


Figure 2.15: Crosswind mean velocity magnitude ratios for the valley flow at three heights and two downstream locations. (a) $z = 195\text{m}$, $x = -44\text{m}$, (b) $z = 195\text{m}$, $x = 105\text{m}$, (c) $z = 252\text{m}$, $x = -44\text{m}$, (d) $z = 252\text{m}$, $x = 105\text{m}$.

As expected, at higher levels above the surface, the mean velocity correlates well over a large spatial extent in the crosswind direction, see Figs. Figure 2.15(c) and (d). As we approach the surface, the velocity ratios decrease, see Figure 2.15(a) and (b). Note that the sudden drop in Figure 2.15(b) is attributed to the PIV errors at the edge of the frame rather than to a physical cause. The overall velocity ratios are relatively high for this case further confirming that the flow is well behaved. In fact the vertical plane PIV plots (not shown herein) indicate a classical, parallel, boundary layer behaviour in this region. Figure 2.15 also indicated that there is no clear trend in the velocity ratio variation with the downstream position for this case.

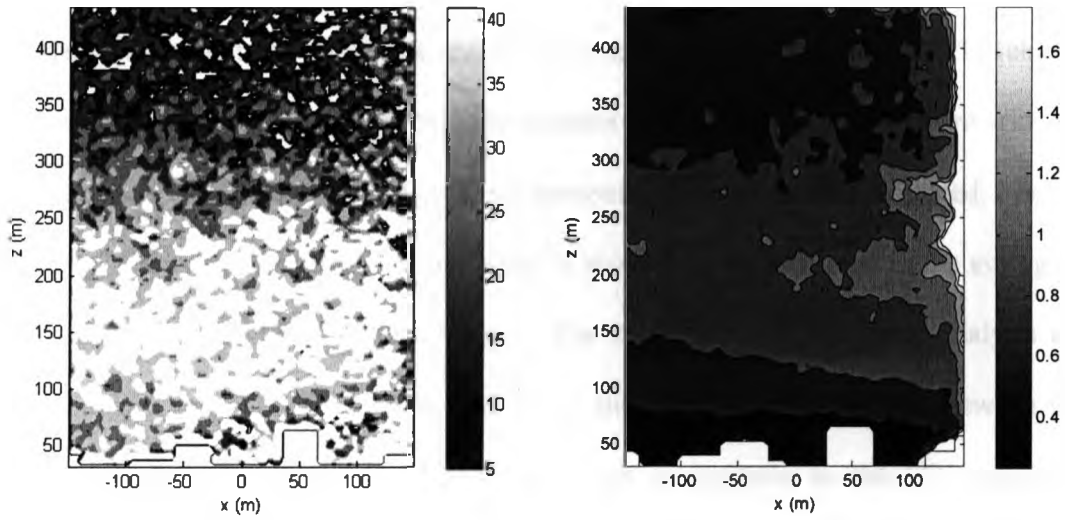


(a) (b)

Figure 2.16: Contour plots for the valley flow in a vertical plane at $y = 0$. (a) Mean vorticity contours [1/sec], (b) t.k.e. contours [$m^2/sec^2$]. Flow direction is from right to left.

The PIV measurements also provide an opportunity to analyze the flow structure in a vertical plane at the same location. Figure 2.16(a) and (b) present contour plots of mean vorticity and t.k.e., respectively in the vertical plane at $y = 0$. The wind direction is from right to left. The building blocks that appear in the lower portion of the plots lie between the measurement plane and the PIV camera at 212m lateral from the measurement plane. The building height is small compared to this distance and hence the building did not influence the flow in the vertical measurement plane. The vorticity plot shows high level of crosswind vorticity in the near-surface region with maximum values in the shear layer, between 150 m and 200 m. As expected, the t.k.e. plot shows maximum turbulence levels in the same region.

PIV and hot-wire mean velocity and turbulence intensity profiles are compared at the approximate location of (x,y)=(0,0). The hotwire data, sampled at 500 Hz, was available from a previous experiment at the same wind speed and at a specific horizontal location

within the same region as for the horizontal and vertical PIV measurements. As the PIV provides velocity data at very high resolution in space, there were several PIV velocity vectors in the vicinity of the approximate location of the hotwire. To compare with the hotwire data, PIV velocity vectors over this approximate location were averaged. Prior to averaging, a sensitivity analysis is conducted to investigate the influence of the averaging window size for the PIV velocity vectors. The details of the sensitivity analysis are presented in Table 2.1. The results show that the percentage difference between the hotwire and PIV datasets slightly decreased with an increase in the PIV averaging window size, however, the variations from a 2×2 window to a 9×9 window are less than 5%. A 3×3 averaging window (i.e. 9 velocity vectors) is selected for this case that correspond to a full-scale area of 196 $m^2$.

The mean and turbulent intensity profiles from hotwire (Ho and De Leebeeck (2004)) and PIV measurements are compared in Figure 2.17. Given the complexity of the topographic model, the fact that the three sets of measurements (hot-wires, horizontal PIV and vertical PIV) were taken at different times and the inherent errors in determining the exact same location for the three sets of independent measurements, the overall matching of the mean velocity profiles in Figure 2.17(a), is quite remarkable. The mean streamwise velocity computed from both vertical and horizontal PIV measurement planes are slightly larger compared to the hot-wire measurements, mostly in the outer-layer.

Table 2.1: Sensitivity analysis of the mean velocities relative to the size of the averaging area for the PIV velocity vectors. The percentage difference is calculated with respect to values measured with the hot-wire.

| Averaging area size (no. of points) | 81 | 36 | 9 | 4 |
|---|---|---|---|---|
| Averaging area size in full scale ($m^2$) | 1764 | 784 | 196 | 81 |
| Percentage difference | 7.38 | 7.52 | 7.66 | 7.75 |

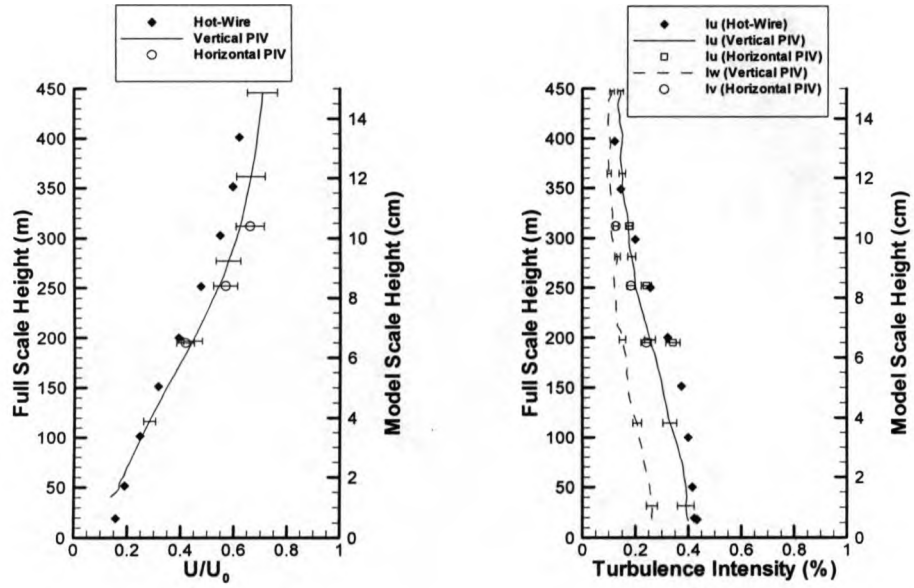


Figure 2.17: Comparison of profiles measured by PIV and hot-wires for the valley flow. (a) Mean velocity, (b) Turbulence intensity.

The comparison is less trivial for the turbulence intensity profiles. While hot-wires only record the velocity component perpendicular to the sensor, two velocity components are extracted from the PIV measurements for each plane: *Iu* and *Iv* are determined in the horizontal plane and *Iu* and *Iw* are determined in the vertical plane. In Figure 2.17(b), the continuous and dashed lines represent measurements from the vertical PIV plane (streamwise and vertical turbulence intensities, respectively), and the open symbols represent measurements from the horizontal PIV plane (streamwise and crosswind turbulence intensities). The plot shows excellent agreement between the horizontal PIV and hot-wires *Iu* measurements. The turbulence intensities from the vertical PIV measurements compare well in the upper layer and are lower compared to the ones from hot-wires below 250m. These differences however are within the measurement uncertainty range. As expected the other two turbulence intensity components, *Iv* and *Iw*, have lower values compared to the alongwind component.

Figure 2.18: Wind direction for hill configuration. The cross marks the approximate location of the region of interest (Satellite image is from Google Earth).

### *2.3.2 Hill Flow*

The hill flow location corresponds to an azimuthal angle of 40 degrees, Figure 2.18. The PIV measurements were performed in two horizontal planes as well as one vertical plane. The locations of the horizontal and vertical PIV measurement planes with respect to the hill and the elevation contours corresponding to the topography in and around the region of interest are depicted in Figure 2.19. The mean velocity field in two horizontal planes at $z = 249\text{m}$ and $z = 360\text{m}$ are shown in Figure 2.20(a) and (b), respectively. The plots show that the mean flow is well behaved as it approaches the hill. A slight deviation from the free stream direction is observed with an increase in the elevation of the topography. As expected, this deviation is more profound in the lower measurement plane at $z = 249\text{m}$.

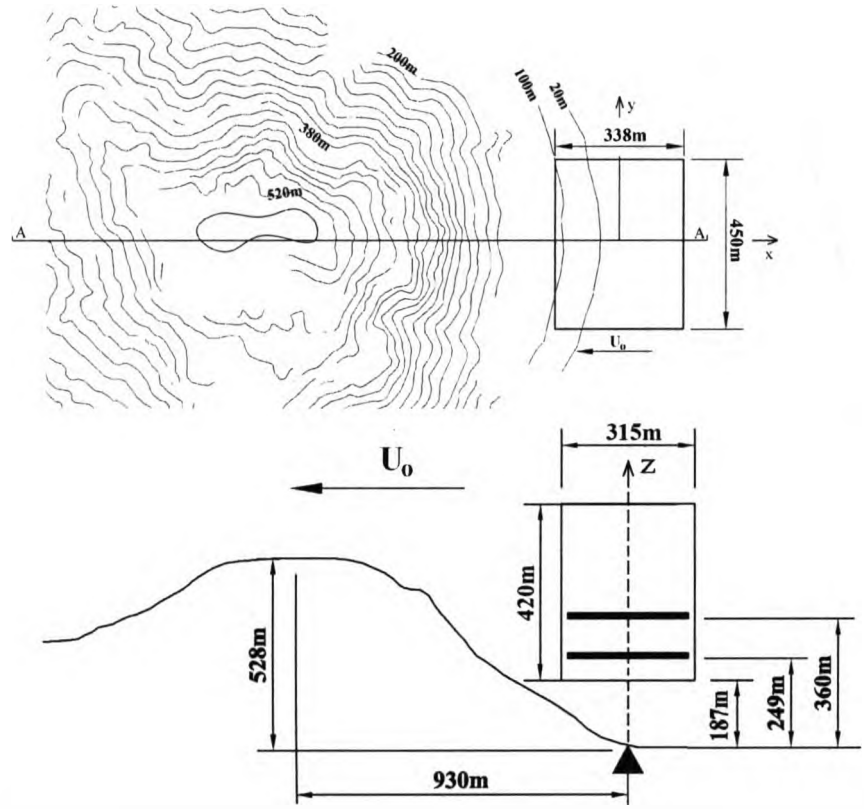


Figure 2.19: Topographic contours and side view of the hill configuration with horizontal and vertical measurement area locations, size and reference coordinates. The rectangles show the extent of the PIV measurements in horizontal and vertical planes. The thick solid lines in side view correspond to the horizontal measurement planes demonstrated as a rectangle in top view.

The crosswind mean velocity magnitude ratios for two alongwind positions, $x = 68\text{m}$ and $x = 139\text{m}$ and for two elevations: $z = 249$, and 360m are presented in Figure 2.21. Similar to the valley case the mean velocity magnitudes correlate better with increasing height, see Figure 2.15(c) and (d) and no clear trend is observed relative to downstream position. For both valley and hill cases, the wind direction is towards the topographic feature and therefore, the flow is less sensitive to the downstream location.

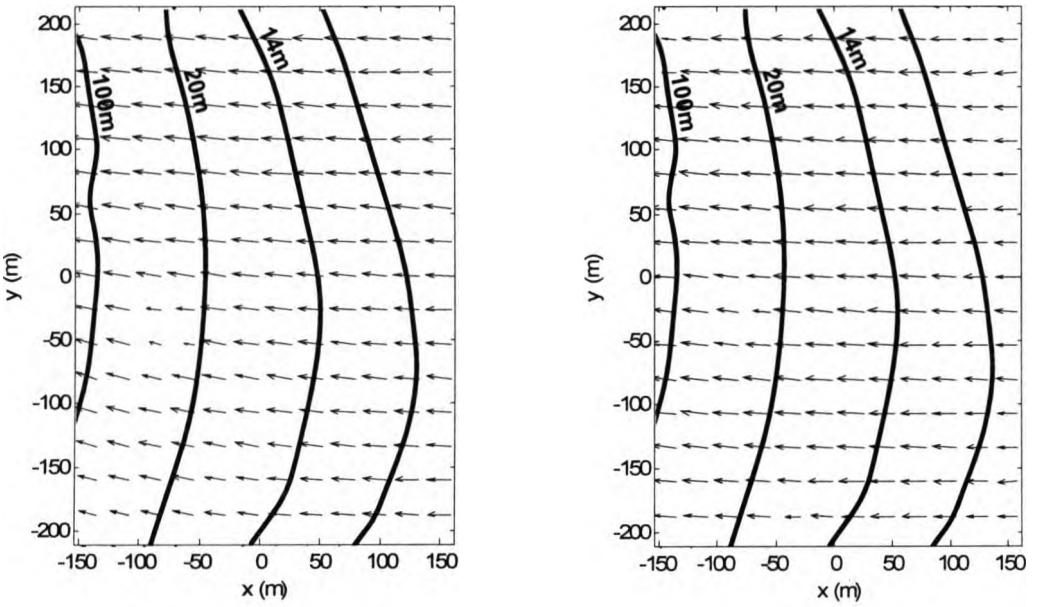


Mean Velocity Angle: 7.1°
(a)

Mean Velocity Angle: 3.1°
(b)

Figure 2.20: Mean velocity vectors in the horizontal plane for the hill flow. (a) $z = 249\text{m}$, (b) $z = 360\text{m}$.

The contour plots of mean vorticity and t.k.e. in the vertical plane are shown in Figure 2.22(a) and (b), respectively. A building block (approx. 275 meters high) close to the measurement plane is also visible in these figures. Both plots show that while the building is not exactly in the same plane ($\Delta y = 230\text{m}$) it affects the flow. The vorticity plot shows strong vortical structures which are induced by this building and other buildings close to the measurement plane. The t.k.e plot also shows higher level of turbulence in the vicinity of the building. These plots also indicate that the influence of the building on the overall flow structure is mainly restricted within the building height.

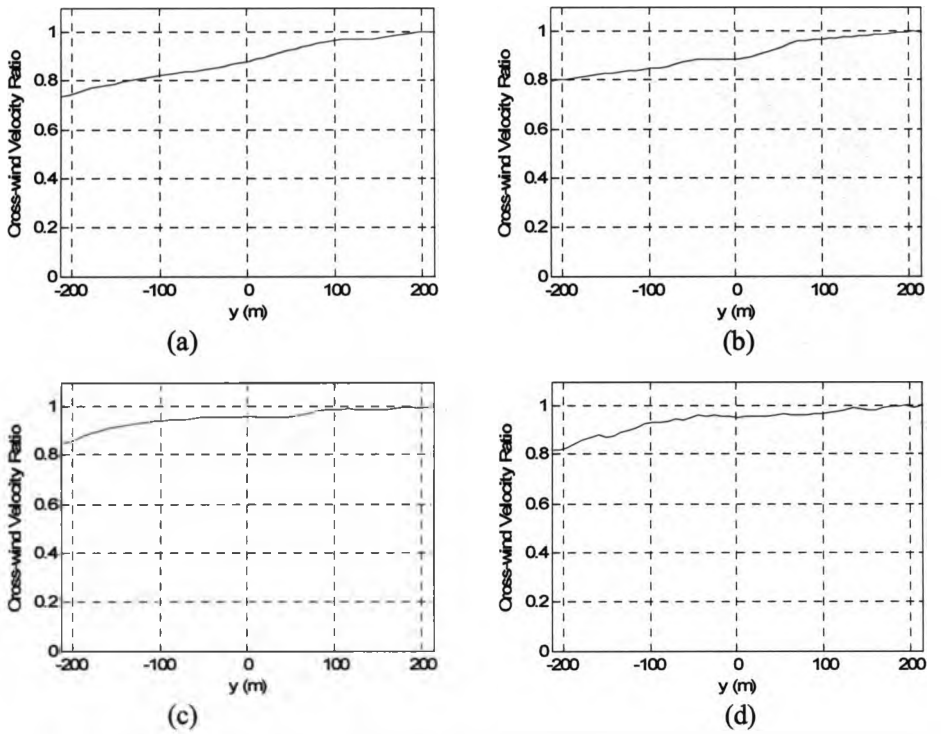


Figure 2.21: Crosswind mean velocity magnitude ratios for the hill flow at two heights and two downstream locations. (a) $z = 249\text{m}$, $x = 68\text{m}$ , (b) $z = 249\text{m}$, $x = 139\text{m}$ , (c) $z = 360\text{m}$, $x = 68\text{m}$, (d) $z = 360\text{m}$, $x = 139\text{m}$.

PIV and hot-wire (Farquhar and Ho (2004)) mean velocity and turbulence intensity profiles at the approximate location (x,y)=(0,0) are compared in Figure 2.23. Here the PIV data was averaged over a 2×2 matrix of 4 velocity vectors that corresponds to a full-scale area of 81 $m^2$. The data from all three sets of measurements (hot-wires, horizontal PIV and vertical PIV) shows very good agreement for both mean and turbulent intensities.

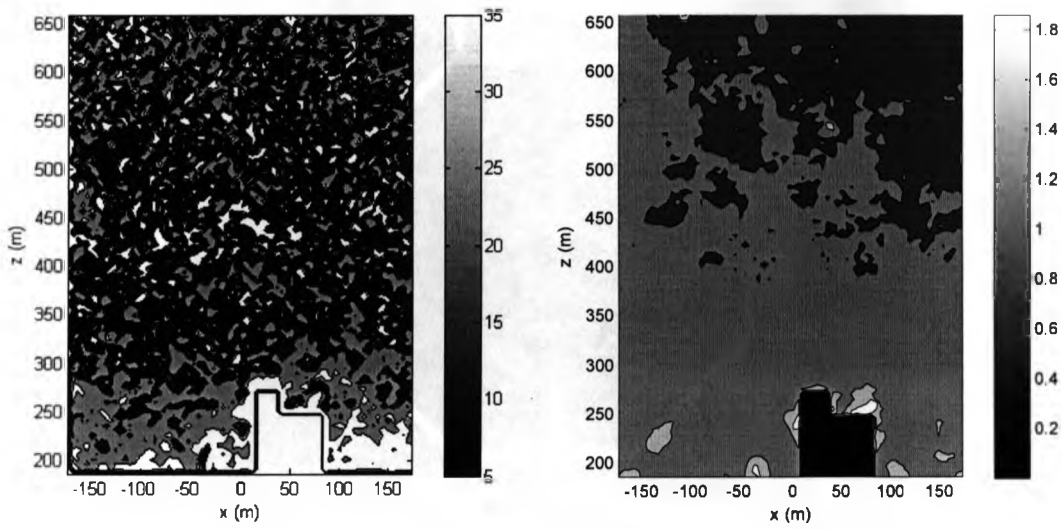


(a) (b)

Figure 2.22: Contour plots for the hill flow in a vertical plane at $y = 0$. (a) Mean vorticity contours [1/sec], (b) t.k.e. contours [$m^2/sec^2$]. Flow direction is from right to left.

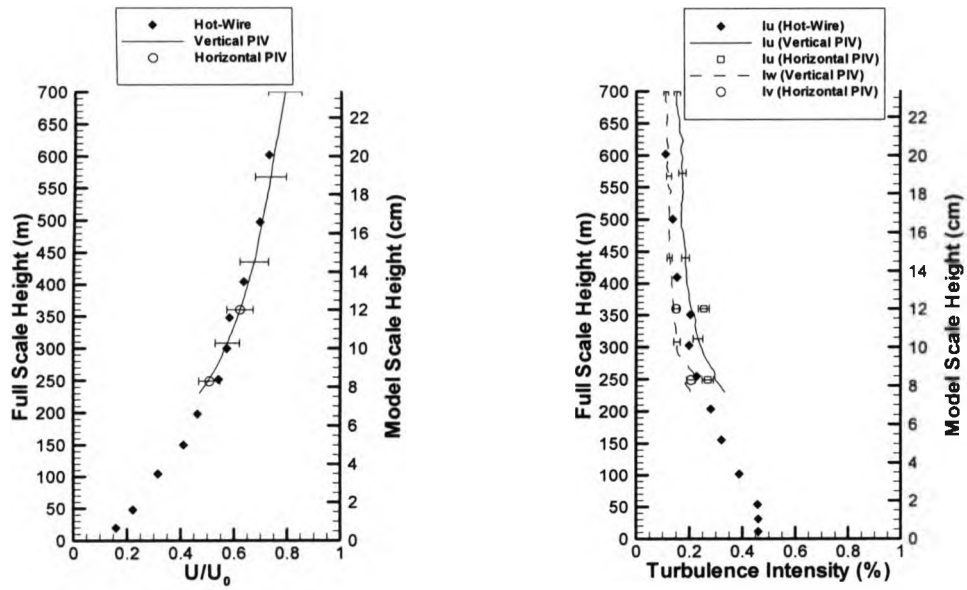


(a) (b)

Figure 2.23: Comparison of profiles measured by PIV and hot-wires for the hill flow. (a) Mean velocity, (b) Turbulence intensity.

Figure 2.24: Wind direction for ridge configuration. The cross marks the approximate location of the region of interest (Satellite image is from Google Earth).

### *2.3.3 Ridge Flow*

The ridge flow location corresponds to an azimuthal angle of 170 degrees, Figure 2.24. The PIV measurements were performed in four horizontal planes. No vertical plane measurements were performed for this case. The locations of the horizontal PIV measurement planes with respect to the ridge and the elevation contours corresponding to the topography in and around the region of interest are depicted in Figure 2.25.

As opposed to the two previous cases the ridge flow is expected to produce a complex recirculation zone in the wake of the ridge. Figure 2.26 presents the instantaneous and mean velocity vectors in a horizontal plane at $z$ = 200 m. Note the striking difference between these two plots. The instantaneous flow field for the ridge case, Figure 2.26(a), varies significantly in each frame; this implies that the ridge flow is rather complex and non-stationary. However, when averaged, the mean flow at 200 m, Figure 2.26(b), is well

structured even if not aligned with the free stream wind direction (left to right in this plot).

Figure 2.27 shows again instantaneous and mean velocity vector plots in a horizontal plane at z=255 m. While at this higher elevation, the mean velocity is aligned with the free stream velocity (Figure 2.27(b)), the instantaneous flow field is significantly influenced by the local topography, see Figure 2.27(a).

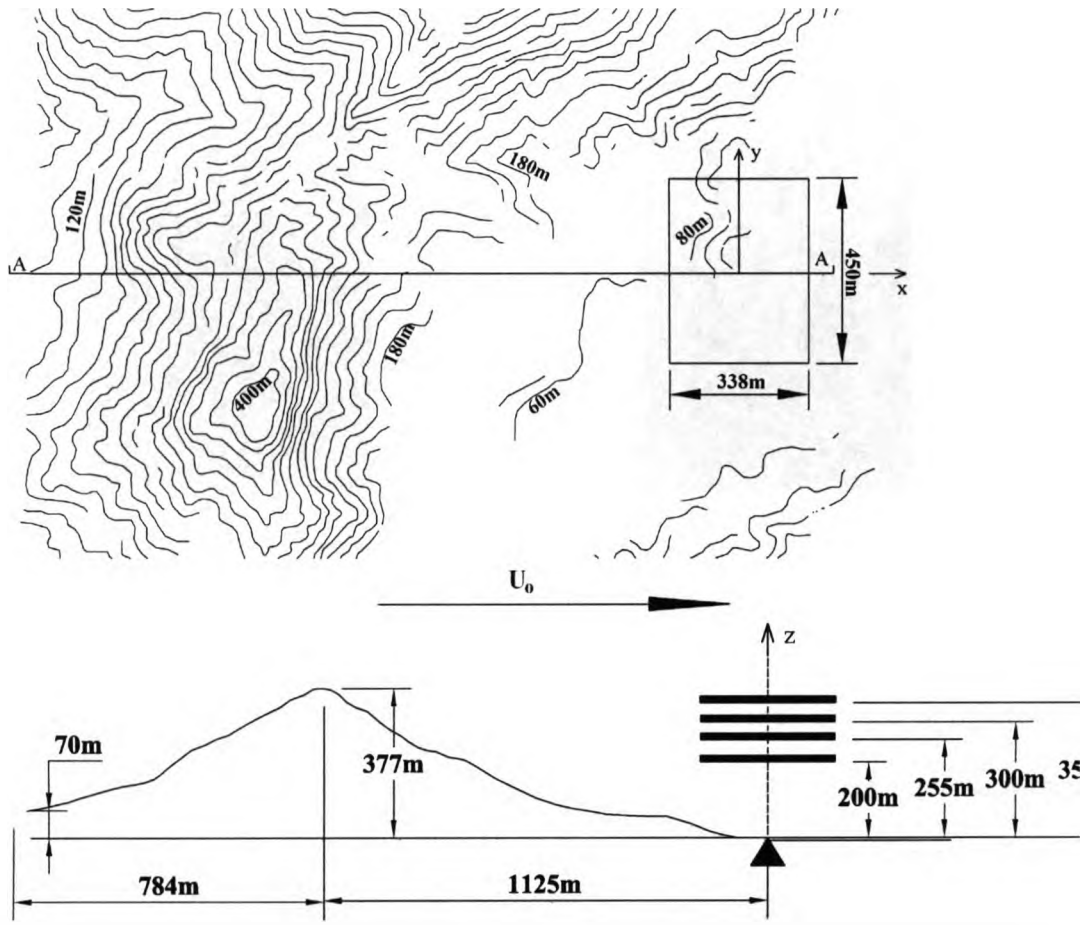


Figure 2.25: Topographic contours and side view of the ridge configuration with horizontal measurement area locations, size and reference coordinates. The rectangle shows the extent of the PIV measurement in the horizontal plane. The thick solid lines in side view correspond to the horizontal measurement planes demonstrated as a rectangle in top view.

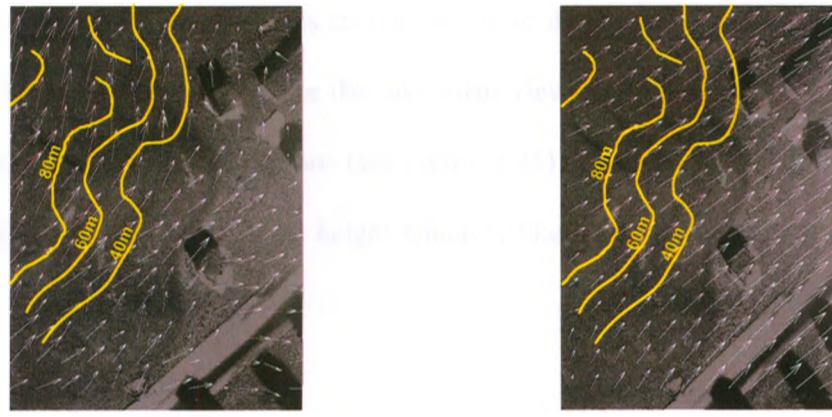


(a) (b)

Figure 2.26: Velocity vectors for the ridge flow in a horizontal plane at $z = 200\text{m}$.
(a) Instantaneous velocity field, (b) Mean velocity field. The velocity vectors are superimposed on the topography image. Flow direction is from left to right.

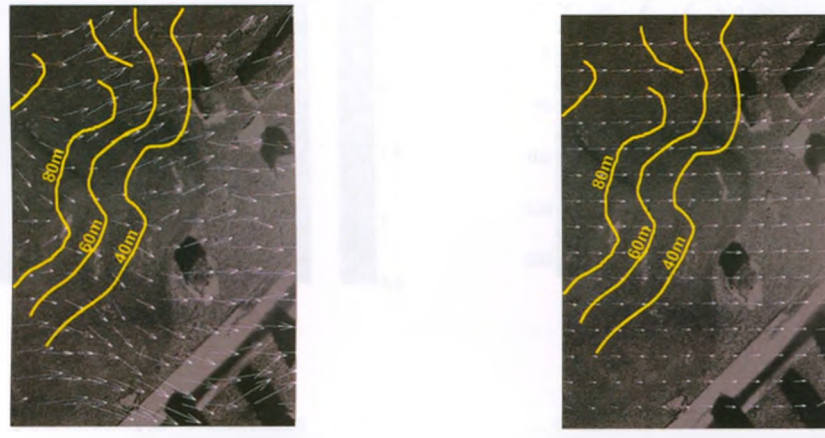


(a) (b)

Figure 2.27: Velocity vectors for the ridge flow in a horizontal plane at $z = 255\text{m}$.
(a) Instantaneous velocity field, (b) Mean velocity field. The velocity vectors are superimposed on the topography image.

The complexity of the ridge Flow is also illustrated by the contours of t.k.e. at different heights in Figure 2.28(a) to (d). The plots show a large variation of t.k.e. patterns with height. Figure 2.28(a) and (b) show maximum t.k.e. levels in the upper left region. This indicates that closer to the surface, the t.k.e. is mainly influenced by the local topographic features. In contrast, Figure 2.28 (c) and (d) show maximum t.k.e. levels in the mid-lower

region. This indicates that at levels corresponding to the ridge height the main impact on the t.k.e. is due to the ridge. Note that in a plan view, the ridge is located towards the lower part of the measurement plane (see Figure 2.25). These four plots also indicate that the maximum t.k.e increases with height which is likely due to the increased production of t.k.e in the ridge shear layer.

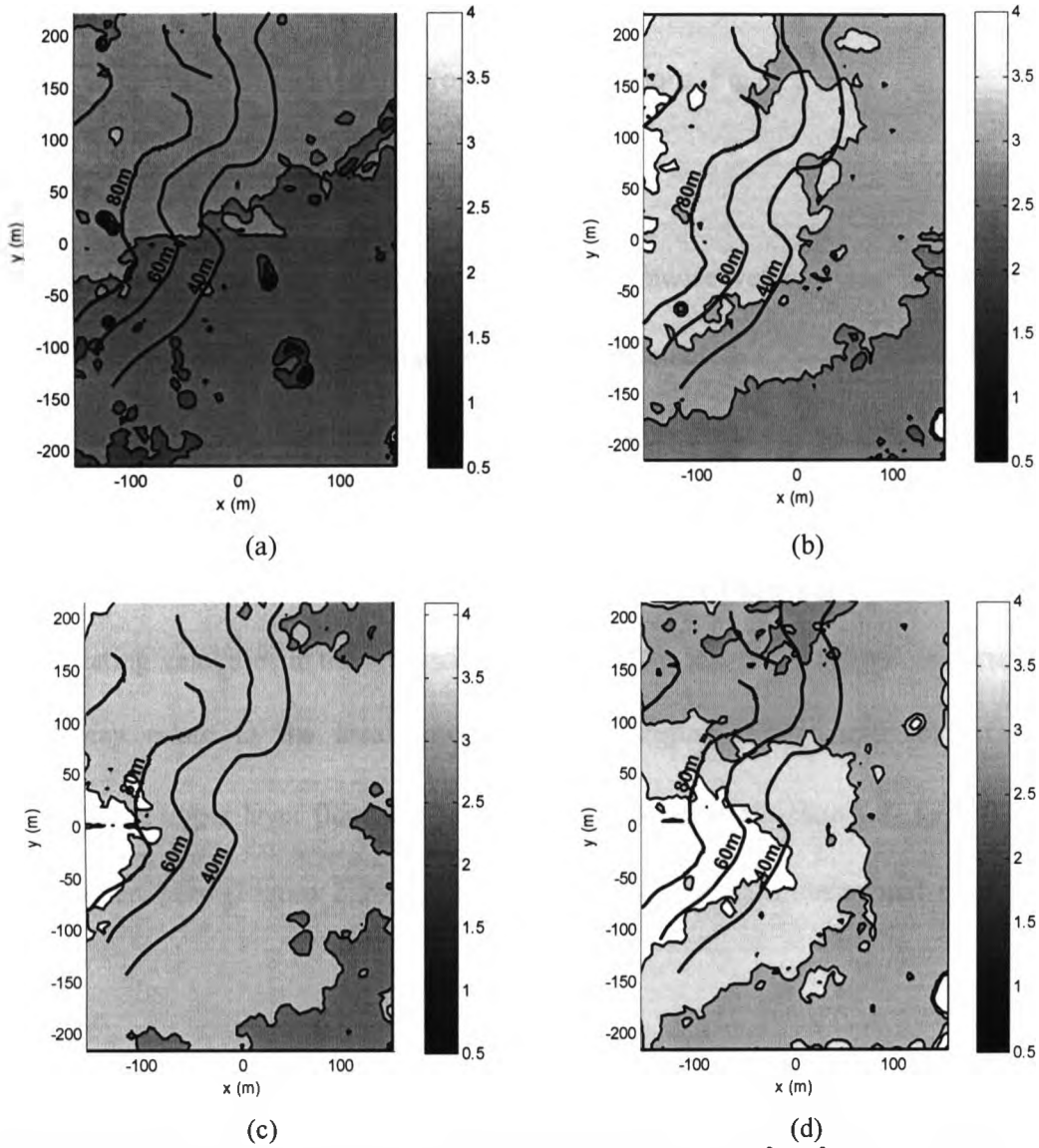


Figure 2.28: t.k.e contours for the ridge flow in horizontal planes [$m^2/sec^2$]. (a) $z = 200m$, (b) $z = 255m$, (c) $z = 300m$, (d) $z = 350m$. Flow direction is from left to right.

The crosswind mean velocity magnitude ratios for two alongwind positions, $x = -84$m and $x = 98$m and for two elevations: $z = 200$ and 255m are presented in Figure 2.29. In contrast to the two previous cases, the velocity ratios become weaker with increasing height. For the lowest height the largest ratios are observed at the location closest to the local topography, see Figure 2.29(a) and (b). Overall velocity ratios are smaller at higher levels and closer to the ridge.

For this case we also calculated the crosswind correlations, Figure 2.30:

$$R_{uu}(y) = \frac{< u(y_{ref}, t)\, u(y_{ref} + y, t) >}{< (u(y_{ref}))^2 >} \tag{2.3}$$

where, $u$ is the fluctuating component of the streamwise velocity and $y_{ref} = 0$ as the reference point at which the spatial correlations are calculated.

As opposed to the mean velocity ratios, $R_{uu}(y)$ decays faster in the ground proximity: $R_{uu}(y = -100)$ is 0.4 at $z = 200$m, Figure 2.30(a) and 0.45 at $z = 255$m, Figure 2.30(c). This indicates that in the shear layer the mean velocities are better correlated compared to the fluctuating velocities in the crosswind direction. This loss in the crosswind correlation $R_{uu}(y)$ may relate to the local topography, see Figure 2.28(a) and (b) for t.k.e.. Meantime, the upper layer fluctuating velocity field is better correlated, $R_{uu}(y) = 0.6$ was found for z=350m (Figure 2.30(f)), indicating the quasi two-dimensional ridge shear layer.

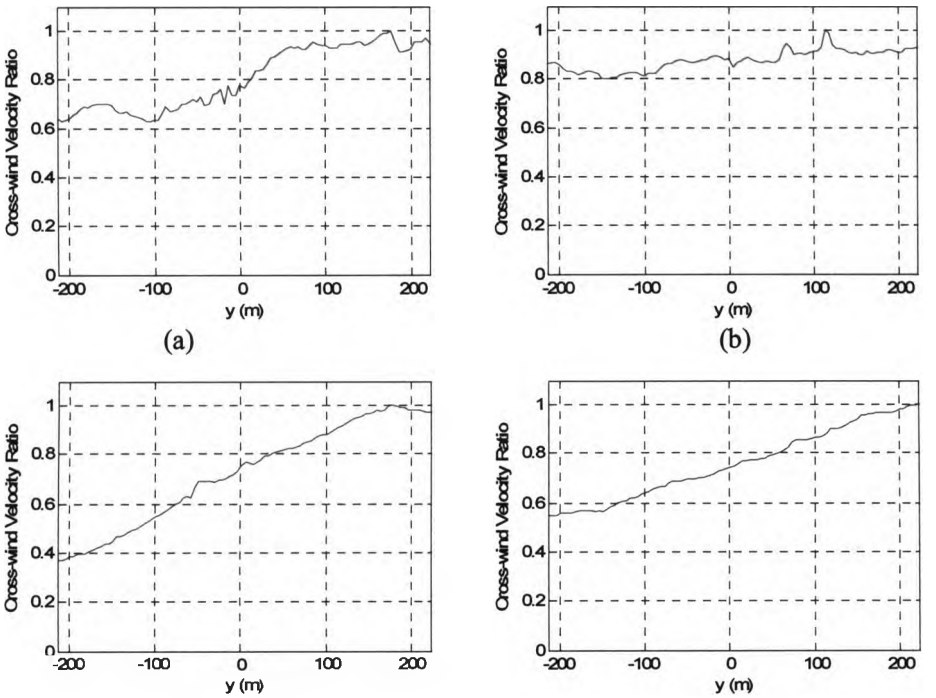


Figure 2.29: Crosswind mean velocity magnitude ratios for the ridge flow at three heights and two downstream locations. (a) $z = 200\text{m}$, $x = -84\text{m}$, (b) $z = 200\text{m}$, $x = 98\text{m}$, (c) $z = 255\text{m}$, $x = -84\text{m}$, (d) $z = 255\text{m}$, $x = 98\text{m}$.

PIV and hot-wire mean (Ho and De Leebeeck (2004)) velocity and turbulence intensity profiles for the ridge flow case are compared in Figure 2.31. Overall, the mean velocity data shows good agreement between the two techniques. Closer to the surface, the hot-wires tend to show larger magnitudes. This might be attributed to the fact that the flow in this region is very dynamic (i.e. the instantaneous and turbulent flow structures change rapidly with time), as evident in Figure 2.26(a).

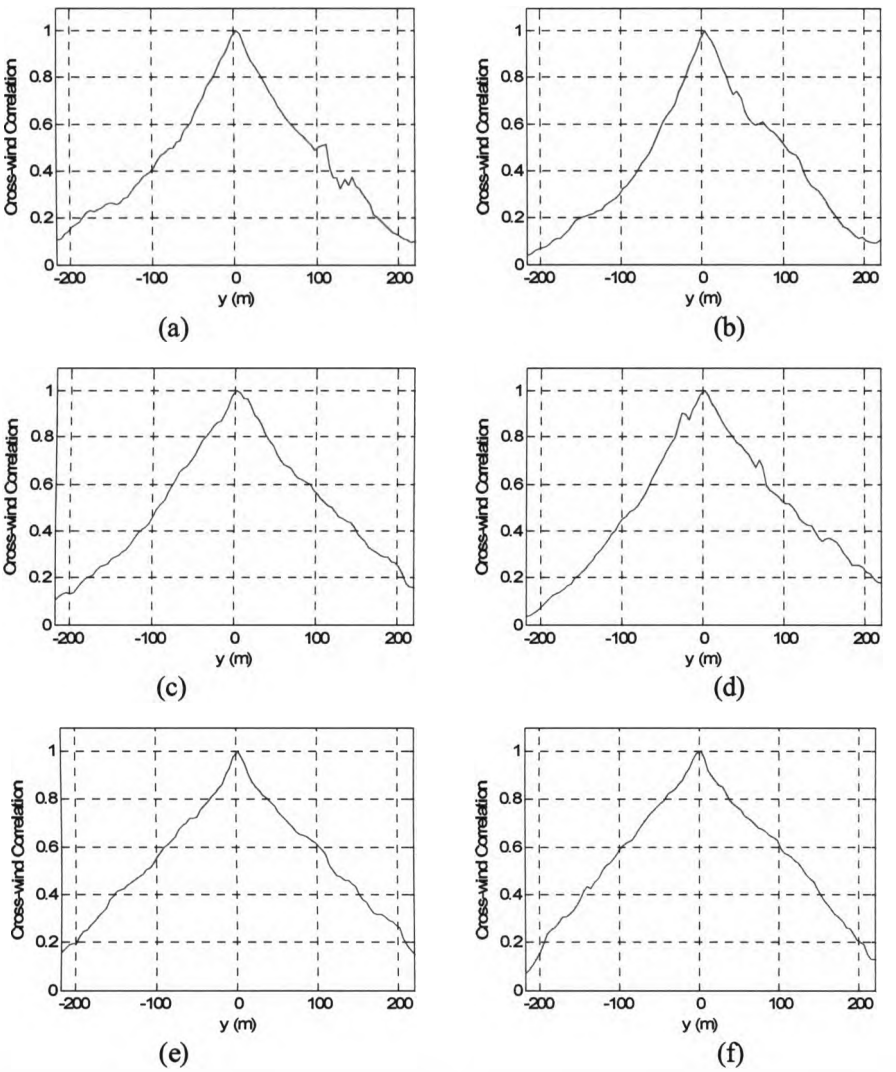


Figure 2.30: Crosswind correlations of the mean velocity magnitudes for the ridge flow at three heights and two downstream locations. (a) $z$ = 200m, $x$ = -84m, (b) $z$ = 200m, $x$ = 98m, (c) $z$ = 255m, $x$ = -84m, (d) ) $z$ = 255m, $x$ = 98m, (e) $z$ = 350m, $x$ = -84m, (f) $z$ = 350m, $x$ = 98m.

Figure 2.31(b) presents the turbulence intensity profiles from hot-wires and PIV measurements. While for levels above 300 meters the matching is again excellent, for the lower levels the PIV based turbulence intensities are larger compared to the ones obtained from hot-wires. A flow recirculation region is expected at these levels in the ridge wake. As hot-wires are insensitive to reverse flow, it is difficult to assess their measurement accuracy in this area mostly when turbulence intensities are well over 20%

(Kawall et al., 1983). Moreover, in this region the hot-wires showed higher mean velocities (Figure 2.31a), which would translate into lower calculated turbulence intensities. However, for this particular case these differences may also be related to PIV measurements due to large velocity gradients and flow seeding in the wake region. The seeding particles have the tendency to follow the local streak-lines and therefore less seeding protrudes in the ridge wake region. Large velocity gradients increase uncertainty in the PIV measurements. The other main difference between the two measurement systems relate to the sampling frequency, with the PIV sampling at lower frequency (15 Hz in this case) but over an increased time interval compared to the hot-wires. One of the limitations of the conventional PIV system is its lower time resolution which may be insufficient to resolve some important time scales in wind engineering applications such as structural responses. However, with the availability of high-speed time-resolved PIV system, this deficiency can be overcome.

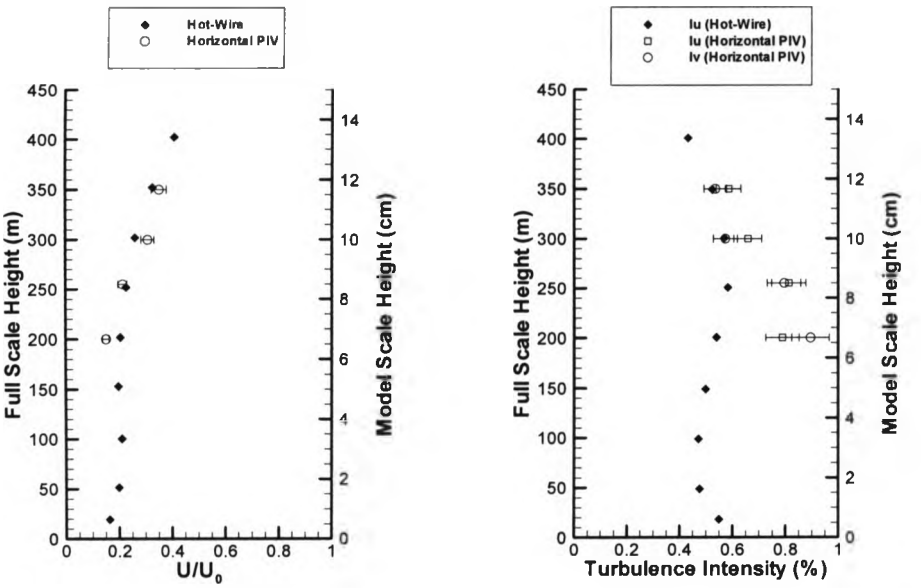


(a) (b)

Figure 2.31: Comparison of profiles measured by PIV and hot-wires for the ridge flow. (a) Mean velocity, (b) Turbulence intensity.

## 2.4 Conclusions

Particle Image Velocimetry (PIV) technique is for the first time applied for wind velocity mapping on a scaled model of complex topographic terrain. This non-intrusive technique simultaneously measures thousands of velocity vectors in a plane with high spatial resolution. However, due to its low sampling frequency, the PIV technique can resolve spatial scales of turbulence over a relatively wide range but can resolve only a small range of time scales. That is, the PIV technique can resolve turbulent scale up to very high wavenumbers but the time resolution is restricted to very low frequencies.

Carefully conducted PIV measurements using a large number of samples provide both mean and turbulent characteristics of the wind flow over extended areas. Three topographic configurations were investigated: a ridge, a valley and a hill. The results showed that while the valley and hill wind flows are relatively well behaved, the ridge flow is very dynamic. The t.k.e mapping for the ridge flow revealed that at lower heights, the flow is influenced by local topography while the dominant topographic feature (ridge) strongly influences the t.k.e at higher levels.

Crosswind mean velocity ratios showed that for the valley and hill cases the mean flow is well correlated over large spatial extends. For the ridge the crosswind mean velocity ratios and correlations were strongly influenced by the relative position from the local and major topographies.

The mean velocity profiles obtained by PIV were compared with hot-wire profiles previously measured at the same locations. The overall results show very good matching between the two techniques as well as between horizontal and vertical plane PIV measurements. The comparison of turbulence intensity profiles showed overall good

agreement between the two techniques for flow regions with no recirculation regions while discrepancies were found for the ridge wake region. These discrepancies may be attributed to the complexity of the flow in this region and the limitations of both techniques.

# 3 Simulations

## 3.1 Introduction

Developing a new cost effective and time efficient methodology to predict the wind patterns and obtain wind maps over any topographic terrain is absolutely needed for wind turbine/farm siting. Ideally one should be capable of producing wind maps over any type of terrain from the existing GIS data of the site and wind records. As introduced in the previous chapter, one method is performing PIV measurements over a physical scaled model of the topography. This is the best approach when dealing with complex topography and when the wind conditions at the site are known within the last 500 meters in altitude. However, sometime this is prohibitive and only large, mesoscale results are available on a grid size of the order of kilometers (both horizontally and vertically). In these cases CFD modeling seems to be the best alternate solution to provide microscale wind modeling. However, there are still many unanswered questions in selecting the best turbulence model, determining the solution domain size and the procedure to setup the upstream flow conditions.

In this chapter, two generic benchmark cases have been selected to study the effects of employing different turbulence models and the solution domain size: the two-dimensional NASA Hump and the three-dimensional Hill. Thereafter, CFD simulations for three different configurations of wind flow in southeast Hong Kong are presented. The selected areas for this ultimate case are the same regions introduced in the previous chapter.

## 3.2 Two-Dimensional Simulation – NASA Hump

In this section, the NASA hump model is introduced as a representation of a two-dimensional topographic feature that involves regions of impingement, boundary layer, separation and reattachment. Different numerical modeling schemes are evaluated to obtain the most suitable turbulence model for simulating the flow over the hump model as a typical topographic feature.

The NASA hump is a two-dimensional model that was originally designed with injection/suction holes for flow separation control studies (Figure 3.1(a) shows schematic of the experimental model of the hump). The hump is the upper surface of a 20% thick variant of the Glauert-Glas II airfoil (Seifert and Pack (2002)). The chord length of the model (C) is 42cm and the highest point on the hump (h) is 5.4cm. Figure 3.1(b) shows the hump profile and the reference coordinate system.

Several experiments were carried out by researchers to investigate the flow properties over the hump model (with and without flow control). Results such as surface pressure, skin friction and velocity profiles were produced as benchmark which are used as reference in this section.

### *3.2.1 Numerical Setup*

The flow conditions for the NASA hump experiment are listed in Table 3.1. The flow Reynolds number based on the hump chord length ($Re_C$) is $9.36\times10^5$. The velocity profile at 2.14C (0.90m) upstream of the hump leading edge is available from the previous measurements and is used in this study to verify the upstream length generating the proper boundary layer profile reaching the hump model.

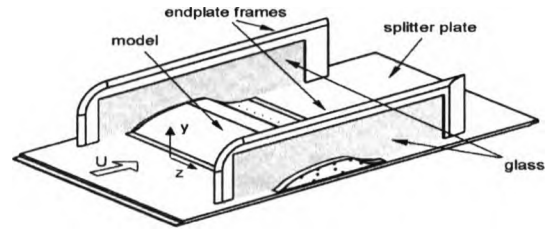


(a)

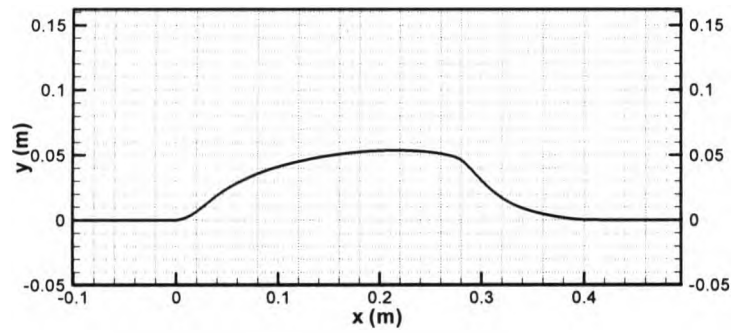


(b)

Figure 3.1: NASA hump model. (a) Schematic of the hump (from Greenblat et al. (2006)), (b) Hump prfoile.

Table 3.1: Flow conditions in NASA hump experiment.

| | |
|---|---|
| Inlet Mach number | 0.1 |
| Inlet velocity | 34.6m/s |
| Ambient pressure | 101325Pa |
| Ambient Temperature | 298°K |

#### 3.2.1.1 Solution Domain

The hump model was simulated in a rectangular domain with the hump model on the bottom wall of it (Figure 3.2). The height of the domain is 7.07h (0.3818m) which is adopted from the height of wind tunnel test section where the experiments were carried out. The outlet of the domain is 4C (1.68m) downstream of the trailing edge of the hump. The inlet boundary is located 6.39$C$ (2.68m) upstream of the leading edge. An upstream distance of 6.39C is required to develop a boundary layer at $x/C = -2.14$ (note that

leading edge of the hump is at $x/C = 0$) which is similar to boundary layer measured at this location in the wind tunnel (Sally and Viken (2003)).

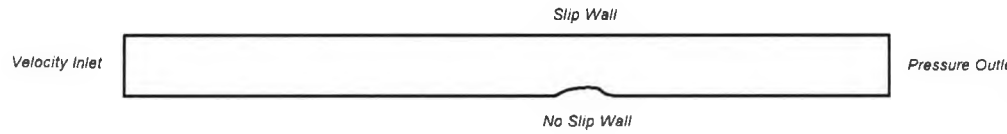


Figure 3.2: Solution domain and boundary conditions for NASA hump test case.

#### 3.2.1.2 Boundary Conditions

The boundary condition for bottom wall of the domain was considered as a no-slip wall without roughness. The top wall was specified as zero-shear stress (or slip wall) to prevent boundary layer formation. The outlet boundary is a pressure outlet with pressure drop of 53.70Pa (The pressure drop was calculated by Sally and Viken (2003)). Outflow boundary condition is another option for this problem; however, that would require the downstream length to be extended to accommodate for the fully developed flow assumption at the outlet boundary in this case. Figure 3.2 illustrates the boundary conditions on the solution domain. The inlet boundary is a velocity inlet with uniform velocity distribution of 34.6m/s and turbulence intensity of 0.1%.

#### 3.2.1.3 Grid

A multi-block structured grid was generated in the solution domain considering the presence of boundary layer over the bottom wall. The grid is clustered near the bottom wall and its density increases moving from the upstream and downstream ends of the

domain towards the hump section. The overall grid density was chosen to be relatively low considering the fact that the numerical simulation of the NASA hump is being carried out with the goal of simulating flow over a large area with complex geometry which is considerably more resource intensive. The grid has only 86000 cells while the first cell height at the bottom wall is approximately $8\times10^{-6}$m. Figure 3.3 shows overall and magnified view of the structured grid used for the simulations.

Two more grids have also been simulated and used for the grid independence study which are listed in Table 3.2 and discussed in section 3.2.2.

#### 3.2.1.4 Numerical Solution Method

The flow over all test cases in this thesis is unsteady, three-dimensional and turbulent. Therefore, the most accurate approach to CFD simulation of these cases is direct numerical simulation by discretizing the full Navier-Stokes equations in time and space. However, DNS modeling is very resource intensive and limited to the memory and processing power of the available computers.

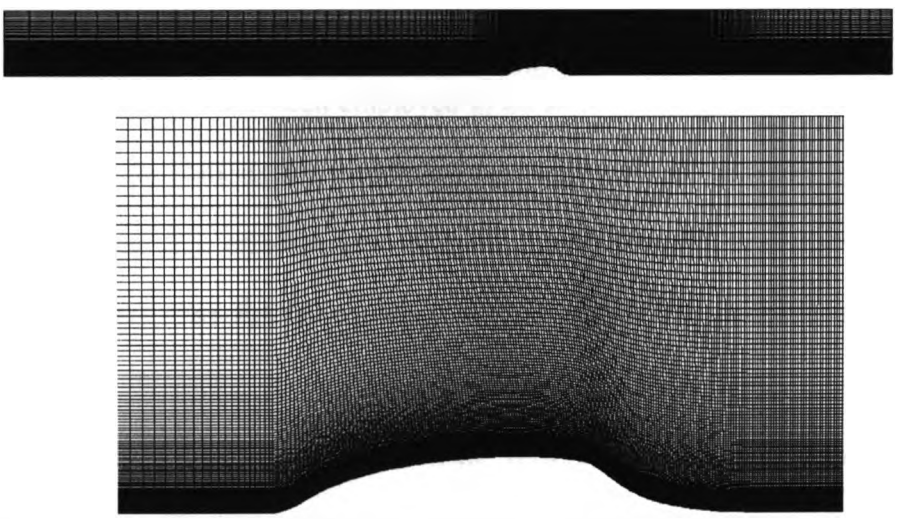

Figure 3.3: Structured grid over NASA hump model. View of the entire solution domain and magnified view of the grid around hump model.

Another modeling option is LES; this numerical scheme resolves the large turbulence structures by the filtering Navier-Stokes equations. The filtering process effectively filters out the eddies whose scales are smaller than the filter width or grid spacing used in the computations. The smaller scales are then modelled by a subgrid-scale turbulence model. Although LES can resolve a wide range of turbulence scales using coarser grids compared to DNS, it still needs the grid be so fine that only isotropic turbulence structures are left to be modelled while the rest should be resolved by the filtered Navier-Stokes equations. A few authors have attempted to employ LES to small complex topography (Uchida and Ohya (2003)). However, as reported in section 1.3.2.3, these attempts are at very basic stages and limited to relatively low Reynolds flows with large time steps imposed by the processing speed of the present supercomputers.

Employing Reynolds averaged Navier-Stokes (RANS) equations in CFD simulations is the most efficient solution in terms of model size and processing time. The RANS equations only resolve the averaged flow quantities and model the turbulent structures. The range of modelled turbulence scales depends on the turbulence model, flow complexity and grid. Although the test cases in this work are unsteady in nature, the steady RANS equations have been employed in all simulations given that the Unsteady-RANS (URANS) simulations for a complex topography model can take more than six months per test case. The effectiveness of steady RANS simulations is discussed for the presented test cases. The RANS equations need a turbulence model to solve for the Reynolds stresses. Selecting of the proper turbulence model along with appropriate near wall treatment is essential to obtain realistic flow simulations. Different turbulence models that were used in simulating the NASA hump problem are explained below.

The CFD simulations for all cases in this chapter were carried out in commercial software FLUENT (Version 6.2.16). The governing equations for this problem are two-dimensional steady RANS equations without heat transfer. Spalart-Allmaras, k-ε, k-ω and RSM turbulence models were used in simulating the hump flow.

Spalart-Allmaras model is a single equation turbulence model which solves for turbulent kinematic viscosity. It is designed to work throughout the boundary layer and is capable of resolving the near wall turbulence providing the grid is fine enough.

The k-ε model solves two equations for turbulence kinetic energy and turbulence dissipation. In deriving the semi-empirical equations of the standard k-ε model, it is assumed that the flow is fully turbulent and the effects of molecular viscosity are negligible. Therefore, k-ε models can not be used directly near the wall boundaries. The RNG k-ε model is derived analytically from the instantaneous Navier-Stokes equations and has an additional term in dissipation equation compared to the standard k-ε. This model has been found to work best for rapidly strained and swirling flows. The Realizable k-ε model uses new formulations for turbulent viscosity and has a new equation for dissipation which has a mathematical constraint on normal stresses to be physically valid. This model is recommended for flows with strong adverse pressure gradients, separation and recirculation. Hence, realizable k-ε turbulence model was used in this study.

Standard k-ω is an empirical model that solves two equations for turbulence kinetic energy and specific dissipation rate. This model is recommended for low Reynolds flows, wall-bounded boundary layer and transitional flows. Shear Stress Transport (SST) k-ω model is based on the standard k-ω but employs a high Reynolds version of k-ε model for

the outer layer of the boundary layer. The model gradually changes from the k-ω model within the inner layer of the boundary layer to k-ε model. It also employs a modified turbulent viscosity model to include the transport effects of the principal turbulent shear stress. This model operates in a wider range of flows such as cases involving adverse pressure gradient on airfoils and wall bounded flows. Therefore, SST k-ω is widely used in the present work.

Reynolds stress model is a five equation model solving directly for the turbulent shear stress components and therefore avoiding isotropic formulation of turbulent viscosity. It is suitable for complex three-dimensional flows with strong swirl and rotation. However, it is substantially more memory and time intensive compared with the two equation models.

Among the discussed turbulence models, only Spalart-Allmaras and k-ω (when employed using specific coefficients suitable for transitional flows) models are designed to function properly throughout the boundary-layer - provided the near wall grid satisfies the $y^+ < 300$ condition, where $y^+ = \frac{u_\tau}{\nu} y$ is dimensionless wall distance ( $u_\tau$ , friction velocity; ν, local kinematic viscosity). The rest of the turbulence models and LES scheme are primarily valid for core flows far from the walls. For near wall regions wall functions must be incorporated. Standard wall functions provided by FLUENT assume the grid cells adjacent to the wall are large enough to embed turbulent viscous sublayer and buffer layer inside themselves and therefore they employ an empirical logarithmic equation to blend the near wall boundary layer characteristics to the core flow. This require the first layer of cells next to wall have $30 < y^+ < 300$ . On the other hand, enhanced wall functions automatically adjust the equations to accommodate for the linear velocity

profile inside the viscous sublayer ( $y^+ < 5$ ), within the buffer layer ( $5 < y^+ < 30$ ) and outside the buffer layer while $y^+ < 300$ . However, it is recommended to avoid using grid cells within the buffer layer. Both standard wall functions and enhanced wall functions are used for the hump model simulations for the sake of evaluation.

In order to solve the turbulence model and governing equations in the computational domain, the equations are discretized in space domain with second-order accuracy (unless otherwise stated) using the finite volume approach. The equations are solved using a segregated implicit scheme provided by FLUENT. Note that the pressure-velocity coupling in discretized equations is achieved by SIMPLE algorithm. For further details on the specific turbulence model constants and the abovementioned numerical scheme please refer to the FLUENT documentation (FLUENT 6.3.26 User's Guide (2007)).

### *3.2.2 Results and Discussion*

The final grid independence study was performed by trying three different grids and grid sizes listed in Table 3.2. However, a number of medium sized grids with different configurations for wake region and near wall regions were tested. To examine the grid independency of the simulation, the lift of the hump model (only the component of the lift generated by pressure distribution) was calculated for each case. Since, the lift force is an integral of the pressure distribution on the hump surface it can be a good measure of the accuracy of the model. Table 3.2 shows the calculated lift and skin friction coefficients along with their percentage difference with the very fine case (180000 grid cells). The results confirm that the very fine grid case produces the same results as the second case. Therefore the rest of the analyses are based on grid case 2. Also, the values

of $y^+$ where checked for the lower wall and it was seen that they all fell within the acceptable range of 0.5 to 3.5. Moreover, the near wall grid was also refined without changing the entire domain grid structure to verify the convergence. It was found that the entire flow simulation is more dependent on the near wall grid rather than simply doubling or tripling the number of grid cells in the domain. The calculated average skin friction coefficients on the hump for the cases with grid cells being larger than the buffer layer and viscous sublayer (i.e $30 < y^+ < 300$) were found to be very different from those generated by the grids listed in Table 3.2.

Figure 3.4 shows the calculated and measured mean velocity profiles at the x/c=-2.14 (upstream of the hump). The overall matching of the profiles with the measured values indicates the proper selection of the upstream inlet length to develop the desire boundary layer from uniform velocity inlet condition. It is noticed that the RSM model predicts the inner layer of the boundary layer perfectly; however, the velocity at the mid-layer (i.e. $0.02<y/C<0.08$) is under-predicted. This might be attributed to the nature of the RSM equations which solve for all the Reynolds stress components and therefore producing more turbulent viscosity which is noticeable where the wall functions are blending into the core turbulence equations. Both SST k-ω and k-ε model slightly over-predict the velocity within the near wall area; however, SST k-ω model seems to produce more a accurate profile. This can be related to validity of the model for near wall regions (without using wall functions).

Table 3.2: Grid independence study for the NASA hump.

| Grid size | Lift due to pressure coefficient | Difference in lift (%) | Skin Friction Coefficient | Difference in skin friction (%) |
|---|---|---|---|---|
| 63000 | 0.4150 | 5.95 | 0.0037344 | 7.97 |
| 86000 | 0.4413 | 0.02 | 0.0034368 | 0.05 |
| 180000 | 0.4414 | --- | 0.0034351 | --- |

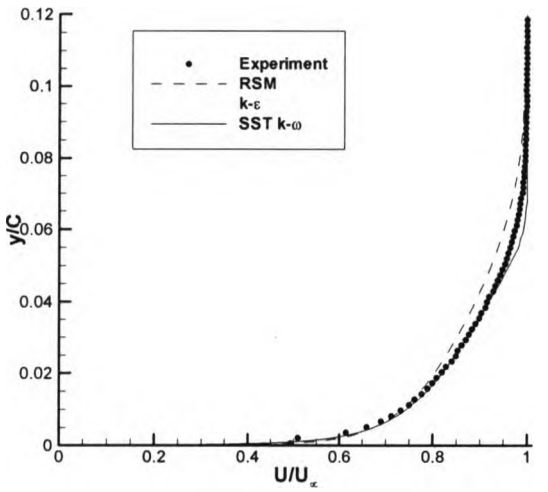


Figure 3.4: Mean velocity profiles at x/c=-2.14.

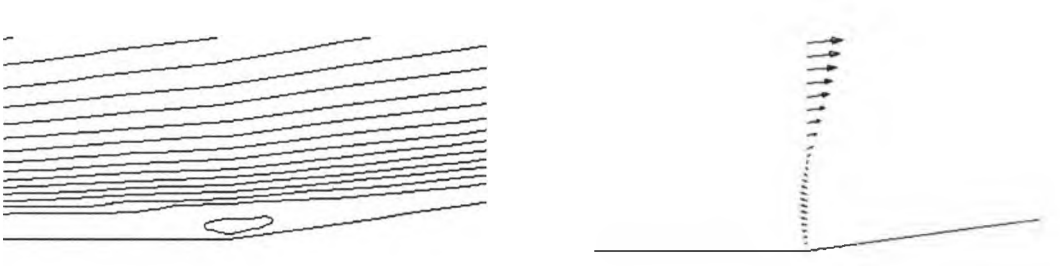

(a) (b)

Figure 3.5: Non-physical separation in leading edge (x/c=0). (a) Contours of velocity, (b) velocity vectors, Flow direction is from right to left.

Figure 3.5 shows magnified views of the velocity contours and vectors at the leading edge of the hump when very fine grids are used (the height of the magnified profile is approximately 0.04mm). The simulations show a non-physical separation bubble at leading edge regardless of the choice of turbulence model. This was also observed by Naughton et al. (2004) in the CFD simulations results but not the oil film skin friction measurements.

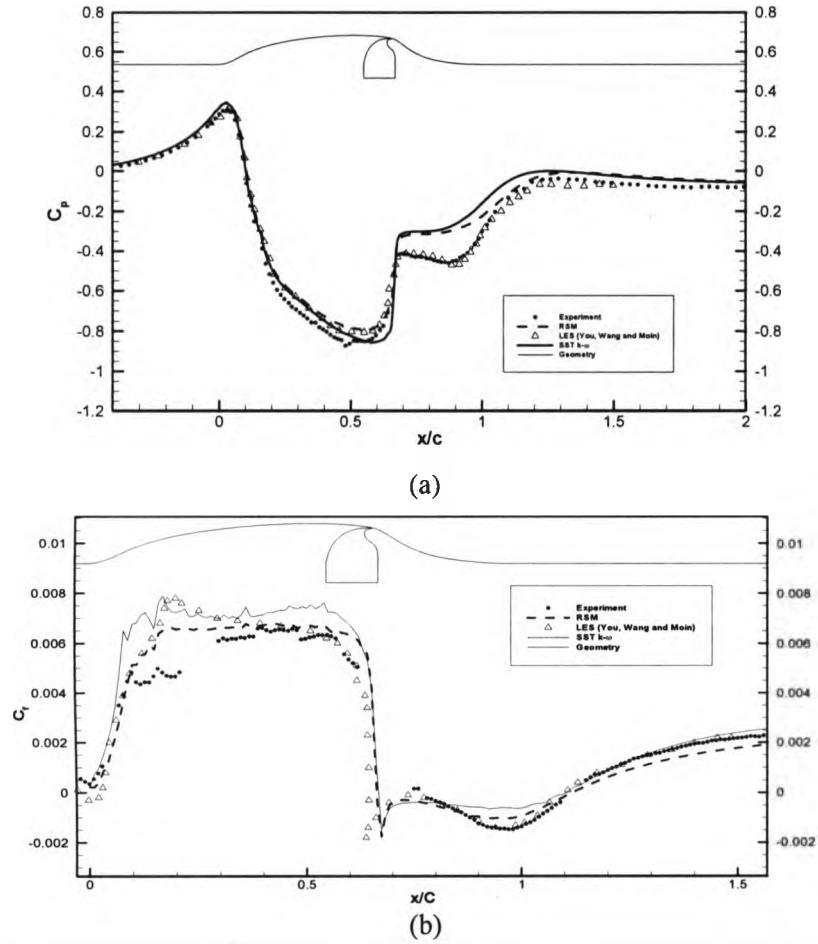


Figure 3.6: Pressure (a) and skin friction (b) coefficients on the hump surface obtained by SST k-ω and RSM turbulence model.

The surface pressure and skin friction coefficient on the hump surface are compared for different turbulence models including the LES simulations by You et al. (2006). Figure 3.6(a) shows that the LES simulations perfectly match with the measured values. On the other hand, SST k-ω and RSM turbulence models with steady RANS equations under-predict the surface pressure in the recirculation region. However, the separation point is correctly captured. RSM model demonstrates better overall results. Figure 3.6(b) compares the skin friction coefficients calculated using different turbulence models. The LES simulations predict the surface friction perfectly in the separation bubble area and

downstream of it. However, it appears that all the turbulence models have problems in simulating proper near wall conditions where the hump has a mild upward slope ($0.1<x/C<0.3$). As expected, RSM model predictions inside the separation bubble are closer to measurements compared with SST k-ω. The skin friction coefficient wiggles over the rising slope of the hump for SST k-ω and RSM are generated as a result of near wall grid refinement based on the $y^+$.

Velocity profiles for four sections on the hump are presented in Figure 3.7. The velocity profiles for the section located at the leading edge of the hump (C1) are almost identical for both RSM and SST k-ω turbulence models. It can be observed that the mid layer is slightly over-predicted by k-ω model. In section C2, where the flow accelerates on the hump surface, the RSM model demonstrates less speed up effect. Since the RSM model fully resolves the shear stress components, it predicts higher turbulent viscosity causing in less speed up effect relative to the k-ω model. Section C3 lies over the hump surface where the separation starts. The PIV measurements from Naughton (2004) are also compared with the simulated values. Both models present higher velocity values resulting in a separation point slightly forward from the point observed in experiments. Section C4 is inside the recirculation region and the velocity profiles show presence of the reversed flow. The CFD predictions produce a small separation bubble compared with the experiments. This is normally observed in steady RANS simulations; only LES or DES simulations can accurately model the separation region.

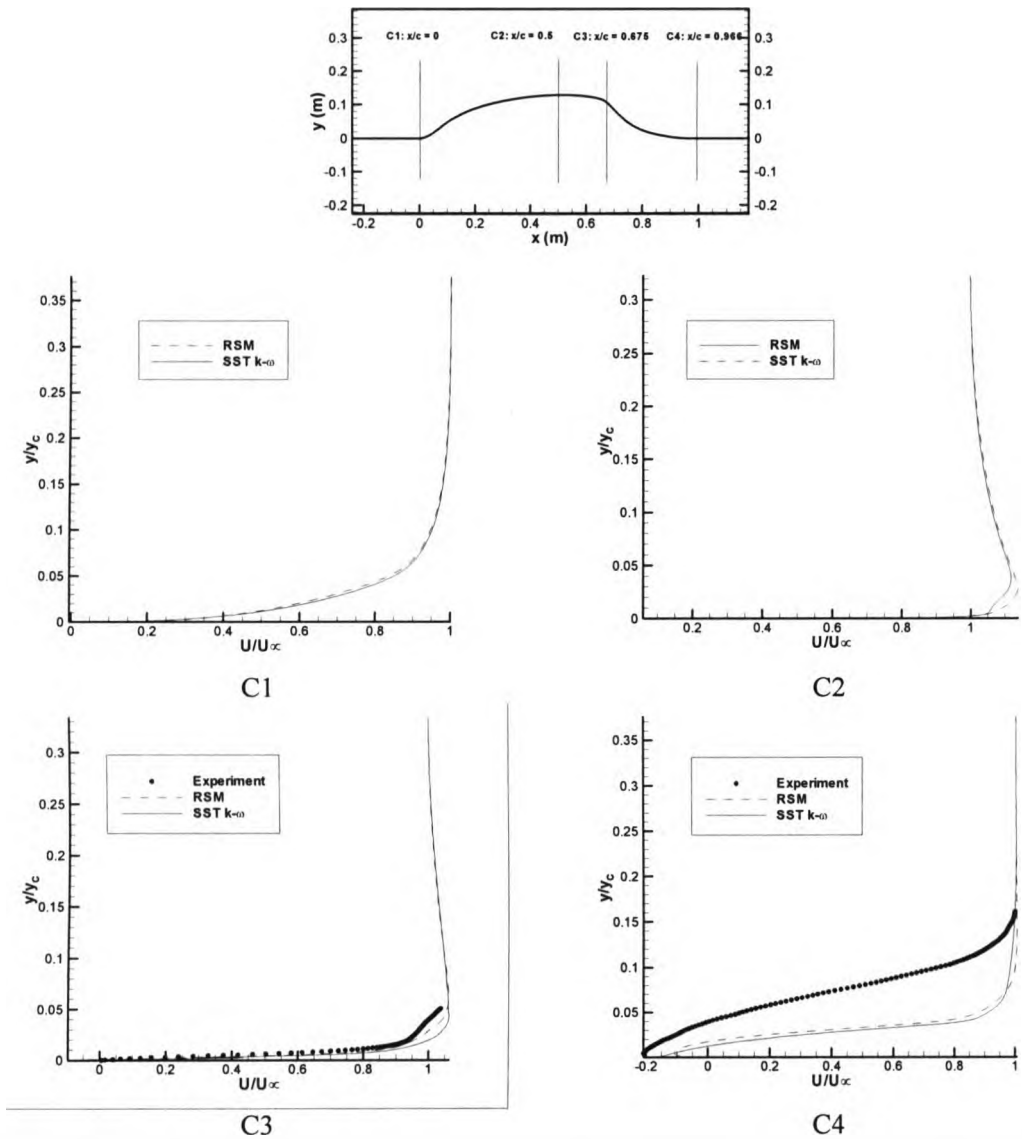


Figure 3.7: Velocity profiles in four sections over the hump for SST k-ω and RSM turbulence model. C3 and C4 are also compared with measurements.

### *3.2.3 Conclusions*

The two-dimensional flow over NASA hump model was studied for the purpose of evaluating different turbulence models on predicting the flows with acceleration, separation and reattachment regions. Pressure and surface friction coefficient on the hump model as well as velocity profiles on different areas along the hump were

discussed. The results show that the steady RANS models were found to predict smaller separation region in comparison with the measured values. The SST k-ω model tends to slightly over-predict the velocity values in the inner region of the boundary layer. Unsteady LES model provides accurate results for the separation region and downstream; however the steady RANS simulations (RMS and k-ω) presented more accuracy with less computational effort. It must be noted that the RSM model requires considerably larger resources compared with k- ω model, which becomes a serious issue in simulating very detailed large domains such as complex topography

## 3.3 Three-Dimensional Simulation – Generic Hill

Flow over a three-dimensional hill model is studied for the purpose of determining the most suitable domain size and evaluating the CFD model in simulating the wake region behind this symmetric test case.

The introduced axisymmetric hill model has a cosine squared cross section and a maximum slope of 32°. Hot-wire measurements and numerical simulations for this model were carried out by Ishihara et al. (1999 and 2002). The hill model has maximum height of h=4cm with its diameter being 2L=20cm. The shape function for the model is defined in equation (3.1). Along wind cross section of the hill model is shown in Figure 2.1.

$$z_s(x,y) = h\cos^2\left(\frac{\pi\sqrt{x^2+y^2}}{2L}\right) \tag{3.1}$$

Results such as velocity profiles at hill foot, mid slope sections are available for upstream and downstream of the hill at the central cross wind and along wind cross sections.

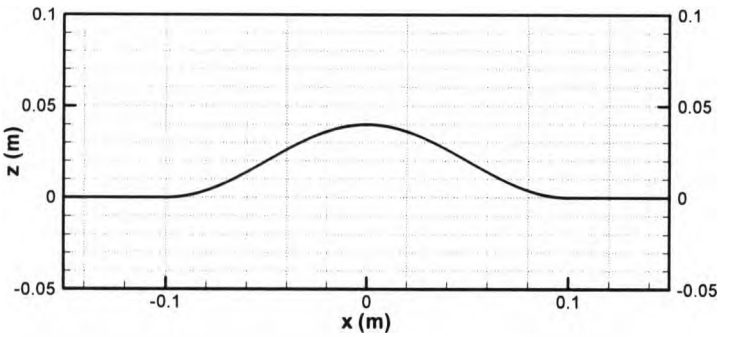


Figure 3.8: Middle section profile of the three-dimensional hill.

### *3.3.1 Numerical Setup*

The flow conditions for the generic hill model are listed in Table 3.3. The flow Reynolds number based on the hill height ($Re_h$) is 14600. The three normal stress components were available in profiles at the inlet; however, an averaged value of the three components is used (see 3.3.1.2).

#### 3.3.1.1 Solution Domain

The generic hill model was simulated in a number of rectangular domains, where the model was on the bottom surface of the domain. Figure 3.9 shows a schematic of the domain and hill model. Note that the origin of the coordinate system is the center of the hill, with its x-axis aligned with the flow direction.

Table 3.3: Flow conditions for generic hill model.

| | |
|---|---|
| Maximum inlet velocity ($U_\infty$) | 5.5m/s |
| Inlet velocity profile | $\frac{U}{U_\infty} = \left(\frac{z}{0.2}\right)^{0.135}$ |
| Maximum turbulence intensity at the inlet | 5.7% |

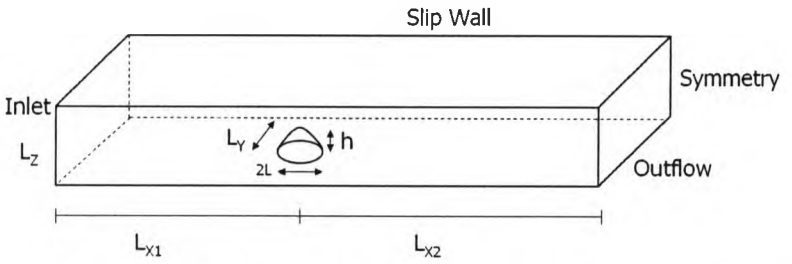


Figure 3.9: Solution domain and boundary conditions for three-dimensional hill.

Table 3.4: The different domain dimensions used in the generic hill study.

| Case Number | $L_{X1}$ | $L_{X2}$ | $L_Y$ | $L_Z$ |
|---|---|---|---|---|
| 1 | L | 6L | 4L | 3h |
| 2 | L | 6L | 4L | 9h |
| 3 | L | 6L | 4L | 12h |
| 4 | 3L | 6L | 4L | 3h |
| 5 | 3L | 6L | 4L | 9h |
| 6 | 3L | 6L | 4L | 12h |
| 7 | L | 9L | 4L | 3h |
| 8 | L | 9L | 4L | 9h |
| 9 | L | 9L | 4L | 12h |
| 10 | 3L | 9L | 4L | 3h |
| 11 | 3L | 9L | 4L | 9h |
| 12 | 3L | 9L | 4L | 12h |

A number of domains with varying height, length and width were tested (Table 3.4) and finally case 11 was selected (see 3.3.1.4).

### 3.3.1.2 Boundary Conditions

The boundary condition for bottom wall of the domain was considered as a no-slip wall without roughness. The top wall was specified as zero-shear stress (or slip wall) to prevent boundary layer formation. The side walls were assigned symmetry boundary conditions. The outlet boundary is outflow boundary condition which incorporates the assumption that the flow is fully developed at the outlet boundary in this case. Figure 3.9

illustrates the boundary conditions on the solution domain. The inlet boundary is a velocity inlet with specified profile of mean velocity shown in Table 3.3. Since the employed turbulence model is an isotropic model, the three turbulence normal stress components measured in experiments provided by Ishihara et al. (1999) were averaged and imposed on the inlet boundary as a single turbulence intensity profile.

#### 3.3.1.3 Grid

A hybrid grid was generated in the solution domains with structured clustered grid cells at the bottom wall boundary. The structured section of the grid has 11 layers of clustered cells with the first cell height being 0.001m. The surface grid has triangle elements which generate the three-dimensional grid cells when extruded in normal to surface direction. The average edge length of the face mesh near and on the hill model is 0.002m. The rest of the domain was filled with tetrahedral cells smoothly blending the fine grid cells on the bottom wall to the relatively coarse cells near the other walls. Figure 3.10 illustrates the grid structure explained above, on a smaller domain described in section 3.3.1.1. Different grids listed in Table 3.4 were generated in such a way that they shared approximately the same elements sizes, with the larger domains holding more cells due to the extra space they provided.

Two more grids for case 11 have also been generated for the grid independence study which are listed in Table 3.5 and discussed in section 3.3.2.

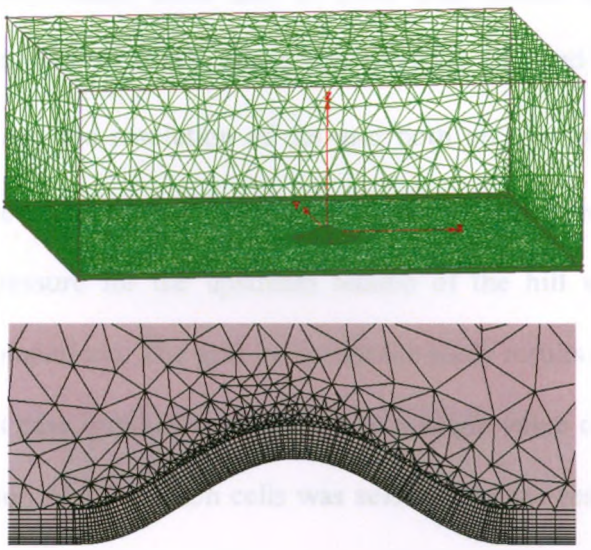

Figure 3.10: Hybrid grid over three-dimensional hill model. View of the entire solution domain and zoomed sectional view of the grid around hill model.

#### 3.3.1.4 Numerical Solution Method

The governing equations are steady three-dimensional RANS coupled with SST k-ω turbulence model. The set of coefficients adjusted for transitional flows are used for the SST model. Spatial discretiziation is second-order; segregated implicit solver is used with SIMPLE pressure-velocity coupling method.

### *3.3.2 Results and Discussion*

Different simulations using numerical domains listed in Table 3.4 were carried out. The overall quality of the flow properties such as velocity and pressure were examined in the along wind middle section of the domains. It was observed that smallest domain that does not demonstrate any disturbance imposed by the domain boundaries is case 11 which has upstream length of 3L, downstream length of 9L and height of 9h above the surface.

For the grid sensitivity study, three sets of grids with similar quality but different resolutions were used. The first cell height was carefully adjusted to accommodate for the $y^+ < 5$ condition, and the resolution of the grid both on hill surface and in vertical direction was increased. The surface friction coefficient for the entire hill surface and lift coefficient due to pressure for the upstream section of the hill were calculated as a reference point for comparison. The grid independence study results for case 11 are listed in Table 3.5. For this case, gradual convergence to a single value can be observed. The grid with the resolution of 1.2 million cells was selected for the results presented in the rest of this section.

Studying the same case with different grid styles and sizes showed that it is very important to change grid resolution both in vertical and horizontal direction. As a matter of fact, the vertical resolution is limited to the $y^+$ and the first grid cell height near the wall; therefore, the best obtained vertical resolution lies in a very limited range making the grid sensitivity verification less trivial. One can change the vertical resolution in areas very far from the wall, but this was found to impose extremely slight changes to the flow properties within the area of interest (which is near wall boundary regions for wind engineering cases). On the other hand, increasing the horizontal resolution will end in resolving the geometry more accurately and obviously creating more meaningful results. This is a feasible approach for the simple geometries such as generic hill test case; but it can become a major source of concern when dealing with very complex geometries such as a real topographic terrain where the CFD model must be created with the highest resolution in horizontal direction to the memory and processing limits.

Table 3.5: Grid independence study for the generic hill.

| Grid size | Lift due to pressure coefficient for upstream half | Difference in lift (%) | Surface friction coefficient for the hill | Difference in surface friction (%) |
|---|---|---|---|---|
| 400000 | $-5.6798\times10^{-3}$ | 6.5 | $4.2558\times10^{-3}$ | 10.6 |
| 1.2 million | $-5.3347\times10^{-3}$ | 0.03 | $3.8061\times10^{-3}$ | 0.07 |
| 2.6 million | $-5.3331\times10^{-3}$ | --- | $3.8035\times10^{-3}$ | --- |

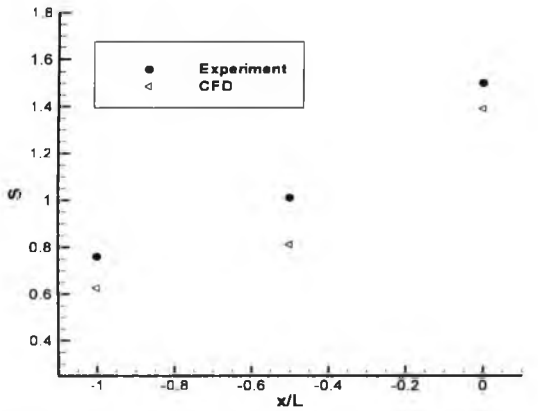


Figure 3.11: Speed-up ratios (S) for three locations over the hill (hill foot, mid slope and summit).

The mean speed-up ratio has always been at the center of interest in structural design and wind energy estimates. The speed-up ratio (S) definition is provided in equation (3.2).

$$S = \frac{U(z)}{U_0(z)} \tag{3.2}$$

where, $U(z)$ is the streamwise velocity profile, and $U_0(z)$ is the streamwise velocity profile in the same location but in absence of the hill. Note that z is distance from surface. Figure 3.11 compares the speed-up profiles at z/h=0.13 above the hill surface on the middle section (y/L=0) for three different locations: on the hill foot, mid slope and summit of the hill. The experimental results are from Ishihara et al. (1999) who verified their measurements at z/h=0.13 with results from Arya and Gadiyaram (1986). CFD simulations perfectly predict the trend of the increase in speed-up; however, the speed-up

values are slightly under-predicted. Measurement results at x/L=-0.5 (mid slope) imply almost no influence from the presence of hill (S=1) but the CFD model predicts flow retardation in that section.

To achieve more understanding of the flow quality downstream of the hill, the velocity profiles at four sections downstream of the hill are presented. Figure 3.12 (a) compares the measured and velocity profiles at the summit of the hill (y=0, x/L=0). The overall match of the profiles and flow acceleration is within the acceptable range. As observed in Figure 3.11, the predicted values are slightly smaller than the measured ones. Figure 3.12 (b) shows the profiles on a section inside a recirculation region (x/L=0.45). As it was observed in section 3.2.2 for the hump model, the CFD model predicts a smaller separation bubble. Figure 3.12 (c) and (d) demonstrate the profiles on the downstream of the hill, along mid section. The reverse flow in the recirculation region can be observed for both CFD and experimental results.

### *3.3.3 Conclusions*

CFD models for the flow over a generic three-dimensional hill were carefully examined in order to achieve an understanding of the effects of the simulation domain size on the final results. Moreover, the flow properties for the generic hill were compared with experimental values to verify the CFD model in producing acceptable results for wind engineering purposes. Different solution domain sizes were examined the minimum solution domain dimensions for these types of simulations were found. Any domain that has the wall boundaries 3L upstream, 9L downstream and 9h above the model, can safely be assumed to suffer the least interference from the boundaries while employing the optimally sized domain.

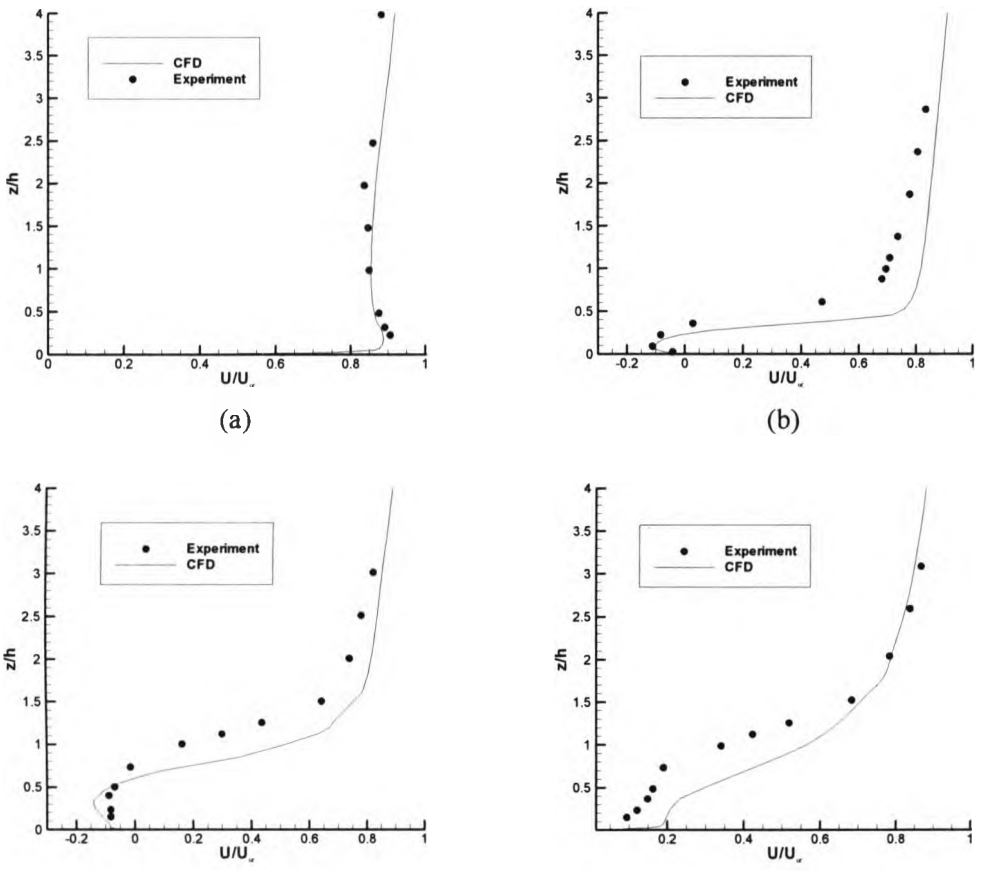


Figure 3.12: Streamwise velocity profiles on four locations on the mid section of the hill (y/L=0) at (a) x/L=0, (b) x/L=0.45, (c) x/L=1.0 and (d) x/L=1.5. The experimental values are from Ishihara et al. (1999).

Speed-up ratios were compared with experiments and CFD model was found to rightly predict the trend in speed-up increase along hill. However, the simulated flow acceleration was slightly under-predicted. The study of flow downstream of the hill revealed that the steady RANS simulations do not model the separation region as large as it is observed in experiments.

## 3.4 Complex Topography Simulation – Hong-Kong Model

The Hong-Kong CFD model is sharing the same geometry and boundary conditions with the cases explained in the previous chapter. The cases are simulated considering the physical topography model orientation in the wind tunnel and the wind tunnel dimensions and flow conditions.

The topography model dimensions are 4.7m×4.7m covering a full scale area of 14km×14km. The model is very complex and consists of different features; however, one can roughly assume that it is composed of few large geometric features that are 0.65m wide (L) and 0.4m high (h). This approximation can provide a general idea of the model in analyzing the boundary conditions and solution domain size.

The results from the PIV measurements on the topography model explained in the previous chapter are used in verifying the CFD simulations.

### *3.4.1 Numerical Setup*

Creating a surface model of the topography from the available databases is the key part in CFD modeling of flow over topographies. When modeling a simple geometry or surface models with limited number of key points, conventional techniques can be successfully used to generate a CAD/CAM model of the geometry and using it in grid generation software. However, the topography models consist of large raster files that can not be used as input for CAD/CAM or grid generation software. A universal algorithm to generate a CFD model for simulation the flow over topography starting from the GPS coordinates of a region is designed and used for Hong-Kong test case (Figure 3.13). Digital Elevation Model (DEM) for most of the regions can be found in Geographic Information System (GIS) portals or map libraries. The digital data is available in point

cloud format and the topography maps can be digitized into elevation contour maps. For the case of southeast Hong-Kong the data was available in digitized elevation contour maps (Figure 3.14(a)). The contours were converted into point cloud files and Kriging interpolation technique was used to create a surface model of the topography in the desired resolution (in this case 48m×48m). Kriging interpolation is a group of geo-statistical techniques which helps to interpolate data in a region that a limited number of data points are available for them; this model is available to use with very large data files in all GIS software and some surface analysis tools. The interpolation results are in point cloud format, but arranged in a specific grid where the elevation is known for each grid point. This dataset can be used to create a NURBS (Non-Uniform Rational Basis Spline) model resulting in a surface model that can be recognized in all CAD/CAM and grid generation software ((Figure 3.14(b))). Many of the CAD/CAM software use the NURBS mathematical model to handle free-form shapes; but to the knowledge of the author, none of them can handle the very large scattered point cloud datasets such as digitized elevation contour maps unless they are processed using the Kriging interpolation. Once the surface model is in NURBS format it can be imported to the grid generation software.

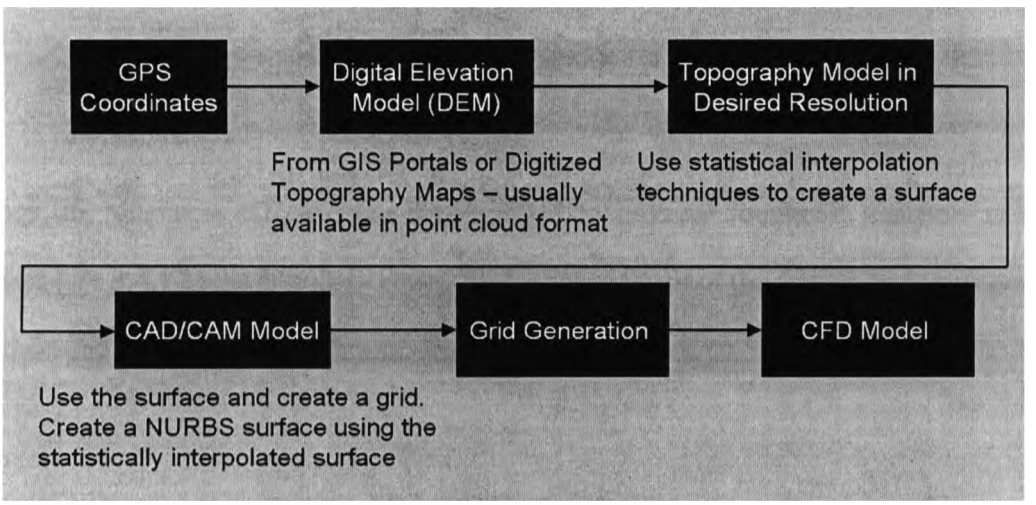


Figure 3.13: Modeling procedure for complex topographic terrains.

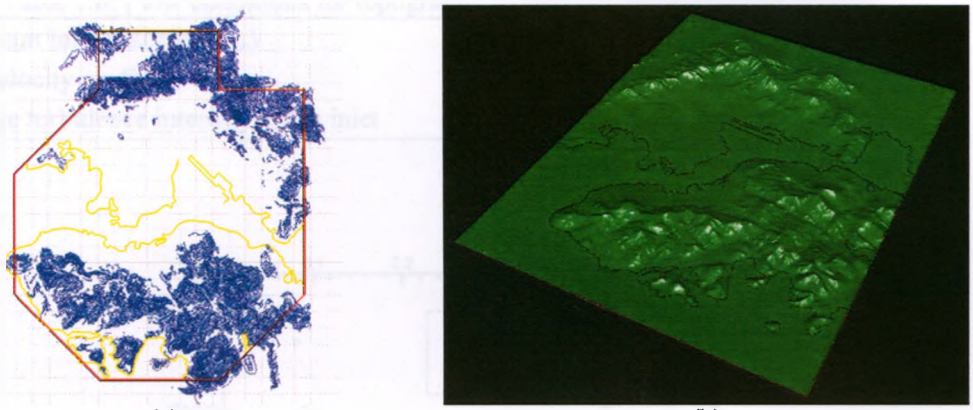

(a) (b)

Figure 3.14: Southeastern Hong Kong model. (a) Digital elevation model (b) NURBS surface.

Three different surface models were created for the hill, valley and ridge test cases with respect to their orientation in the wind tunnel (see section 2.2.2). In this study Pointwise V16.03 was used in creating the grids.

#### 3.4.1.1 Solution Domain

The flow conditions for the topography model are listed in Table 3.6. The flow Reynolds number based on the height of largest geometric feature on the model ($Re_h$) is 197000. The velocity and turbulence intensity profiles on the upstream of the topography model are available from the hot-wire measurements in wind tunnel which are shown in Figure 3.15.

#### 3.4.1.2 Boundary Conditions

Since the roughness effects were implemented as physical roughness elements in the model (see 3.4.1.3) the boundary condition for bottom wall of the domain was considered as a no-slip wall without roughness.

Table 3.6: Flow conditions for topography model: hill, valley and ridge cases.

| | |
|---|---|
| Maximum inlet velocity ($U_\infty$) | 7.44m/s |
| Inlet velocity profile | Figure 3.15 |
| Average turbulence intensity at the inlet | 25% |

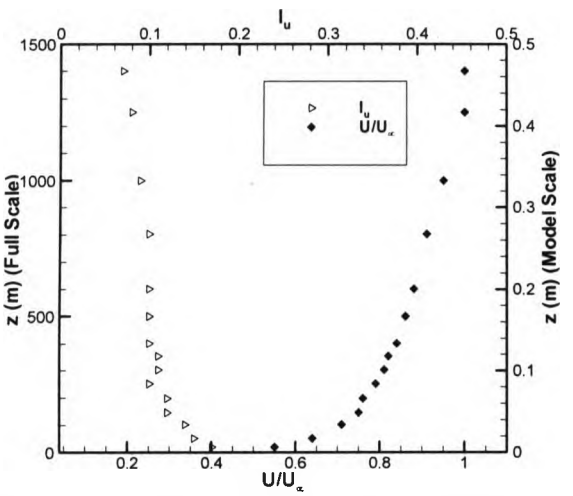


Figure 3.15: Streamwise velocity and turbulence intensity profiles upstream of the topography model from hot-wire measurements.

The top wall was specified as zero-shear stress (or slip wall) to prevent boundary layer formation. The side walls were assigned symmetry boundary conditions. The outlet boundary is outflow boundary condition which incorporates the assumption that the flow is fully developed at the outlet boundary in this case. Figure 3.16 illustrates the boundary conditions on the solution domain. The inlet boundary is a velocity inlet with specified profile of mean velocity and turbulence intensity shown in Figure 3.15.

#### 3.4.1.3 Grid

A hybrid grid was generated in the solution domains with structured clustered grid cells at the bottom wall boundary (the same methodology used in generic hill simulations).

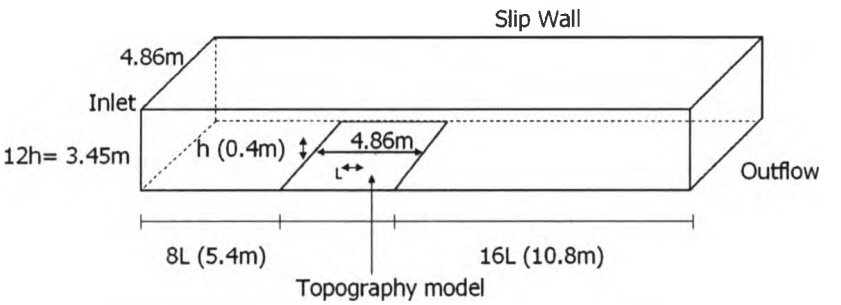


Figure 3.16: Solution domain and boundary conditions for topography models.

The structured section of the grid has 6 layers of clustered cells with the first cell height being 0.002m (6mfull scale). Unfortunately, the topography surface model has many sharp curves and steep slopes creating sharp angles which do not allow for more than 6 layers of clustered grid cells on the wall in topography region. However, the grid for the upstream area employs 13 more layers of structured cells.

The surface grid has triangle elements which generate the three-dimensional grid cells when extruded in normal to surface direction. The average edge length of the face mesh on the topography model is 0.016m (full scale 48m). Each cell on the topography surface covers an area of 1.28cm$^2$ (full scale 1152m$^2$). The rest of the domain was filled with tetrahedral cells smoothly blending the fine grid cells on the bottom wall to the relatively coarse cells near the other walls. Figure 3.17 illustrates the grid structure. The resulting grid size is 4.1 million cells.

As described in section 2.2.2, the high roughness height of the built-up urban are was reproduced by distributing a number of small foam blocks in the wind tunnel mode, each of them representing a tower or a building.

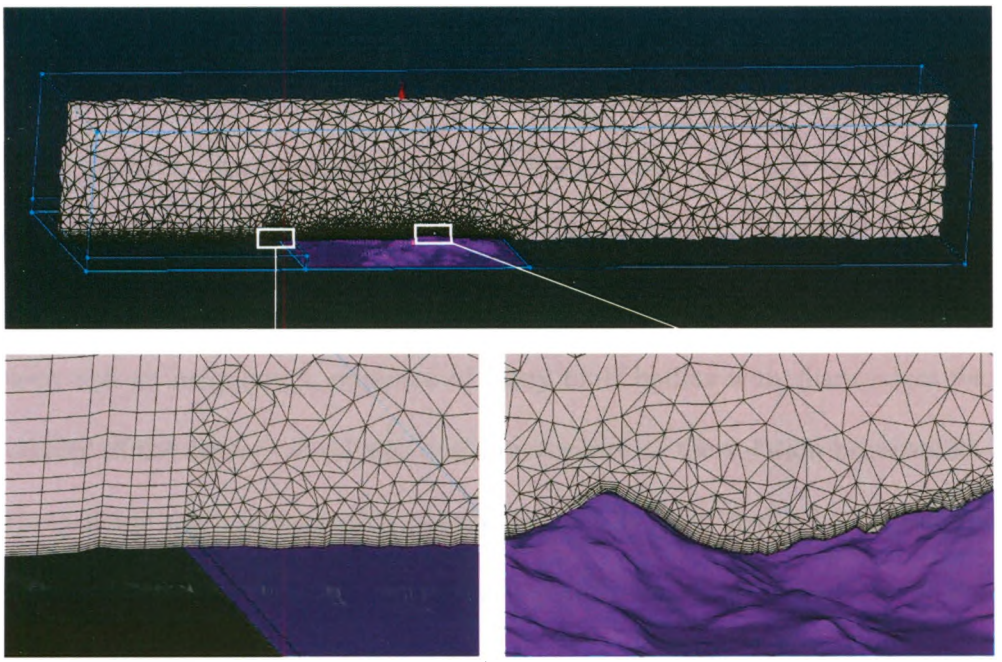

Figure 3.17: Hybrid grid over topography model. View of the entire solution domain and magnified view of the grid near topography surface.

In CFD simulations there are a few options in implementing the roughness in atmospheric boundary layer such as: incorporating the roughness in wall functions, minimizing the upstream domain length and directly imposing the boundary profile in the inlet boundary condition, specifying wall shear stress at the wall boundary conditions and physically modelling the roughness elements (Blocken et al. (2007)). Since the roughness height is relatively large in the upstream area for valley and hill test cases (urban area, densely populated by towers and high buildings) it is almost impossible to imply roughness in wall functions; specifying shear stress on the wall eliminates the presence of realistic boundary layer profiles near the wall which is not acceptable for the purpose of this work. It was found that the best options is to decrease the upstream length as much as possible to impose the boundary layer profile on the inlet. However, for the complex case of south eastern Hong Kong, the built-up area is split by water surface separating the

mainland from Hong Kong Island (see Figure 2.2). Also, the area of the land covered by building varies along the shore. Therefore, it is required to physically model the roughness elements (herein foam blocks, see Figure 2.3) in the CFD model. Physically modeling of the roughness blocks has two major limitations: the grid should be fine enough to capture the boundary layer and the small scale turbulent structures caused by the block and its neighbours, presence of many bluff bodies with sharp edges weakens the stability of the numerical scheme and convergence of the solution becomes an issue. The Hong Kong topography model is very detailed by itself and it has caused the grid size to exceed 3.5 million cells; therefore, the roughness blocks can not be modeled exactly as they are.

As a result, a new approach is introduced to physically model the roughness blocks for problems of this kind. A roughness density ratio is used to find the equivalent density of bell-shaped roughness elements which are relatively large compared to the original roughness blocks. These bell-shaped roughness elements, which count less that the original blocks and are smoother in shape, are modeled in the simulation domain. Akomah (2004) showed that different arrays of roughness blocks produce equal roughness heights if they share a specific roughness ratio. The ratio is defined as the ratio of frontal area of the roughness blocks to the planform area of the region the blocks are laid out. This ratio is used in the present work in generating equivalent roughness elements in the CFD model. Akomah's (2004) experiments were based on square section roughness elements; however, to the knowledge of the author, there has been no research work available on study of bell-shape or semi-sphere roughness elements within the range of high roughness heights suitable for wind engineering purposes. Fang and Sill

(1992) thoroughly investigated different shapes of roughness elements and their effect in aerodynamic roughness length including roughness elements with the shape of spherical segment. However, the size of roughness elements was as small as 2-6mm and the resulting roughness length are not within the range of urban areas.

The topography model has more than 1000 foam blocks around the studied areas. In a randomly selected region with area of 2558cm $^2$, 279 foam blocks exists; knowing that the blocks are 3.5cm high their cross section 1cm×1cm, the roughness element density ratio becomes 0.38. In order to generate clustered grid near the topography surface, the height to width ratio of the bell-shaped elements and their population density can not exceed very large values. The different combinations of element height and population density were examined and the maximum element density of 0.33 was achieved when the distance between elements is 10cm and their height is 4.3cm (frontal area of 16.96cm$^2$). The bell-shaped elements are in staggered arrangement and 18 of them covers an area of 911cm$^2$ (see Figure 3.18(c)). The array of element is rotated for each case of valley and hill to position the elements in an angle causing maximum frontal area.

#### 3.4.1.4 Numerical Solution Method

The numerical scheme and turbulence model are identical to the generic hill model conditions which are described in section 3.3.1.4.

### *3.4.2 Results and Discussion*

As discussed in section 3.3.2 about the grid independence study, the number of near wall grid cells, quality of the wall adjacent grids and horizontal resolution of the surface grid are more important compared to the over all number of grid cells in the domain.

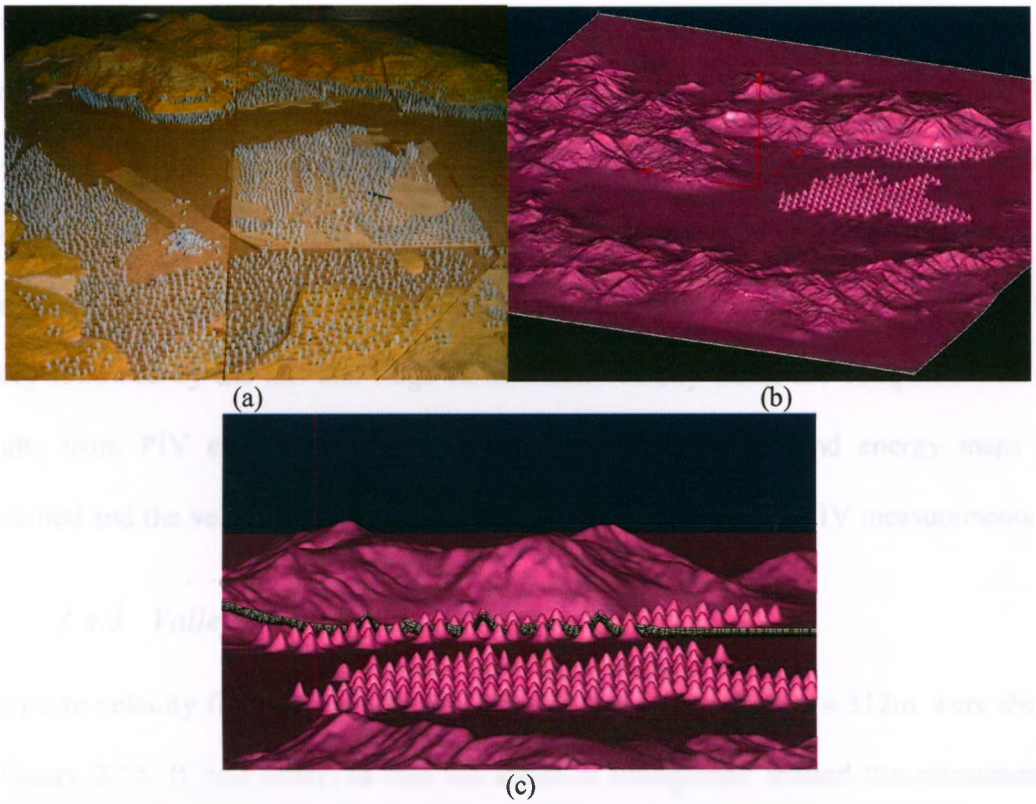


Figure 3.18: Roughness simulation in hill configuration: (a) Roughness blocks in wind tunnel model, (b) Roughness elements implemented in the numerical model, (c) the elements are staggered in an angle to produce maximum frontal area- the camera axis is in direction of free stream. Flow direction is from bottom-left corner to the top-right corner in isometric views (a and b).

Geometry for the Hong-Kong model is extremely complex and a slight decrease in horizontal resolution results in a large loss of geometry details. Therefore, the horizontal resolution of the surface grid on the topography model was carefully chosen in such a way that the CFD model uses maximum available resources on the computer used for the simulations (5GB memory, Quad core 2.4GHZ Processor). In this case the conventional procedure to verify the grid consistency which was utilized for the hump and generic hill model is not applicable. However, the same procedure that was discusses in section 3.3.2 is employed to generate the most reliable grid. Moreover, an attempt was made to verify the grid independency by clipping the width of the topography model to 80% of its size

and replacing the clipped parts with plane surface. This allowed a slight increase in the horizontal and vertical resolution of the domain while keeping the size at maximum. The flow quality in the core region and the profiles in the ridge section did not experience a change.

The results for the simulation cases are presented in the same order as section 2.3: the valley followed by the hill and ridge flow. Mean velocity fields are compared with the results from PIV experiments presented in chapter 2. The wind energy maps are presented and the velocity profiles are compared with hot-wire and PIV measurements.

### *3.4.3 Valley Flow*

The mean velocity field in two horizontal planes at $z = 195\text{m}$ and $z = 312\text{m}$ were shown in Figure 2.14. It was observed that the effect of topography around the measurement area was to divert the flow slightly towards the neighboring slope (towards positive y axis). However, by examining the contours of elevation it could be implied that the flow should deviate in negative y direction (downwards in the plot). This can be explained by visualizing streamlines in the simulation results. Figure 3.19 demonstrates streamlines released from an upstream rake for two elevations. It is observed that mean flow at the height of $z = 195\text{m}$ (Figure 3.19(a)) is mainly influenced by the U shaped ridge line that is located within a short distance in positive y direction from the measurements location. Since the flow is constrained by the rising slope in the downstream, it is being diverted to the U shaped region. Figure 3.19(b) shows in the height of z=312m, the influence of the downstream slope will fade and the flow is uniformly aligned with the free stream.

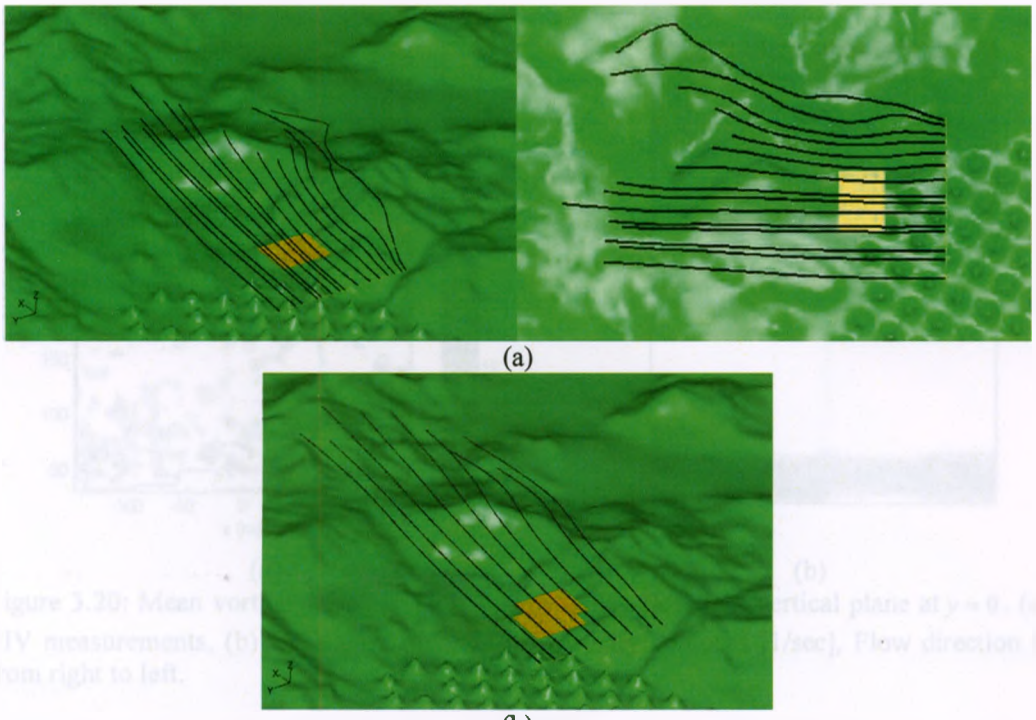

Figure 3.19: Stream lines in ridge flow released from an upstream rake at the height of (a) $z = 195\text{m}$ (b) $z = 312\text{m}$.

Figure 3.20 presents contour plots of measured and simulated mean vorticity. The flow direction is from right to left. The simulated vorticity values follow the same trend observed in the measurements. The crosswind vorticity has its maximum values in the shear layer; however, the simulated vorticity values have their maximum values in a wider band of the shear layer.

PIV, hot-wire and simulated mean velocity and turbulent intensity profiles are compared at the approximate location of $(x,y)=(0,0)$. Figure 3.21 compares the velocity profiles; the CFD simulation is in good agreement with the measurements between the ground and 150m. However, in areas above 150m the simulated values are over-predicted. Figure 3.22 shows that the predicted turbulence intensity is considerably lower than the measured values.

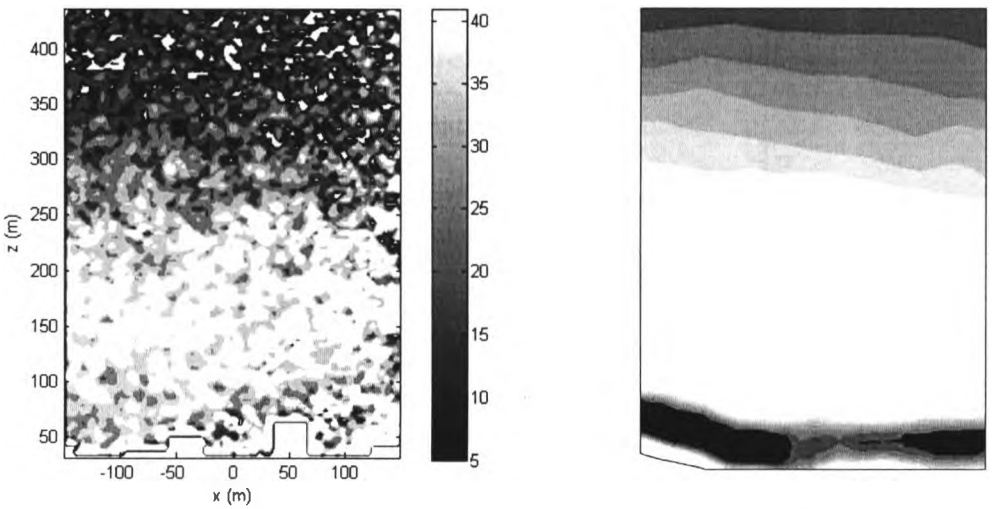


(a) (b)

Figure 3.20: Mean vorticity contour plots for the valley flow in a vertical plane at $y = 0$. (a) PIV measurements, (b) CFD simulation. Mean vorticity contours [1/sec], Flow direction is from right to left.

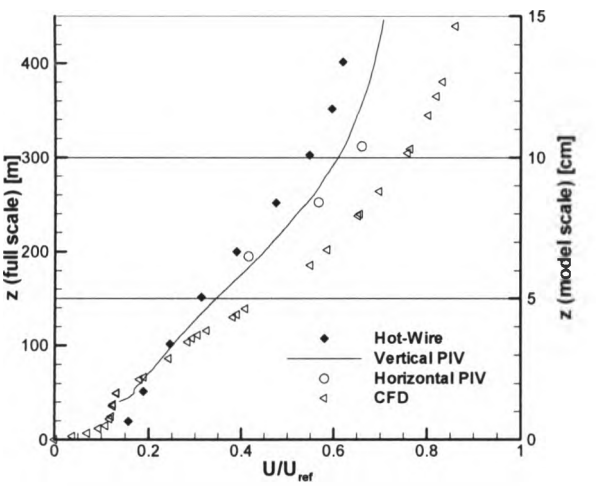


Figure 3.21: Comparison of CFD predicted mean velocity profiles by PIV and hot-wire measurements for the valley flow.

The low values of turbulence intensity are results of low turbulent viscosity which can cause the mid layer of the boundary layer predict higher velocity. Implementing the arrays of bell-shaped roughness elements helped in modeling the roughness effects near the wall and providing a reliable estimate of the velocity profiles within the inner layer.

The NASA hump test case demonstrated that the SST k-ω turbulence model predicts relatively larger velocity values compared to RSM and the experiments.

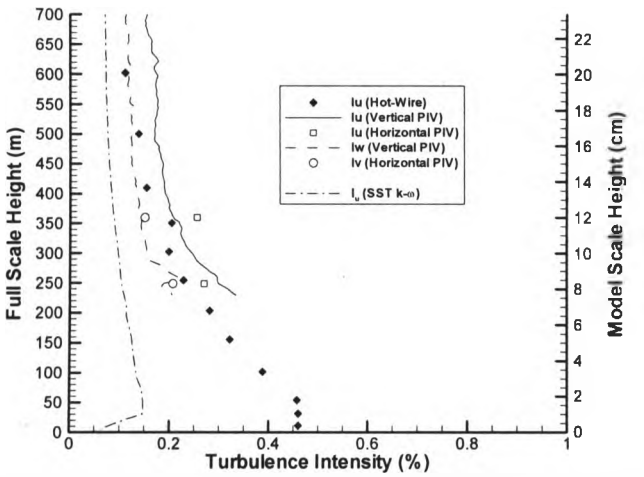


Figure 3.22: Comparison of CFD predicted turbulent intensity profiles by PIV and hot-wire measurements for the valley flow.

### *3.4.4 Hill Flow*

The CFD simulation results can be used to generate very high resolution wind energy maps. Figure 3.23 shows a three-dimensional view of mean contours of the hill velocity magnitude and wind energy coefficient at the wind turbine hub height level. The wind energy coefficient is defined as the summation of squared x and y component of the velocity normalized by square of the free stream velocity times two ($\frac{u^2+v^2}{U_\infty{}^2}$). The coefficient provides a non-dimensional measure of the available wind energy. The hub height level is assumed to be 50m. The flow direction in Figure 3.23 is aligned with the x axis, from negative to positive axis. As expected, maximum wind energy exist on the summit of the hill (x=0,y=0). However, the urban area close to the hill has caused the wind energy at the hill foot and slope become relatively smaller than the hills which are

situated in suburbs (x=-1.6,y=1.8). Notice that the grid lines in the plots are spaced in 1.7m steps (5km full scale). The mesoscale simulations provide the wind maps with maximum resolution of 5km×5km which means the whole area demonstrated in Figure 3.23 becomes only 9 cells in mesoscale simulations while the present CFD simulation has 150000 grid cells over the same area.

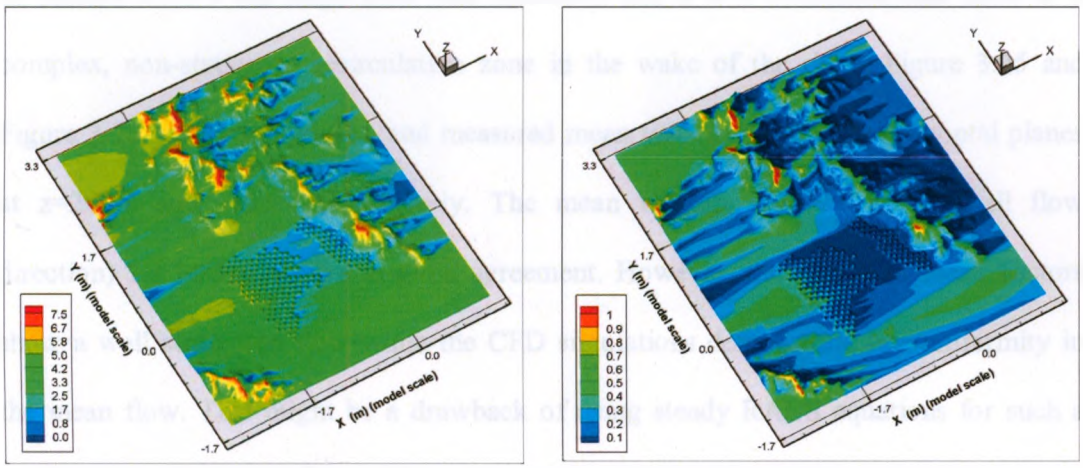


(a) (b)

Figure 3.23: Mean contour plots at hub height ( $z = 50m$ ) for the hill flow. (a) Velocity magnitude contours [m/s], (b) wind energy coefficient contours. Flow direction is aligned with x-axis. The plots cover an area of 12km×14km

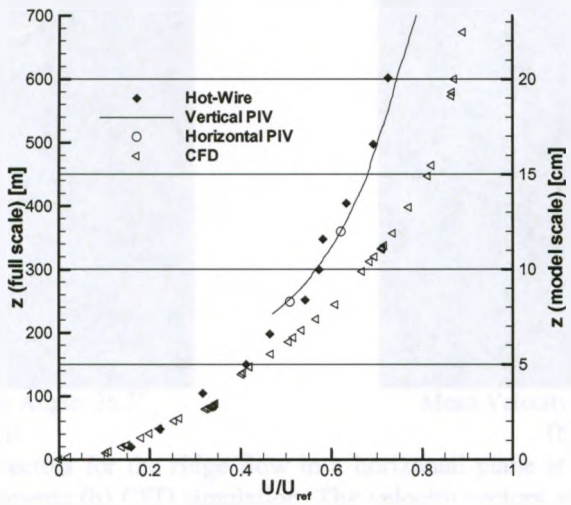


Figure 3.24: Comparison of CFD predicted mean velocity profiles by PIV and hot-wire measurements for the hill flow.

The predicted and measured velocity profiles are compared in Figure 3.24. The predicted velocity profile matches the measured one up to the height of 200m but diverges from them in the inner layer of the boundary layer (the same was observed in the valley flow).

### *3.4.5 Ridge Flow*

In section 2.2.2.3 the ridge flow was discussed and it was concluded that there is a complex, non-stationary recirculation zone in the wake of the ridge. Figure 3.25 and Figure 3.26 compare predicted and measured mean velocity vectors in horizontal planes at z=200m and z=255, respectively. The mean velocity angles (the over all flow direction) for both plots are in good agreement. However, the measured mean vectors show a well structured flow while the CFD simulations demonstrate less uniformity in the mean flow. This might be a drawback of using steady RANS equations for such a non-stationary complex flow.

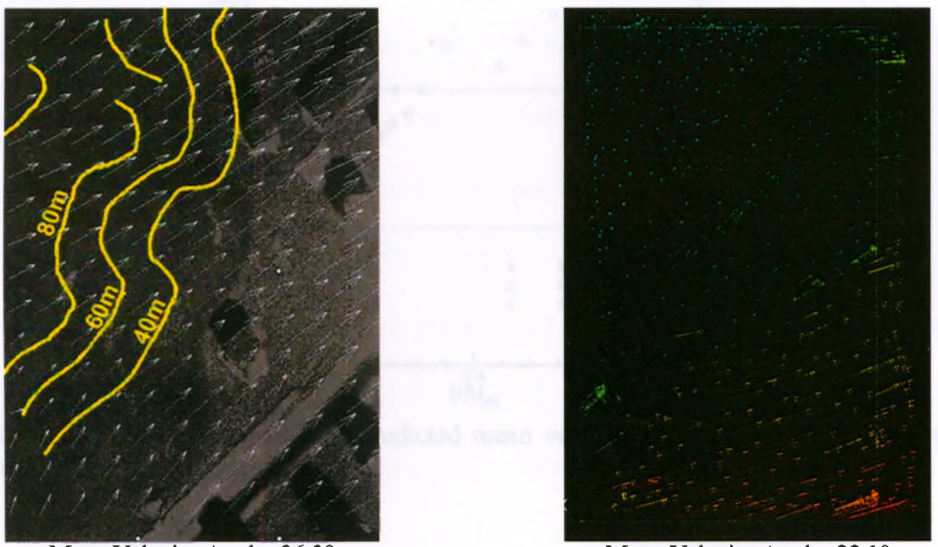


Mean Velocity Angle: 36.3° (a)

Mean Velocity Angle: 22.1° (b)

Figure 3.25: Velocity vectors for the ridge flow in a horizontal plane at $z = 200$m (6cm model scale). (a) PIV measurements (b) CFD simulation. The velocity vectors are superimposed on the topography image. Flow direction is from left to right.

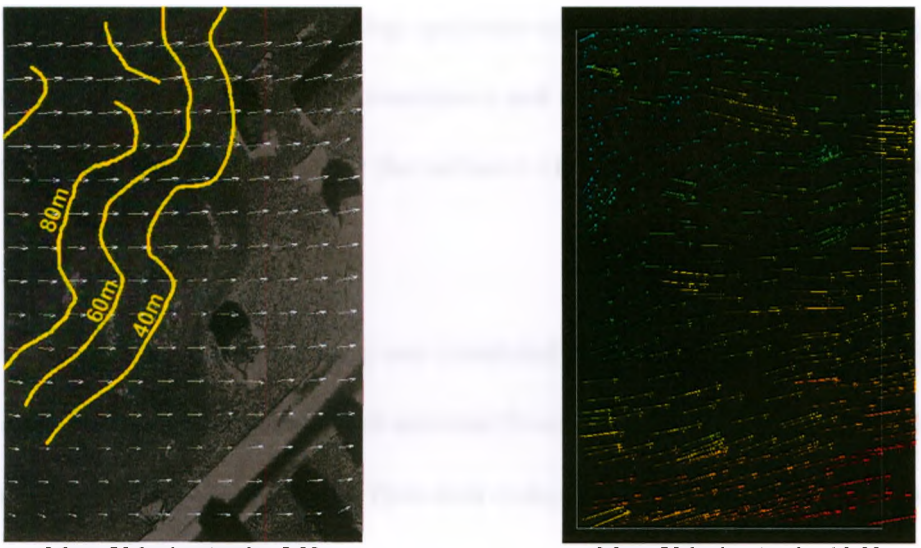


Mean Velocity Angle: 5.9° (a)

Mean Velocity Angle: 10.0° (b)

Figure 3.26: Velocity vectors for the ridge flow in a horizontal plane at $z = 225$m (7.5cm model scale). (a) PIV measurements (b) CFD simulation. The velocity vectors are superimposed on the topography image. Flow direction is from left to right.

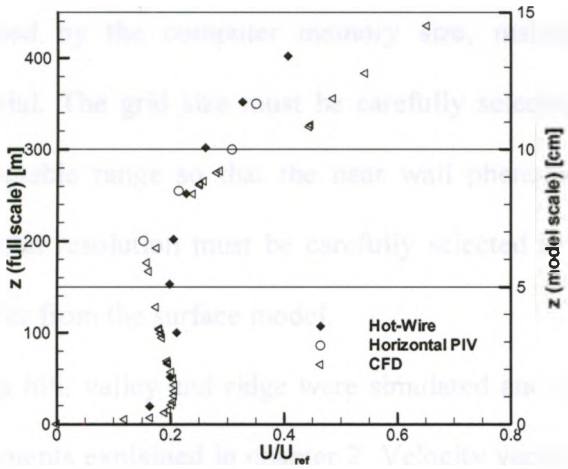


Figure 3.27: Comparison of CFD predicted mean velocity profiles by PIV and hot-wire measurements for the ridge flow.

Figure 3.27 shows the predicted and measured velocity profiles for ridge flow. Once again, CFD simulation results match the measurements up to z=300m. During the PIV experiments it was observed that the seeding in the flow is insufficient for heights above

350m. This was a result of the existing upstream topographic features in the ridge flow. The discrepancies between the CFD simulation and experiments above that height can be related to the low resolved values for the turbulent viscosity by the turbulence model.

### *3.4.6 Conclusions*

The flow over southeast Hong-Kong was simulated using CFD technique. CFD is being widely used for modeling internal and external flows. However, due to the complications involved in CFD simulation of wind flow over complex topography, CFD is at its earliest stages for this type of simulation. A universal algorithm was introduced to generate surface model of any topography for CFD simulation. Roughness elements, i.e. the foam blocks representing the built-up areas were included in the CFD model as bell-shaped roughness elements.

The limitation imposed by the computer memory size, makes the choice of grid resolution be less trivial. The grid size must be carefully selected to maintain vertical resolution in an acceptable range so that the near wall phenomena can be captured. Moreover, the horizontal resolution must be carefully selected to ensure the simulated geometry does not differ from the surface model.

Three flow cases for a hill, valley and ridge were simulated and results were compared with the PIV measurements explained in chapter 2. Velocity vectors, wind energy maps, velocity profiles and streamlines for the cases were provided. The results prove that the CFD simulations can potentially predict the wind speeds very close to the measured values up to the heights six times higher than the typical wind turbine hub height (50m) where the wind energy maps are generated at.

# 4 Conclusions

The flow over complex topographic terrain has been modeled by both wind tunnel experiments and Computational Fluid Dynamics (CFD) simulations in order to evaluate the capabilities of Particle Image Velocimetry (PIV) measurement technique and CFD modelling in providing the flow properties in detail for the purpose of wind energy estimation and structural design. Wind mapping for complex topographic terrain at high resolution is made possible using a new technique that would certainly help in wind farm development to efficiently place the wind turbines in topographic terrains.

In this study, the PIV technique was applied for wind velocity mapping on a scaled model of complex topographic terrain while the existing PIV experiments on topography are limited to smaller and more simplified topography models. The performed CFD simulations in this research which focus on flow over complex topography including a wide range of terrain roughness from water surface to urban area are far beyond the scope of existing simulations for topographic flow studies. Previous research was limited to simple topography with a narrow range of roughness distribution on their surface. In the present work, urban area roughness was successfully implemented by using specially arranged roughness element arrays in the CFD model. Moreover, the presented numerical simulations were performed by introducing an integrated GIS, CAD and CFD technique to obtain high resolution wind maps from GPS coordinates for any desired location.

An overview of the research conducted and a summary of the specific findings is presented in the following sections. Afterwards, recommendations for future work are made.

## 4.1 Experiments

PIV measurements were carried out to measure the velocity vectors in several horizontal and vertical planes over a 1:3000 scaled topographic model with high spatial resolution and maximum temporal resolution allowed by the measuring equipment, i.e. the high speed cameras. Three different model configurations were utilized to study the flow over a ridge, a valley and a hill. The results demonstrate that while the valley and hill wind flows are relatively less time dependent, the ridge flow is highly unsteady.

The mean velocity profiles obtained by PIV in vertical and horizontal planes (one data point per horizontal plane) were compared with hot-wire profiles and the overall results showed very good agreement between the two techniques.

The comparison of turbulence intensity profiles showed overall good agreement between the two techniques for flow regions with no recirculation while discrepancies were found for the ridge wake region probably originating from the limitation of both measurement techniques in resolving turbulence parameters in non-stationary flows. PIV technique can resolve spatial scales of turbulence over a relatively wide range but only a limited range of time scales are captured due to the low sampling frequency. By examining the turbulence kinetic energy (t.k.e) maps for the ridge flow, it was found that at higher heights, the flow is strongly influenced by the dominant topographic feature (i.e ridge) strongly influences while at lower heights, the flow is influenced by local topography.

Crosswind mean velocity ratios showed that for the valley and hill cases the mean flow is well correlated over large spatial extents. For the ridge the crosswind mean velocity ratios and correlations were strongly influenced by the relative position from the local and major topographies.

The proper seeding particle distribution is critical for the PIV technique to compute reliable velocity fields. The seed particles were locally injected to the flow due to the large volume of the wind tunnel. Regions of low seed density emerging in typical PIV vector maps are usually corrected using conventional operations such as local mean or median tests when extremely low seeding in relatively large portion of filed of view for some image pair is observed in only very few image pairs. However, for the case of low seeding within the field of view of the PIV camera, employing conventional techniques will result in non-physical vector maps created by mathematical smoothing and averaging algorithms. Therefore, the regions of low seeding ought to be ruled out from each image pair. Manual exclusion of these regions of non-physical vectors is a tedious job as the size and spatial location of these regions vary from image to image and data sets typically consist of 500 or more image pairs. A novel scheme introduced by Siddiqui et al. (2008) was employed to automatically detect and extract the regions with low seed density from image processing which resulted in creating vector maps with minimum possible error even though the seeding was insufficient.

## 4.2 Simulations

CFD simulations were carried out for the same test cases involved in PIV measurements performed over Hong-Kong complex topography model using commercial CFD software, FLUENT. Two benchmark test cases, NASA hump and generic hill were analyzed prior to simulation of the flow over complex topography model, in order to determine the most suitable turbulence model, domain size and configuration for simulating flow over the topographic features.

The flow over NASA hump involves regions of impingement, boundary layer, separation and reattachment which are similar to those of existing in real topography. Different turbulence models were evaluated to obtain the most suitable turbulence model for simulating the flow over the hump model as a typical topographic feature. The results such as velocity profiles, surface friction and pressure coefficients demonstrated that the steady RANS models predict a smaller separation region in comparison with the measured values while the rest of the flow pattern was well resolved. The SST k-ω model tends to slightly over-predict the velocity values in the inner region of the boundary layer. RSM model proved to be slightly more suitable for the separation region. However, the RSM model requires considerably larger memory and processing power than the k- ω model restricting the grid resolution to remain coarse when simulating detailed large domains such as complex topography. Therefore, the SST k-ω turbulence model was selected to be used throughout the rest of the simulations.

The three-dimensional hill model was used in a number of simulations to obtain the optimal domain size for flow over topography. A domain with the wall boundaries 3L upstream, 9L downstream and 9h above the model was found to be the smallest configuration among those tested that demonstrated no significant interference from the boundaries. The velocity profiles over the hill and speed-up ratios were compared with the available experimental results and were found to produce acceptable results for wind engineering purposes while predicting a smaller separation bubble. Moreover, the speed-up ratios were slightly under-predicted but they followed the same trend as measured ones when compared in along wind direction.

Steady RANS CFD simulations using the SST k-ω turbulence model for the wind tunnel model of the topography of southeast Hong-Kong were carried out and the results were compared with the wind tunnel PIV measurement results.

An algorithm to generate a CFD model for simulation the flow over topography starting from the GPS coordinates of a region was designed and used for Hong-Kong test case. The grid generation and CAD/CAM software are unable to directly build a surface model from scattered point cloud data which is usually generated by digitizing topography elevation contour maps, especially when the terrain is very complex in details and sharp edges and curves are present in geometry. The proposed algorithm was instrumental in easily creating complex terrain models with adjustable horizontal resolution.

Southeast Hong-Kong topography model included wide range of terrain roughness from water surface to highly built-up urban area comprising many high-rise structures. Conventional roughness modeling techniques in CFD simulations are designed for roughness heights existing in typical fluid dynamics test cases which are limited to a very small range, making them unable to resolve the roughness existing in wind engineering cases. A new approach was made to simulate the roughness elements (i.e. foam blocks representing the buildings) as arrays of bell-shaped roughness elements which can be easily incorporated into the CFD model. The equivalent roughness elements were found to be effectively productive for the CFD simulation of flow over terrain with high roughness heights even in extreme case of the urban area composed of high-rise structures.

The domain dimensions were setup cconsidering the minimal domain dimensions obtained in the generic hill parametric study while. The grid size was carefully selected to

maintain vertical resolution within an acceptable range while maintaining the optimal horizontal resolution to incorporate all the topography details.

Wind mapping for the near ground elevations up to 100-200m is of importance in wind engineering and wind energy applications. The velocity profiles and velocity vectors were compared with the PIV measurements and were found to be in good agreement near the ground and up to the full scale height of 300m. However, the simulated velocity profiles were over-predicted compared with the measured ones at heights higher than 300m.

The turbulence intensity profiles were examined and it was found that measured fluctuating components of the velocity are noticeably larger than the predicted ones. This problem was overcome by including the equivalent roughness element arrays to increase roughness for the near ground regions which resulted in the velocity fields up to the heights of 300m with good accuracy while the profiles for the higher heights were showed larger values due to the small turbulent viscosity resolved by the turbulence model.

## 4.3 Future work

Based on the findings of the present study, recommendations for future work are made and listed below:

- It was observed that local injection of seeding particles into the flow is a good approach for PIV measurements in large wind tunnels. A specially designed seed distributor was built to optimize the presence of particles in the measurement areas. However, the seeding quality can be improved by injecting the seed particles throughout the surface of the topography model using a porous medium.

- Different GIS, CAD/CAM and utility software were used in the procedure introduced for modeling the surface model of topography with desired resolution which can be used in the grid generation tools. Developing a new code, employing NURBS surface generation algorithms specifically optimized for creating terrain model and then integrating the code with open source or commercial GIS software can speed up the model creating process.

- Arrays of Bell-shaped roughness elements were implemented in the CFD model of topography as equivalent to the existing foam blocks representing the built-up urban area. A parametric wind tunnel study on the arrangement and dimensions of the bell-shaped elements in simulating the terrain roughness can be very helpful for CFD modelling.

## REFERENCES


Akomah A., 2004. Experimental investigation of high Reynolds number rough surface boundary layers. PhD thesis, University of Western Ontario.

Apsley D. D., Castro I. P., 1997. Flow and dispersion over hills: Comparison between Numerical Predictions and Experimental Data, J. Wind Eng. Ind. Aerodyn. 67-68, 375-386.

Arya S. P. S., Gadiyaram P. S., 1986, An experimental study of flow and dispersion in the wakes of three-dimensional low hills, Atmos. Environ. 20, 729-740.

Ayotte, K. W., Hughes D. E., 2004. Observations of boundary-layer wind-tunnel flow over isolated ridges of varying steepness and roughness. Boundary-Layer Meteorol. 112, 525-556.

Balakumar P., 2005, Computations of flow over a hump model using higher order method with turbulence modeling, AIAA 2005-1270.

Biswas D., 2006, Studies on separation control CFD validation test case based on a higher order LES model, AIAA 2006-3684.

Bitsuamlak G., Stathopoulos T. and Bedard, C., 2004, Numerical evaluation of wind flow over complex terrain: review, J. Aerospace Eng. 17, 135–145.

Blocken B., Stathopoulos T. and Carmeliet J., 2007. CFD simulation of the atmospheric boundary layer: wall function problems, Atmospheric environment. 41, 238-252.

Bowen A. J., Lindley D., 1977. A wind-tunnel investigation of the wind speed and turbulence characteristics close to the ground over various escarpment shapes. Boundary-Layer Meteorol. 12, 259-271.

Cao. S., Tamura T., 2006. Experimental study on roughness effects on turbulent boundary layer flow over a two-dimensional steep hill. J. Wind Eng. Ind. Aerodyn. 94, 1-19.

Chock G. Y. K., Cochran L., 2005. Modeling of topographic wind speed effects in Hawaii. J. of Wind Eng. Ind. Aerodyn. 93, 623-638.

Chock G. Y. K., Cochran L., 2006. Erratum to "Modeling of topographic wind speed effects in Hawaii", J. wind Eng. Ind. Aerodyn., 94, 173-187.

Chow F. K., Street R. L., 2008. Evaluation of turbulence closure models for larg-eddy simulation over complex terrain: Flow over askervein hill, American Meteorological Society, 48, 1050-1065.

Cook N. J., 1985. The designer's guide to wind loading of building structure. Part 1, Butterworths, London.

Cowen E. A. and Monismith S. G., 1997, A hybrid digital particle tracking velocimetry technique, Exp. Fluids, 22, 199-211.

Cui J., Agarwal R., 2005, CFD validation of turbulent separation control on a 2D hump (NASA langley workshop validation: Case 3), AIAA 2005-5013.

Fang C., Sill B. L., 1992. Aerodynamic roughness length: correlation with roughness elements, J. Wind Eng. Ind. Aerodyn. 41-44, 449-460.

Farquhar S., Ho T. C. E., 2004, 39 Conduit Road Mid-Levels Hong Kong, Boundary Layer Wind Tunnel Report BLWT-SS60-2004.

Ferreira, A. D., Lopes, A. M. G., Viegas, D.X. and Sousa, A.C.M., 1995, Experimental and numerical simulation of flow around two-dimensional hills, J. Wind Eng. Ind. Aerodyn. 54/55, 173-181.

Finardi S., Tinarelli G., Faggian P. and Brusasca G., 1998. Evaluation of different wind field modeling techniques for wind energy applications over complex topography, J. Wind Eng. Ind. Aerodyn. 74-76, 283-294.

Fincham A. M., Spedding G. R., 1997, Low cost, high resolution DPIV for measurement of turbulent fluid flow, Exp. Fluids, 23, 449.

Finnigan J. J., 1988. Air flow over complex terrain. Flow and Transport in The Natural Environment, Springer, Heidelberg, 183–229.

Foucaut, J. M., Carlier, J. and Stanislas, M., 2004, PIV optimization for the study of turbulent flow using spectral analysis", Meas. Sci. Technol., 15, 1046-1058.

Franck, J. A., Colonius, T., 2008, Large-Eddy simulation of separation control for compressible flow over a wall-mounted hump, AIAA 2008-0555.

Fluent 6.3.26 User's Guide. 2007. Fluent Inc , Lebanon, NH (USA).

Garvey B., Castro I., Wiggs G., Bullard J., 2005. Measurements of flows over isolated valleys. Boundary-Layer Meteorol. 117, 417-446.

Grant A. L. M., Mason P. J., 1990. Observation of boundary-layer structure over complex terrain. Q.J.R. Meteorol. Soc. 116, 159-186.

Greenblatt, D., Paschal, K. B., Yao, C. S., Harris, J., Schaeffler, N. W., Washburn, A. E., 2004, A separation control CFD validation test case, Part 1: baseline and steady suction, AIAA 2004-2220.

Greenblatt, D., Paschal, K. B., Yao, C. S., Harris, J., 2005. A separation control CFD validation test case, part 2: Zero efflux oscillatory blowing," AIAA., 0485.

Greenblatt, D., Paschal, K. B., Yao, C. S., Harris, J., Schaeffler, N. W., Washburn, A. E., 2006, Experimental investigation of separation control Part 1: baseline and steady suction, AIAA Journal, 44-12, 2820-2830.

Ho T. C. E., De Leebeeck K., 2004, Hong Kong Sanatorium and Hospital Happy Valley Hong Kong, Boundary Layer Wind Tunnel Report BLWT-SS44-2004.

Holmes J. D., Banks R.W., Paevere P., 1997. Measurements of topographic multipliers and flow separation from a steep escarpment. J. Wind Eng. Ind. Aerodyn. 69-71, 885-892.

Hunt J. C. R., Leibovich S., Richards K. J., 1988. Turbulent shear flows over low hills. Quart. J. Roy. Meteorol. Soc., 114, 1435-1470.

Ishihara T., Hibi K., Oikawa S., 1999. A wind tunnel study of turbulent flow over a three-dimensional steep hill. J. Wind Eng. Ind. Aerodyn. 83, 95-107.

Ishihara T., Hibi K., 2002. Numerical study of turbulent wake flow behind a three-dimensional steep hill. Wind and Structures. 5, 317-328.

Jackson P. S., Hunt J. C. R., 1975. Turbulent wind flow over a low hill. Quart. J. Roy. Meteorol. Soc. 101, 929-955.

Kawall J.G., Shokr M., Keffer J.F, 1983. A digital technique for the simultaneous measurement of streamwise and lateral velocities in turbulent flows. J. Fluid Mech. 133, 83-112.

Kim H. G., Lee C. M., Lim H. C., 1997. An experimental and numerical study on the flow over two-dimensional hills. J. Wind Eng. Ind. Aerodyn. 66, 17-33.

Kim H. D., Patel V. C., Lee C. H., 2000. Numerical simulation of wind flow over hilly terrain, J. wind Eng. Ind. Aerodyn., 87, 45-60.

Kim H. G., Lee C. M. and Lim H. C. 1997, An experimental and numerical study on the flow over two-dimensional hills, J. Wind Eng. Ind. Aerodyn. 66, 17-33.

Kim, J., Baik, J., and Chun. H., 2001, Two dimensional numerical modeling of flow and dispersion in the presence of hill and buildings, J. Wind Eng. Ind. Aerodyn., 89, 947.

Krishnan, V., Squires, K., Forsythe, J., 2004. Prediction of separated flow characteristics over a hump using RANS and DES, AIAA., 2004-2224.

Kondo K., Tsuchiya M., Sanada S., 2002. Evaluation of effect of micro-topography on design wind velocity. J. Wind Eng. Ind. Aerodyn. 90, 1707-1718.

Lavoie P., Avallone G., De Gregorio F., Romano G. P., Antonia R.A., 2007, Spatial resolution of PIV for the measurement of turbulence, Exp. Fluids, 43, 39-51.

Lawson N. J., Eyles J. M. and Knowles K., 2002, Particle image velocimetry and laser Doppler anemometry experimental studies of a compressible short take-off and vertical landing ground vortex flow, J. Aerospace Eng., 216, 171-187.

Lemelin D. R., Surrey D., Davenport A. G., 1988. Simple approximations for wind speed-up over hills, , J. Wind Eng. Ind. Aerodyn. 28, 117-127.

Lopes A. S., Palma J. M. L. M., Castro F. A., 2007. Simulation of the askervein flow. Part 2: Large-eddy simulations. Boundary-Layer Meteorol. 125, 85-108.

Lubitz W. D., White B. R., 2007. Wind –tunnel and field investigation of effect of local wind direction on speed-up over hills, J. Wind Eng. Ind. Aerodyn. 95, 639-661.

Lun, Y., Mochida, A., Murakami, S., Yoshino, H., Shirasawa, T., 2003, Numerical simulation of flow over topographic features by revised k-e models, J. Wind Eng. Ind. Aerodyn., 91, 231.

Lun, Y., Mochida, A., Murakami, S., Yoshino, H., 2007. Applicability of linear type revised k-e models to flow over topolographic features, J. wind Eng. Ind. Aerodyn., 95, 371-384.

Madugundi, D., Nagib, H. and Kiedaisch, J., 2008, Evaluation of turbulence models through prediction of separated flows with and without flow control and circulation effects, AIAA 2008-0567.

Mason P. J., 1986. Flow over the summit of an isolated hill. Boundary-Layer Meteorol. 37, 385-405.

Maurizi A. 2000. Numerical simulation of turbulent flows over 2-D valleys using three versions of the k-e closure model, J. wind Eng. Ind. Aerodyn., 85, 59-73.

McKenzie R. L. and Reinath R. L., 2005, Three-dimensional planner Doppler velocity measurements in a full-scale rotor wake, AIAA Journal, 43, 489-499.

Miller C. A., 1996. Turbulent boundary layers above complex terrain. Ph.D. thesis, Boundary layer wind tunnel laboratory, University of western Ontario, Canada.

Miller C. A., Davenport A. G., 1998. Guidelines for calculation of wind speed-ups in complex terrain, J. wind Eng. Ind. Aerodyn.,74-74, 189-197.

Mosedale A. D., Elliot G. S., Carter C. D., Beutner T.J., 2000, planner Doppler velocimetry in a large-scale facility, AIAA Journal, 38, 1010-1024.

Mochida A., Murakami S., Ojima T. and Kim S. 1997. CFD analysis of mesoscale climate in the greater Tokyo area, J. Wind Eng. Ind. Aerodyn. 67-68, 459-477.

Morgan, P. E., Rizzetta, D. P. and Visbal, M. R., 2005. Large-Eddy Simulation of Flow Over a Wall-Mounted Hump. AIAA. January, 0484.

Morgan, P., Rizzetta, D. and Visbal, M., 2007. Large-eddy simulation of separation control for flow over a wall-mounted hump, AIAA Journal. 45-11, November, 2643-2660.

Naess A., Clausen P. H., Sandvik R., 2000. Gust factors for locations downstream of steep mountain ridges. J. Wind Eng. Ind. Aerodyn. 87, 131-146.

Naughton, J., Viken, S. and Greenblatt, D., 2004. Wall shear stress measurements on the NASA hump model for CFD validation, AIAA 2004-2607.

Naughton, J., Viken, S. and Greenblatt, D., 2006. Skin-friction measurements on the NASA hump model, AIAA Journal, 44-6, 1255-1265.

Ngo T. T., Letchford C. W., 2009. Experimental study of topographic effects on gust wind speed, J. Wind Eng. Aerodyn., 97, 426-438.

Pearse J. R., 1982, Wind flow over conical hills in a simulated atmospheric boundary layer, J. Wind Eng. Ind. Aerodyn. 10, 303-313.

Prasad A. K., Adrian R. J., Landreth C. C., Offutt P. W., 1992, Effect of resolution on the speed and accuracy of particle image velocimetry interrogation, Exp. Fluids, 13, 105-116.

Prospathopoulos J., Voutsinas S. J., 2006. Implementation issues in 3D wind flow predictions over complex terrain. Journal of Solar Energy Engineering. 128, 539-553.

Rodrigo J. S., Van Beeck J., Dezso-Weidinger G., 2007. Wind tunnel simulation of the wind conditions inside bidimensional forest clear-cuts. Application to wind turbine siting. J. Wind Eng. Ind. Aerodyn. 95, 609-634.

Rognvaldsson O., Olafsson H., 2005. Numerical simulation of the climatology of winds in the complex terrain of Iceland. Hrvarski Meteoroloski Casopis. 40, 691-694.

Rumsey C., 2006. Reynolds-averaged navier-stokes analysis of zero efflux flow control over a hump model, AIAA, 2006-1114.

Rumsey C., 2007. Reynolds-averaged navier-stokes analysis of zero efflux flow control over a hump model, Journal of Aircraft, 44-2, 444-452.

Saric S., Jakirlic S., Tropea C., 2005. Computational analysis of locally forced flow over a wall-mounted hump at high-Re number, Proc. of 4th Int. Symposium on Turbulence and Shear Flow Phenomena, Williamsburg, 27-29, 3, 1189-1194.

Saric S., Jakirlic S., Djugum A., Tropea C., 2006. Computational analysis of a locally forced flow over a wall-mounted hump at high-re number, Int. Journal of Heat and Fluid Flow, 27-4, 707-720.

Seifert A., Pack L. G., 2002. Active flow separation control on wall-mounted hump at high Reynolds numbers, AIAA Journal, 40-7, 1363-1372.

Siddiqui M. H. K., Loewen M. R., Richardson C., Asher W.E. and Jessup A.T. 2001. Simultaneous particle image velocimetry and infrared imagery of microscale breaking waves, Phys. Fluids. 13, 1891-1903.

Siddiqui K., 2002, Laboratory measurement of the flow beneath micro scale breaking waves, PhD thesis, Department of Mechanical and Industrial Engineering, University of Toronto.

Siddiqui K. Hangan H., Rasouli A. 2008. PIV technique implementation for wind mapping in complex topographies. Meas. Sci Technol. 19-6, 065403(11pp).

Simpson R. L., Long C. H., 2002. Study of vortical separation from an axisymmetric hill, International Journal of Heat and Fluid Flow, 23, 582-591.

Stangroom P, 2004. CFD modelling of wind flow over terrain. PhD thesis, University of Nottingham.

Takahashi T., Kato S., Murakami S., Ooka R., Yassin M. F., Kono R., 2006. Wind tunnel tests of atmospheric stability on turbulent flow over a three-dimensional hill. J. Wind Eng. Ind. Aerodyn. 93, 155-169.

Takahashi T., Ohtsu T., Yassin M. F., Kato S., Murakami S., 2002. Turbulence characteristics of wind over a hill with a rough surface. J. Wind Eng. Ind. Aerodyn. 90, 1697-1706.

Taylor P. A., Teunissen H. W., 1987. The Askervein hill project: overview and background data. Boundary-Layer Meteorol. 39, 15-39.

Taylor P. A., Manson P. J., Bradley E.F., 1987. Boundary-layer flow over low hills. Boundary-Layer Meteorol. 39, 107-132.

Tong H., Walton A., Sang J. and Chan J., 2005. Numerical simulation of the urban boundary layer over the complex terrain of Hong Kong, Atmospheric Environment. 39, 2005, 3549-3563.

Troen I., Peterson E. L. 1989. European wind atlas, Published for the commission of the European communities by risoe national laboratory, 656pp.

Uchida T., Ohya Y., 2008. Verification of the prediction accuracy of annual energy output at Noma wind park by the non-stationary and non-linear wind synopsis simulator, RIAM-COMPACT, Journal of Fluid Science and Technology, 3, 3.

Uchida T., Ohya Y., 2008. Micro-Siting technique for wind turbine generators by using large-eddy simulation, J. Wind Eng. Ind. Aerodyn, 96, 2121-2138.

Uchida T., Ohya Y., 2003. Large-Eddy simulation of turbulent flow over complex terrain, J. Wind Eng. Ind. Aerodyn., 91, 219-229.

Uchida T., Ohya Y., 1999. Numerical simulation of atmospheric flow over complex terrain, J. Wind Eng. Ind. Aerodyn., 81, 283-293.

Undheim O., Anderson H.I., Berge E., 2006. Non-linear, microscale modeling of the flow over Askervein hill. Boundary-Layer Meteorol. 120, 477-495.

Wakes S., Maegli T., Dickinson K. J., Hilton M. J., 2010. Numerical modeling of wind flow over a complex topography, environmental modeling & software, 25, 237-247.

Yamaguchi, A., Ishihara, T and Fujino, Y., 2006. Numerical modeling of local wind focusing on computational domain setting and boundary treatments, The fourth international symposium on computational wind engineering.

You D., Wang M. and Moin P., 2005. Large-eddy simulation of flow over a wall-mounted hump with separation control, Annual Research Briefs, Center for Turbulence Research, Stanford University.

You D., Wang M. and Moin P., 2006. Large-eddy simulation of flow over a wall-mounted hump with separation control, AIAA Journal. 44-11, November, 2571-2577.

Yu W., Benoit R., Girarad C., Glazer A., Lemarquis D., Salmon J. R., Pinard J. P., 2006. Wind energy simulation toolkit (west): A wind mapping system for use by the wind-energy industry, Wind Engineering, 30, 15-33.

Zhu W., van Hout, R. Luznik L., Kang H. S., Katz J. and Meneveau C. 2006. A comparison of PIV measurments of canopy turbulence performed in the field and in a wind tunnel, Exp. Fluids, 41, 309-318.

# Appendix I: Error Estimate for PIV Measurements

This appendix introduces the uncertainty error related to the PIV measurements provided in chapter 2. PIV measurement errors are generated due to lack of accuracy in temporal measurements and spatial measurements. These sources of errors can be combined together and regrouped in terms of error due to the diameter of seed particles, density of particles, velocity gradients, out of plane motion of particles, dynamic range of grey-scale images, peak-locking and interpolation of velocity vectors (Cowen and Monismith (1997)). The particle size in the present PIV study was 0.5μm (or 0.005 pixels). However, the image of the particle occupies one pixel area and the exact position of the particle can not be resolved. Also, the particle size of less than one pixel causes the peak-locking error increase (the peak locking error is an inherent bias in PIV technique that appears when the correlation peak is shifted towards the nearest integer value (Finchman and Spedding (1997))). The largest error in the PIV experiments for particle diameter of one pixel is calculated and the result is scaled to the particle size of 0.005 pixels. The detailed step by step procedure can be found in Siddiqui (2002).

The velocity gradients from the raw PIV data were examined to compute the largest error. The largest mean velocity gradients in the present study were found to be $\frac{\partial v}{\partial x} = 0.0202$ and $\frac{\partial u}{\partial y} = 0.0187$ pixels/pixel for the RMS velocity components. Figure 5(e) in Cowen and Monismith (1997) was used and the error due to velocity gradients were found to be approximately $\varepsilon_v = 0.06$ and $\varepsilon_u = 0.04$ pixels.

The error associated with the particle diameter of one pixel is obtained from figure 5(a) in Cowen and Monismith (1997) which is 0.06 pixels. The particle size of one pixel was the smallest particle size provided in Cowen and Monismith (1997). Afterwards, this error is scaled to the smaller particle size of 0.005 pixels. Figure 13 in Prasad et al. (1992) provides the variation of bias (peak-locking) error and RMS error as a function of particle diameter. It was found the errors associated with a particle size of 0.007 pixels are two times larger than those of one pixel particle diameter. Prasad et al. (1992) used center of mass peak fitting scheme which is subjected to relatively high peak-locking errors. In this research, a three-point Gaussian peak fitting scheme was used. Since the three-point Gaussian scheme is less susceptible to peak-locking (Cowen and Monismith (1997)), the increase in error for this case can be approximated to be 50% (Siddiqui (2002)). Therefore, the increased gradient error due to particle size is estimated to be $\varepsilon_{v-dp} = 0.09$ and $\varepsilon_{u-dp} = 0.06$ pixels.

To estimate the error due the out-of-plane particle motion, the largest in-plane displacements (excluding the stream-wise velocity component) were examined. The largest ones were found to be in horizontal planes near the surface. Since the measurement planes were parallel to the free stream wind direction, the out-of-plane particle velocity is not expected to be larger than the maximum of *v* or *w* (instantaneous velocity components). The maximum value for instantaneous *v* (or *w*) was found to be 1.97m/s or 1.61 pixels. The laser sheet thickness was approximately 2mm (or 22 pixels) thus the out-of-plane motion error is neglected for this study.

The error due to averaging is calculated from figure 5(f) in Cowen and Monismith (1997). The figure plots AGW averaging error versus dynamic range. Dynamic range is

defined as the difference in mean maximum particle intensity level and the mean background intensity level. For 8-bit CCD cameras it ranges from 100 to 150 counts. The error related to this range is approximately $\varepsilon_{AGW} = 0.08$ pixels.

The total error for each velocity component is calculated by summing the aforementioned errors:

$\varepsilon_{vT} = \varepsilon_{v-dp} + \varepsilon_{AGW} = 0.17$ pixels; $\varepsilon_{uT} = \varepsilon_{u-dp} + \varepsilon_{AGW} = 0.14$ pixels.

Therefore, the total error for a velocity vector is $\varepsilon_T = 0.22$ pixels or $\varepsilon_T = 0.2613$ m/s. Since the maximum mean velocity in the measurement plane was 3.2m/s the error in percentage is calculated to be 8%.

# Appendix II: Turbulence Models used in CFD Simulations

The turbulence models referenced in chapter 3 are elaborated in this appendix (detailed equations and lists of constants are available in the FLUENT documentation (FLUENT 6.3.26 User's Guide (2007))). As mentioned earlier in chapter 3, employing the Reynolds averaged Navier-Stokes equations in CFD simulations is an efficient solution in terms of model size and processing time. The RANS equations only resolve the averaged flow quantities and model the turbulent structures. Equation (4.1) presents the RANS equations in tensor form:

$$\frac{\partial \rho}{\partial t}+\frac{\partial}{\partial x_i}(\rho u_i)=0$$

$$\frac{\partial}{\partial t}(\rho u_i)+\frac{\partial}{\partial x_i}(\rho u_i u_j)=-\frac{\partial p}{\partial x_i}+\frac{\partial}{\partial x_j}\left[\mu\left(\frac{\partial u_i}{\partial x_j}+\frac{\partial u_j}{\partial x_i}-\frac{2}{3}\delta_{ij}\frac{\partial u_l}{\partial x_l}\right)\right]+\frac{\partial}{\partial x_j}\left(-\rho\overline{u_i'u_j'}\right) \quad (4.1)$$

where, $u_i$ is the Reynolds averaged velocity component.

By comparing equation (4.1) with the instantaneous Navier-Stokes equations, it can be observed that an additional term ($-\rho\overline{u_i'u_j'}$) has appeared in the RANS equations which represents the effects of turbulence- These terms are called Reynolds stresses. For the closure of the RANS equations, new sets of equations must be added to the original RANS equations which are obtained from the turbulence models.

The Spalart-Allmaras, k-ε and k-ω turbulence models resolve the Reynolds stresses by assuming isotropic turbulence and relating the stresses to a single scalar quantity called turbulent viscosity ($\mu_t$). The Boussinesq hypothesis is applied in order to achieve the aforementioned relation:

$$-\rho\overline{u_i'u_j'} = \mu_t\left(\frac{\partial u_i}{\partial x_j}+\frac{\partial u_j}{\partial x_i}\right)+\frac{2}{3}\left(\rho k+\mu_t\frac{\partial u_i}{\partial x_i}\right) \tag{4.2}$$

where, $k$ is the turbulence kinetic energy.

*The Spalart-Allmaras Model*

Spalart-Allmaras model is a single equation turbulence model which solves for turbulent kinematic viscosity. The transport equation for $\mu_t$ is provided in equation (4.3):

$$\frac{\partial \mu_t}{\partial t}+\frac{\partial}{\partial x_i}(\mu_t u_i)=G_v+\frac{1}{\sigma_{\tilde{v}}}\left[\frac{\partial}{\partial x_j}\left\{(\mu+\mu_t)\frac{\partial}{\partial x_j}\left(\frac{\mu_t}{\rho}\right)\right\}+C_{b2\rho}\left(\frac{\partial}{\partial x_j}\left(\frac{\mu_t}{\rho}\right)\right)^2\right]-Y_v \tag{4.3}$$

where, $G_v$ is the production and $Y_v$ is the destruction of turbulent viscosity. $\sigma_{\tilde{v}}$ and $C_{b2\rho}$ are constants. Note that $\mu_t$ in equation (4.3) is slightly modified for the near wall regions.

*The k-ε Model*

The k-ε model solves two equations for turbulence kinetic energy and turbulence rate of dissipation that are listed in equations (4.4) and (4.5). The transport equation for turbulence kinetic energy ($k$) is:

$$\frac{\partial}{\partial t}(\rho k)+\frac{\partial}{\partial x_i}(\rho k u_i)=\frac{\partial}{\partial x_j}\left[\left(\mu+\frac{\mu_t}{\sigma_k}\right)\frac{\partial k}{\partial x_j}\right]+G_k-\rho\varepsilon \tag{4.4}$$

And the transport equation for turbulence rate of dissipation ($\varepsilon$) is:

$$\frac{\partial}{\partial t}(\rho\varepsilon)+\frac{\partial}{\partial x_i}(\rho\varepsilon u_i)=\frac{\partial}{\partial x_j}\left[\left(\mu+\frac{\mu_t}{\sigma_\varepsilon}\right)\frac{\partial \varepsilon}{\partial x_j}\right]+C_{1\varepsilon}\frac{\varepsilon}{k}G_k-C_{2\varepsilon}\rho\frac{\varepsilon^2}{k} \tag{4.5}$$

where, $G_k$ is the generation of turbulence kinetic energy due to the mean velocity gradients, $C_{1\varepsilon}$, $C_{2\varepsilon}$ and $C_{3\varepsilon}$ are constants. $\sigma_K$ and $\sigma_\varepsilon$ are the turbulent Prandtl numbers for $k$ and $\varepsilon$. It is assumed that the flow is fully turbulent and the effects of molecular viscosity are negligible. Therefore, k-ε models can not be used directly near the wall boundaries.

*The k-ω Model*

The standard and shear stress transport (SST) k-ω models both solve two equations for turbulence kinetic energy and specific dissipation rate (ω). The turbulence kinetic energy transport equation for these models is:

$$\frac{\partial}{\partial t}(\rho k)+\frac{\partial}{\partial x_i}(\rho k u_i)=\frac{\partial}{\partial x_j}\left[\Gamma_k \frac{\partial k}{\partial x_j}\right]+G_k-Y_k \tag{4.6}$$

And the transport equation for turbulence specific dissipation rate is:

$$\frac{\partial}{\partial t}(\rho \omega)+\frac{\partial}{\partial x_i}(\rho \omega u_i)=\frac{\partial}{\partial x_j}\left[\Gamma_\omega \frac{\partial \omega}{\partial x_j}\right]+G_\omega-Y_\omega+D_\omega \tag{4.7}$$

where, $\Gamma_k$ and $\Gamma_\omega$ represent the effective diffusivity of $k$ and ω. $Y_k$ and $Y_\omega$ represent the dissipation of $k$ and ω due to turbulence. $D_\omega$ represents a cross-diffusion term which is only calculated for SST k-ω model.

The standard k-ω model is recommended for low Reynolds flows, wall-bounded boundary layer and transitional flows while the SST model operates in a wider range of flows such as cases involving adverse pressure gradient on airfoils and wall bounded flows.

*The Reynolds Stress Model (RSM)*

Reynolds stress model is a five equation model which solves directly for the turbulent shear stress components; unlike the Spalart-Allmaras, k-ε and k-ω models which assume the turbulence is isotropic by employing the Boussinesq's assumption. The Reynolds transport equations are derived from averaging the momentum equation multiplied by a fluctuating property:

$$\frac{\partial}{\partial t}\left(\rho\overline{u_i'u_j'}\right)+\frac{\partial}{\partial x_k}\left(\rho u_k\overline{u_i'u_j'}\right)=\frac{\partial}{\partial x_k}\left[\mu\frac{\partial}{\partial x_k}\left(\overline{u_i'u_j'}\right)\right]-\rho\left(\overline{u_i'u_k'}\frac{\partial u_j}{\partial x_k}+\overline{u_j'u_k'}\frac{\partial u_i}{\partial x_k}\right)$$
$$-2\rho\Omega_k\left(\overline{u_j'u_m'}\varepsilon_{ikm}+\overline{u_i'u_m'}\varepsilon_{jkm}\right)-\frac{\partial}{\partial x_k}\left[\rho\overline{u_i'u_j'u_k'}+\overline{p\left(\delta_{kj}u_i'+\delta_{ik}u_j'\right)}\right] \qquad (4.8)$$
$$+\overline{p\left(\frac{\partial u_i'}{\partial x_j}+\frac{\partial u_j'}{\partial x_i}\right)}-2\mu\overline{\frac{\partial u_i'}{\partial x_k}\frac{\partial u_j'}{\partial x_k}}$$

By solving equation (4.8), all individual Reynolds stresses i.e. $-\rho\overline{u_i'u_j'}$ can be obtained. However, the last three terms in the equation (4.8) (which are turbulent diffusion, pressure strain and dissipation) must be modeled in order to close the equations set. RSM is suitable for complex three-dimensional flows with strong swirl and rotation. However, it is substantially more memory and time intensive compared to the two-equation models.